
DOPED TiO_2 BONE SCAFFOLDS

-CORROSION RESISTANCE COMBINED WITH HIGH COMPRESSIVE STRENGTH-

---

A doctoral thesis by
Anne Klemm

Department of Biomaterials
Institute of Clinical Dentistry
Faculty of Dentistry
University of Oslo
Norway

Series of dissertations submitted to the
Faculty of Dentistry, University of Oslo

ISBN 978-82-8327-048-8

Cover: Hanne Baadsgaard Utigard.
Print production: Reprosentralen, University of Oslo.

TO ELSE

ACKNOWLEDGEMENTS

This work was conducted at the Department of Biomaterials, Faculty of Dentistry, University of Oslo during the years 2016–2020. I would like to express my gratitude to the Faculty of Dentistry for the opportunity to work on this exiting PhD project.

Special thanks to Håvard! I could have never hoped for a better boss. You made it possible to tackle different challenges during my PhD life. I truly appreciate all the trust you put in me.

Thank you so much for showing me what it takes to be a good scientist, Hanna! You gave me all the needed space to follow my own path and supported me with absolutely everything when I needed it. Thanks for introducing me to the wonderful world of TiO_2 bone scaffolds and enjoying every slurry with me. I will truly miss the scaffold lab!

Along my way, I was very fortunate to work with great scientist. Thanks to all the great people from the Department of Physics and Department of Bioscience for answering all my questions. Without this support, I could not have made the FIB run. Special thanks to Patricia who spend Friday nights with me at the TEM. It was so nice to work with you Mattis, thank you for producing hundreds of foams for me. I am very grateful for the time I spent at the 3B's Research group, it was so important for me in so many ways. Particular thanks to Manu, who showed me the fun of cell experiments.

I would like to thank the entire Department of Biomaterials, I really enjoyed my PhD! Special thanks to Manu for giving me vital input, even at times when your own stress level was high. Thank you David for the abundancy of productive coffee breaks, whilst discussing the zeta potential, scaffolds and "Shore Stein Papier" – they were an improvement of any given day. Thank you for teaching me, how to appreciate the small things in life, Aman. I couldn't have asked for a better friend to share my PhD life with. I had the best lunch breaks with Pawel, thanks for the hours of laughter. I could always have a chat and a Tøyencola with Monique and Stig, thank you so much for giving me a home in Oslo. Gretchen, put your make-up on and let's have a beer at our pub, thank you for the best start of my PhD time in Oslo.

Thank you for encouraging the choice to go to Oslo, Papa. Thanks for your love Mama, without you as a role model, I would have never managed the PhD in such an organized way. Henry, thanks for being the best herding dog and taking care of all three of us. Katrin, you have been and will always be one of the most important anchors in my life. Thank you Mirco for being at my side at any time. Having the same destination, but choosing completely different ways widens my scope a lot and enriches my life…and made it perfect with Else.

Anne Klemm Oslo, April 2020

TABLE OF CONTENTS

LIST OF PUBLICATIONS

Paper I	Klemm, A. and Tiainen, H., *Coagulated concentrated anatase slurry leads to improved strength of ceramic TiO_2 bone scaffolds.* Ceramics International, 2018. **44**(6): p. 6265-6271.
Paper II	Klemm, A., Gomez-Florit, M., Carvalho, P., Wachendörfer, M., Gomes, M., Haugen, H., Tiainen, H., *Grain boundary corrosion in TiO_2 bone scaffolds doped with group II cations.* Journal of the European Ceramic Society, 2019. **39**(4): p. 1577-1585.
Paper III	Klemm, A. and Tiainen, H., *Highly porous Sr-doped TiO_2 ceramics maintain compressive strength after grain boundary corrosion.* Manuscript, 2020.

Appended publications are reprinted with the kind permission of the copyright holders.

1 INTRODUCTION

Nowadays, placing a dental implant is a standard procedure to replace missing teeth. Years of clinical experience regarding design and techniques has led to a success rate of more than 90% for dental implants.[1-3] To meet the requirement of success, the patient needs to be satisfied with the implant function in addition to the absence of pain, bleeding or peri-implant bone loss.[4] One important factor for the success of an implant is sufficient bone density and volume to guarantee stability between the implant and the bone.[5,6] A loss in alveolar bone can cause problems regarding a sufficient bone volume. The loss of a tooth, a tumor or inflammatory diseases, such as periodontitis, can cause bone resorption, resulting in an insufficient bone volume for placing a dental implant. Thus, the treatment of missing bone volume to improve dental implant stability is a current challenge in dentistry. To face this challenge, bone grafts have successfully been used.[7-10] Bone grafts are used as structures to guide bone during regeneration to achieve sufficient bone volume.

The gold standard treatment for bone grafting is the use of autologous bone grafts, where endogenous bone from the same patient is used as a bone substitute.[11,12] Other options are allografts, which are grafts derived from another donor of the same species, or xenografts, that are extracted from a donor of another species.[13,14] The main disadvantages of all these types of biological grafts are their limited availability, risk of infections and the rejection of the graft by the host tissue.[15-20] Because of these limitations, there is a special interest in bone grafts made of synthetic materials. Advantages of synthetic grafts are on the one hand the option of storage, which guarantees unlimited availability. On the other hand, the fabrication of synthetic grafts ensures the product equality and can be designed according to clinical needs.[21] There are two main challenges for synthetic bone grafts to meet the requirements of successful bone regeneration. While some properties are dependent on the graft material, some important properties can also be influenced during the fabrication process. Consequently, the success of synthetic bone grafts depends on their capacity to allow the formation of new bone tissue, or osteogenesis, and to provide sufficient mechanical support at the defect site for the new bone formation to occur until enough bone tissue has been formed to allow normal function.[22,23] While some synthetic grafts show inadequate mechanical strength compared to natural bone, others show insufficient porosity and interconnectivity of pores to ensure bone ingrowth and vascularization. Thus, there is a great need for synthetic bone graft materials that have similar properties to natural bone tissue.

1.1 BONE GRAFTS

1.1.1 REGENERATIVE CAPACITY OF BONE

Bone tissue forms a strong supportive structure for soft tissues and muscles. It is a highly dynamic tissue which regenerates itself over the whole lifetime of an individual. Bone tissue consist of 30-35% organic and 65-70% inorganic substances. The organic phase mostly consist of collagen type I, while the inorganic phase is mainly composed of calcium and phosphate in the form of hydroxyapatite, tricalcium phosphate, calcium carbonate and calcium fluoride.[24] Two different types of bone are present, namely cortical (compact) and trabecular (cancellous) bone. Cortical bone is dense and constitutes approximately 80% of the skeletal mass. It exhibits a low porosity of 5-20% and a low surface area. Cortical bone forms the outer part of bones and envelopes the inner cavity, where the trabecular bone is filled with bone marrow.[24-26]

Bone tissue is able to regenerate itself without scar formation by resorption of injured bone tissue and formation of new bone tissue.[27] Furthermore, resorption and formation of bone tissue enables bone to adapt to its physical environment.[25] Bone is a composite structure that includes cells, extracellular matrix (ECM) and lipids. The main bone cells related to bone regeneration are osteoblasts, which are responsible for bone formation, osteoclasts, which are responsible for bone degradation, and osteocytes, which sense mechanical strains within the ECM.[28] Following injury, three main phases of bone regeneration are present, as shown in Figure 1-1.

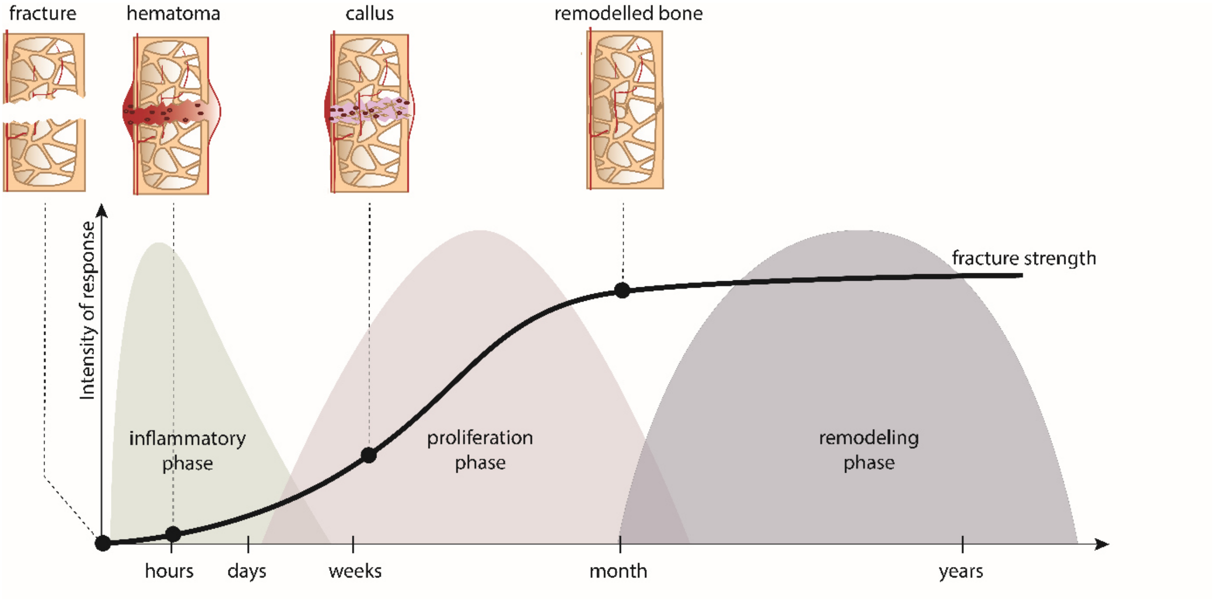

Figure 1-1: Immune response depending on bone regeneration phase. Inflammatory signals are dominant during the inflammatory phase, where a hematoma is forming. To stabilize the fracture site, a callus is formed, which is remodelled to bone during the proliferation and remodeling phases. Adapted from Burn.[29]

During the early inflammatory stage, a hematoma is formed immediately and blood is present in between and around the fracture edges.[30] The immune system is activated, inflammation occurs and a primitive callus starts to form to reduce uncontrolled mobility of the fracture site.[24,27]. To form a callus consisting of a fibrin network and aggregated platelets, a complex cascade of simultaneous signals starts.[31] Macrophages release different inflammatory cytokines which activate osteoclasts. Osteoclasts then attach to the surface of the injured bone and start to resorb the bone tissue by secreting hydrochloric acid, which dissolves hydroxyapatite, the major inorganic component of bone.[26,32] The cytokines recruit mesenchymal cells (MSC), which later on differentiate to osteoblasts. Simultaneously, platelets present in blood are activated and release different growth factors, mainly platelet-derived growth factor (PDGF) and transforming growth factor beta (TGF-β), which cause the migration, activation and proliferation of mesenchymal cells, and the formation of new blood vessels.[33] During the second phase, the callus is replaced with woven bone and gets more solid and mechanically rigid.[34] Specific proteins, such as bone morphogenetic proteins (BMP), are released from the bone matrix and undifferentiated MSCs start differentiating into osteoblasts.[35] These osteoblasts express high level of vascular endothelial growth factor (VEGF) to promote further invasion of blood vessels.[36] During the last phase, the remodeling phase, the replacement of woven bone to mature lamellar bone takes place. Osteoblasts lay down uncalcified bone matrix and differentiate to osteocytes, which interconnect in the ECM.[26] Osteocytes make up 90-95% of cells in bone tissue and release signals to coordinate the actions of osteoblast and osteoclast for optimal bone regeneration.[32] As shown in Figure 1-1, the inflammatory phase takes up to 7 days, while the proliferative stage lasts for weeks and the remodeling phase can lasts for years.[24,27,29] The complex cascade of signals during bone regeneration is characterized by different intensities of response and presence of different cytokines and growth factors. The typical responses during the phases can overlap each other, because of simultaneous resorption and remodeling process.

1.1.2 CLINICAL APPLICATION OF BONE GRAFTS

The self-regeneration potential of bone can be used in clinical applications. In guided bone regeneration (GBR), an alveolar bone defect is covered and stabilized with a membrane.[10,37,38] The main principle of this technique is to create space between the bone defect and the gingival soft tissue to promote bone regeneration within this region.[39,40] The main function of the GBR membrane is to facilitate primary wound closure and to prevent the invasion of epithelial cells into the defect. Thus, the defect is kept free from soft tissue and enough space is maintained for bone ingrowth and angiogenesis.[39,41,42] Protected by the membrane, bone cells start to regenerate the tissue as described earlier. The initial inflammatory response results in migration of inflammatory cells, cytokines and growth factors initiating the bone healing cascade.[22]

The potential of self-regeneration is limited to small, non-critical size bone defects. The loss of a tooth, tumor resection or an inflammatory disease such as periodontitis can cause a dramatic loss of alveolar bone.[43,44] In case of a critical size bone defect, the self-regeneration potential can be used with the aid of support structures known as bone grafts. In GBR, a bone graft is additionally covered by the membrane.[45] Osteoclasts and osteoblasts are present on the graft surface [46]. Bone cells are growing insider the graft and bone tissue starts to regenerate.[22] The clinical goal of bone grafts is primary bone healing and volume preservation. By minimizing micro-motion between the graft and host bone, the formation of a callus is suppressed and strong lamellae bone is formed within the bone graft.[31]

1.1.3 THE IMPORTANCE OF SYNTHETIC BONE GRAFTS

The gold standard bone graft in critical size defects is an autologous bone graft.[12,47] Autografts are taken from another bone in the same individual.[48] Advantages of these bone grafts are the presence of osteogenic cells as well as growth factors.[48,49] Additionally, a low immune reaction is expected using material from the same individual. Nevertheless, autologous bone grafts show a complication rate of 30% with the main complications being morbidity, pain, prolonged hospitalization, the increased risk of deep infections caused by the second surgery and the large volume of bone typically needed to graft critical size defects.[31,48,50] In combination with the limited availability of autografts, these complications have led to the use of allografts and xenografts as possible alternatives for autografts. Allografts are grafts transferred between two different individuals of the same species, while xenografts are transferred between different species.[20] These alternatives show osteoconductive potential and they can be stored, which improves their availability.[51,52] Disadvantages of using allo- and xenografts are the increased risk of infections and the potential rejection of the graft by the host tissue.[13,53,54] Thus, sterility is a major concern for allo- and xenografts. Compared to autografts, both allo- and xenografts require a more sterile processing, which has been shown to result in reduced osteoinductive properties and less revascularization.[14]

To minimize complications related to biological bone grafts, there has been an increasing interest in developing synthetic bone scaffolds.[47,50,55] Advantages of synthetic bone grafts are the option for long-term storage, and thus, unlimited off-the-shelf availability, simplified sterilization process and reduced morbidity.[56] A present challenge for designing synthetic bone grafts is to reach the properties required from bone grafts, which are partly naturally present in biological grafts because of their similarity to natural bone. Synthetic grafts can only exhibit osteoconductive and osteointegrative potential.[56] Osteoconduction, or the ability to support bone growth, is dependent on the geometrical properties of the bone graft material. Thus, similar properties to natural bone are required in terms of mechanical strength, porosity, pore size and the interconnectivity of the pores.[22,57-60] Osteointegration, the ability that bone bonds chemically to the surface, is mostly dependent on the material surface. Because of their similar chemical composition to the inorganic phase of the bone matrix, calcium phosphate bioceramics are often used as synthetic bone graft materials.[56,61,62] Due to Ca^{2+} and PO_4^{3-} ions, a strong chemical bond between bone an the implant is possible.[56,61,63-65] However, there are also limitations involved the use of these biocermics as bone graft materials. For example, beta tricalcium phosphate (β-TCP) shows a high degradation rate not equal to bone formation, which results in less regenerated bone volume than available volume as a consequence of the fast resorption of β-TCP.[66] To reduce the degradation rate, the combination of β-TCP and hydroxyapatite (HA) are often used. Further improvement that is achieved by combining β-TCP and HA is an increased in compressive strength. However, the strength of this biphasic calcium phosphate material is still not comparable to that of bone.[67,68] Thus, the biggest disadvantage of calcium phosphate ceramics as bone graft substitutes is their low mechanical strength and brittleness compared to bone.[28,50] Consequently, there is a need for alternatives to calcium phosphates that have higher compressive strength. These alternatives could be oxide ceramics, such as aluminum oxide (Al_2O_3), zirconium dioxide (ZrO_2) and titanium dioxide (TiO_2). Although Al_2O_3 and ZrO_2 have higher compressive strength than TiO_2, no exchange of ions between implant and bone are possible, resulting in insufficient osteointegration.[56,69,70] In contrast, TiO_2 exhibits a negatively charged material surface when exposed to the human body fluids and allows Ca^{2+} attraction.[71,72] Further phosphate attraction enables the formation of a hydroxyapatite layer, which creates a strong bond to bone.[73-75] Furthermore, TiO_2 is a highly biocompatible material that does not show any undesirable biological effects, such as toxic, allergenic or immunogenic reactions, when implanted into the human body.[76,77] These properties make TiO_2 a very promising material for bone graft substitutes.

1.2 PROCESSING OF CERAMIC BONE GRAFTS

Several graft properties have direct influence on osteoconduction and thus, the success of a bone scaffold. Porosity and interconnected pore network are important properties for cell ingrowth and vascularization.[57,59,78] Thus, a bone scaffold needs to be highly porous. To produce porous ceramic scaffolds, the most common methods are direct foaming, sacrificial template and replica method, as shown in Figure 1-2.[79] In direct foaming method, air bubbles are incorporated to a ceramic suspension to get the final porous structure. To control the porosity, the air bubbles need to be stabilized by surfactants or particles. Otherwise, destabilized air bubbles result in increased bubbles and larger pores. In sacrificial template foaming, a dispersed sacrificial phase within the ceramic suspension is removed to get the final shape. Thus, the final shape is a negative of the sacrificial phase. Although this method is very easy, it is not recommended for bone scaffold fabrication because high porosities cannot be achieved using this method. The replica method, on the other hand, uses a coated template which determines the final shape of the produced ceramic foams after removing the template.[80] To ensure optimal replication of the foam template, the used ceramic suspension should have a shear-thinning behavior to guarantee sufficient removal of excess slurry, which prevents blocked pores.[80,81]

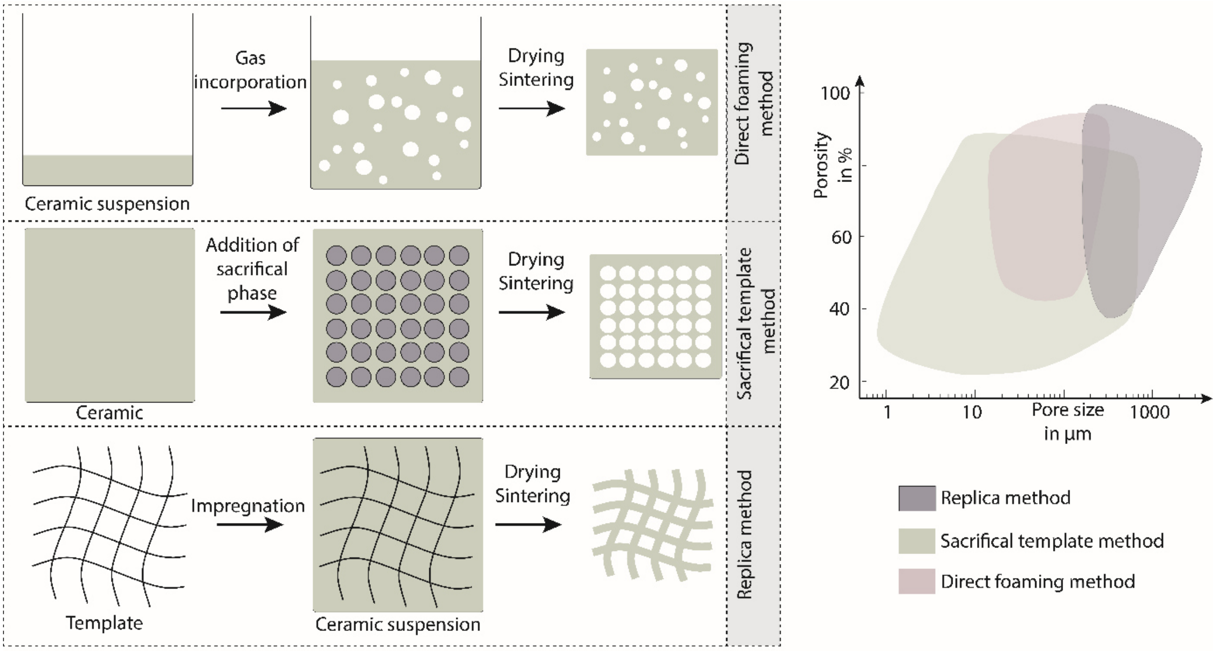

Figure 1-2: Processing of macroporous ceramics (Adapted from Studart et al.[80]). Scaffolds produced with sacrificial template method show the lowest porosity with smallest pore size. An optimal pore size of 300-400 µm and high porosity can be reached by scaffold production via replica method.

As shown in Figure 1-2, scaffolds produced with different methods differ in their pore size and porosity. While pore size and porosity are the lowest in scaffolds produced with the sacrificial template method, both values are increased by using the replica method. Furthermore, the interconnectivity of pores is the highest using the replica method. The optimal pore size for bone scaffolds is typically reported between 300 - 400 µm.[82,83] Thus, replica method is of particular interest when producing bone scaffolds. However, the production of successful ceramic bone scaffolds using this method begins with a suspension and includes sintering. To improve and control the scaffold properties, the suspension properties and material densification kinetics during sintering need to be well studied.

1.2.1 CERAMIC SUSPENSIONS

When using the polymer sponge replication method, slurry behavior is one of the most important factors that directly influence the scaffold properties. Ceramic suspensions contain particles dissolved in a liquid phase. Forces present between these particles determine the slurry behavior. Attractive van der Waals forces result from interactions of dipoles, while the repulsive forces result from charged particle surfaces.[84,85] Derjaguin, Landau, Verwey and Overbeek first described the sum of these attractive and repulsive forces as a net-force depending on the distance between particles, which is known as the DLVO theory (Figure 1-3).[86-88]

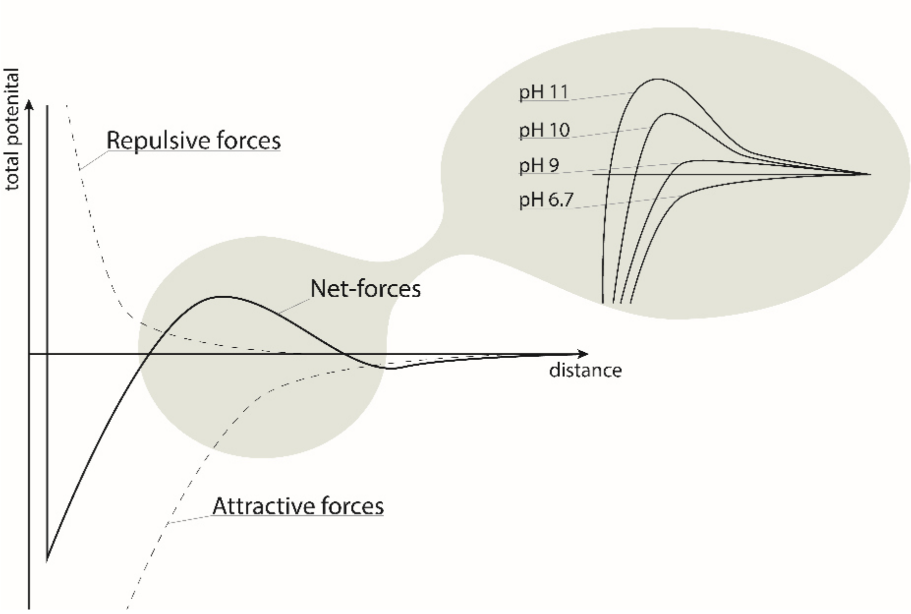

Figure 1-3: Net force in suspension according to DLVO theory. The increased energy barrier depending on pH is also highlighted in the figure (adapted from Israelachvili. [89])

This net-force can be used to determine the stability of ceramic suspensions. A stable suspension does not exhibit any agglomeration of particles.[90] Agglomeration occurs when the attractive van der Waals forces are dominant. Van der Waals (vdW) forces are long-range forces that are always attractive. Furthermore, the vdW forces are insensitive to variations in electrolyte concentration and pH.[89,90] Therefore, to avoid agglomeration and to get a stable suspension, repulsive forces need to be more dominant than the vdW forces. The repulsive forces in colloidal systems are caused by the formation of an electric double layer (EDL) around dispersed particles.[91] This double layer forms because of charging mechanisms. Possible charging mechanism are, on the one hand, ionization or dissociation of surface groups, and on the other hand, adsorption or binding of ions. As opposed to the vdW forces, the repulsive forces are strongly dependent on pH and the electrolytes.[92] This dependency has influence on the first maximum of the net-force, as highlighted in Figure 1-3.[93] Considering a constant particle distance, a decrease in pH would lead to a decrease in repulsive forces and a decreased net-force, while vdW forces remain constant. Thus, the energy barrier for particle agglomeration is decreased for this specific particle distance.[85,89,94]

1.2.2 ZETA POTENTIAL

The electric double layer which causes repulsive forces around a particle is shown in Figure 1-4. The first layer, the so-called Stern layer, consists of ions adsorbed onto the particle surface due to chemical interactions. The second layer is a diffusive layer between the Stern layer and the slipping plane. The slipping plane describes the plane beyond which ions in the solution are unaffected by the motion of the dispersed particles, the exact distance of which from the surface is unknown.[95]

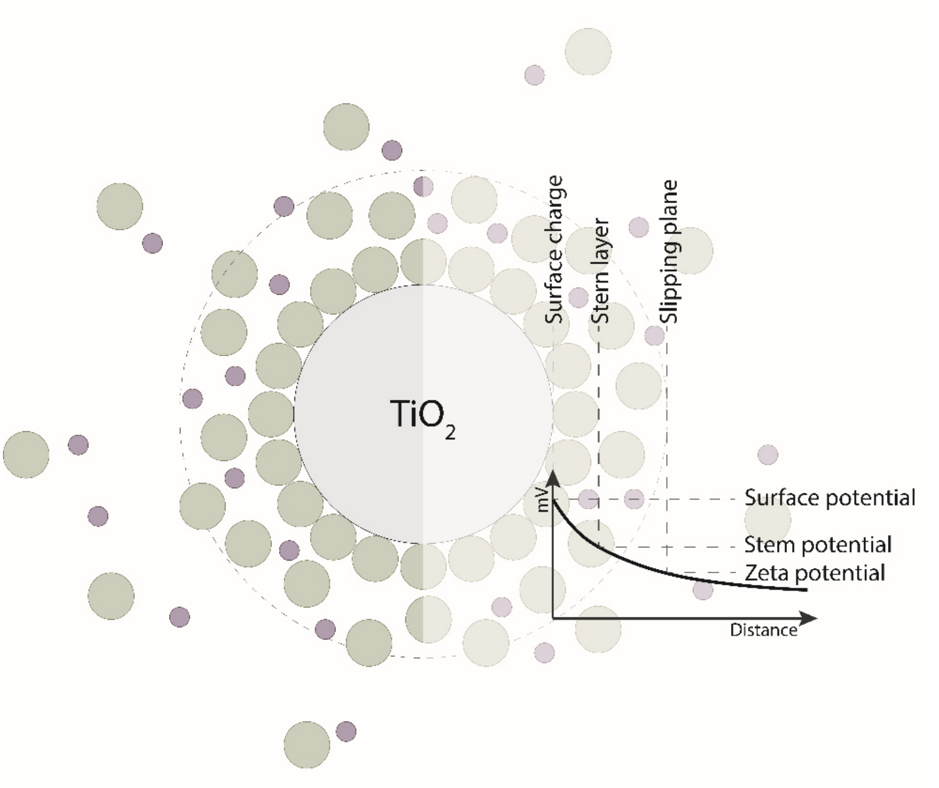

Figure 1-4 – Electric double layer forming on the surface of particles surfaces dispersed in water. The potential of the layer depends on the distance from the particle surface. ζ potential is defined as the potential between the slipping plane and the bulk solution.

As also shown in Figure 1-4, the zeta potential (ζ potential) is defined as the potential between the slipping plane and the bulk solution.[95,96] Although the distance between the slipping plane and the particle surface is not defined, the ζ potential is a key factor in colloidal systems. Due to this potential, an assumption of the repulsive forces in a suspension can be made. The ζ potential depends strongly on the pH and the ionic strength of the solution in which the particles are suspended.[97] The influence of ions can cause compression of the EDL, which in turn causes a decrease in the ζ potential, and according to the DLVO-theory, a decrease in the repulsive force. Furthermore, specific ion adsorption on the particles can cause a shift of the isoelectric point (IEP), which describes the pH where the ζ potential is zero, to higher or lower pH values.[98] These ions can interact differently with particle surfaces, and based on their dominant interaction in the ceramic suspension, they can be described as inert or non-inert electrolytes.[99] While inert and non-inert electrolytes cause a EDL compression, only non-inert electrolytes cause an IEP shift due to a specific ion bonding to the particle surface.[98] The bonding, and furthermore, the inert or non-inert behavior of electrolytes is dependent on the material and electrolyte concentration.[100,101]

1.2.3 SUSPENSION PROPERTIES

By controlling the stability of the ceramic suspension, the quality, processability and properties of many products and devices can be directly influenced. Since the vdW forces are insensitive to the electrolyte, the influence of repulsive forces in a suspension become the crucial factor for the stability of ceramic suspensions. One important parameter influenced by the presence of additional ions is the suspension viscosity. Previous studies have shown that the presence of additional ions leads to a decrease in ζ potential.[102-104] The decreased ζ potential for low pH values was observed for all tested ions. Furthermore, these studies also showed the pH_{IEP} shift caused by non-inert electrolytes. Moreover, a decreased ζ potential can lead to an increase in viscosity.[102] The increased suspension viscosity was caused by the dominant influence of attractive vdW forces as the additional ions present in the suspension decrease the repulsive force. As stated by the general DLVO theory, this causes high attractive forces between particles and results in a high suspension viscosity. Especially for the replica method, the suspension viscosity plays a key role and can directly influence the final scaffold properties. For example, an increase in viscosity can lead to a better foam impregnation, resulting in an increased compressive strength.[81]

Nonetheless, the DLVO theory has its limits to explain suspension stability and fails to explain the stability of highly concentrated suspension with an interparticle distance smaller than 5 nm.

One reason for this is the existence of short-range non-DLVO forces, which can occur between surfaces in water and aqueous salt solution.[89,91] Although the properties of these forces are still not fully understood, they can be divided into strongly monotonically repulsive forces, attractive forces, oscillatory forces, or a combination of these. Monotonically repulsive forces are known as hydration forces and were first proposed by Langmuir in 1938.[89] At higher salt concentrations, hydrated ions bind to the surface and give rise to a repulsive hydration force. The higher the hydration number of an ion the higher is the strength and range of the hydration force. These forces are important phenomena especially in controlling technological processes such as ceramic processing and in preventing agglomeration of ceramic particles in highly concentrated suspensions to yield high packing densities.[89,105]

1.2.4 SINTERING OF CERAMICS

In the replica method, polymer foams are coated with a ceramic suspension.[106] Sintering takes place at high temperatures below the melting temperature of the material (solid-state sintering).[85] The driving force in this process is the reduction of free surface energy. Thus, particles coalesce, the internal surface area of pores is eliminated and results in the densification of the material. This densification process can be divided into three stages.[107] At high temperatures, sharp necks start to form between individual crystalline particles and the crystals, or grains, begin to grow as the low self-diffusion coefficient of the material is increased by the increased temperature and the material densifies. The removal of the last few percentage of porosity is difficult and isolated, closed pores can be present after sintering. As shown in Figure 1-5, the relative density increases with sintering time.

In some cases, a liquid phase can be present during sintering. In the presence of a liquid phase, densification is enhanced through better rearrangement of particular solids and faster matter transport through liquid than solid. These influences are dependent on the liquid volume, which in turn can be controlled by additives. Disadvantage of a liquid phase during sintering is a remaining glassy intergranular phase which may alter the mechanical properties of the sintered material.[85]

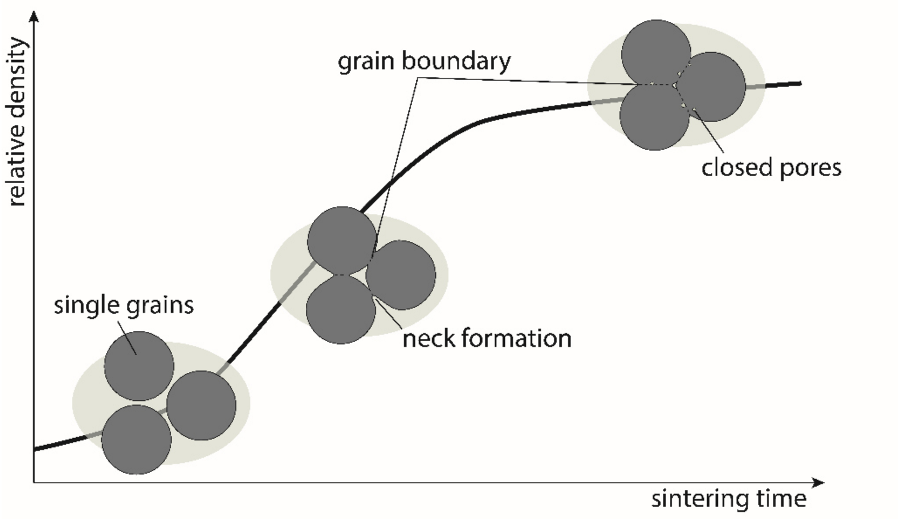

Figure 1-5: Relative density of ceramic particles as a function of sintering time. While the material densifies, surface area is reduced, grain boundaries and closed pores between the grains are formed. Adapted from Tanaka et al.[108] and Kwon et al.[109]

During solid or liquid-phase sintering, the mechanism of grain growth is of special interest. Grain growth describes the increase in grain size of a single-phase solid. As mentioned before, the driving force for grain growth is the reduction of free surface energy. Atoms in grain boundaries have higher energy than atoms in the bulk material. Thus, increasing grain size reduces the total grain boundary area, which is the driving force for sintering.[85] Different mechanism are present during grain growth. As shown in Figure 1-6, grain boundary diffusion and volume diffusion from the grain to the neck are the most important mechanism for material densification. Other mechanisms such as surface diffusion, for example, promote coarsening, which is defined as grain growth coupled with pore growth. As a consequence, the grains grow without material densification.[85,110]

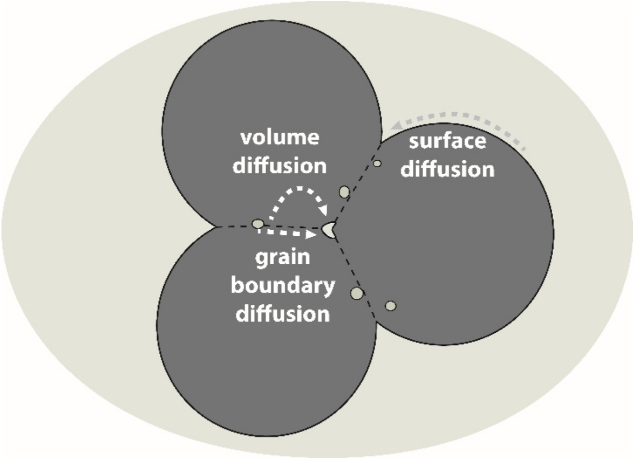

Figure 1-6: Schematic of mass transport paths during grain growth. Grain boundary and volume diffusion are the most important mechanisms for material densification.

1.3 CERAMIC BONE GRAFTS IN SITU

Ceramic bone grafts implanted to bone are exposed to a dynamic physiological environment, which can cause changes in graft properties [111]. The body fluid consist of water, complex compounds, dissolved oxygen, large amounts of sodium and chloride ions and small amounts of other electrolytes. Thus, ceramic bone grafts are constantly bathed in extracellular tissue fluid, which is a harsh environment with a NaCl content of 0.9% at pH 7.4 and a temperature of 37±1°C.[112] Additionally, osteoclasts attach to the bone surface during bone regeneration and resorb bone by secreting hydrochloric acid to dissolve hydroxyapatite.[26,32] This process can cause acidification of the microenvironment and pH values as low as 3.6-4.5 can be present.[113,114] If ceramics are exposed to an acidic environment, corrosion in the form of ion leaching and dissolution can occur.[115] Because hydrogen activity is the driving force for the corrosion, ion leaching and dissolution strongly depend on pH. Corrosion in ceramic bone grafts is mainly concentrated in amorphous grain boundaries. The consequence of grain boundary corrosion is a dramatic loss in compressive strength which further increase the risk of failure for bone regeneration.[111] Thus, grain boundary composition is of special interest when bone grafts are exposed to an acidic environment.

Grain boundaries exhibit different properties and chemistry than the bulk material. Combined with a lower atomic density, grain boundaries are much more open, compared to the bulk material. During the last step of sintering, the amount of micro-pores is reduced. However, a small amount of pores remain and cause a larger surface compared to grains. The higher the micro-porosity in the grain boundaries, the higher the surface exposed to the acidic environment and the higher the corrosion. Furthermore, the presence of other phases is special for ceramic grain boundaries. During sintering of the material, a second or third phase can occur within the grain boundaries and remain there afterwards. Especially in oxide ceramics, glass (SiO_2) is often present at grain boundaries. This strongly affects the mechanical properties and can influence the corrosion resistance of the ceramic as well.[107] The structure of ceramic grain boundaries is complex and depends on several factors. Impurity segregation to grain boundaries from the bulk material, for example, leads to further change in grain boundary composition and corrosion resistance.[107] Because of the dependency of grain boundary porosity and thickness on corrosion, the investigation of these regions is of special interest when considering ceramic bone graft materials.[116]

2 RESEARCH CONCEPT

Because of their high porosity and interconnected pores, TiO_2 bone scaffolds have shown potential as successful support structures for bone regeneration.[117-120] Viable bone tissue is formed within the entire scaffold structure, confirming the osteointegrative and osteoconductive capacity of TiO_2 scaffolds in vivo.[117,119] However, the production of these scaffolds is a complex and time-consuming process because of the TiO_2 raw powder cleaning and double coating process required to produce high strength porous scaffolds. Due to the powder cleaning, soluble impurities are removed from the TiO_2 raw material prior to slurry preparation. Slurries fabricated with cleaned powder have shown appropriate rheology properties such as high viscosity and shear-thinning behavior, which were shown to directly influence scaffold properties.[81] Furthermore, a ceramic double coating is necessary to achieve sufficient mechanical strength to withstand clinical loading.[119] However, dissolution of an amorphous impurity phase at the grain boundaries observed in vitro[111] can result in dramatic loss of strength during bone regeneration and prevent successful bone formation.[47]

To simplify the slurry production, additional ions can also be deliberately added into the ceramic suspension to control and optimize the slurry rheology. The electrical double layer may be decreased when the ionic strength is increased, which could cause lower ζ potential and lower repulsive forces. To optimize the slurry rheology, decreased repulsive forces between TiO_2 particles might lead to higher viscous slurries without agglomeration. Furthermore, the optimal slurry could improve the mechanical strength of fabricated scaffolds while simultaneously ensuring high porosity and interconnected pores. Considering the segregation of impurity ions to grain boundaries, slurries doped with specific ions have the potential to form new grain boundary phases which are resistant to grain boundary corrosion. Thus, the evolution and dissolution of new grain boundary phases have to be investigated regarding their effect on important scaffold properties, such as mechanical strength, corrosion resistance and biocompatibility.

2.1 AIM OF RESEARCH

The general hypothesis of this thesis is that cationic doping of TiO_2 slurries enables simple fabrication of biocompatible scaffolds that maintain their high compressive strength after exposure to acidic environment. The general aim is to simplify the existing fabrication process and produce highly porous TiO_2 scaffolds with high compressive strength and to reduce their susceptibility to corrosion in physiological environment without comprising their biocompatibility.

The overall aim was divided into more specific objectives as followed:

Cationic doping of TiO_2 slurries **Paper I**

- Evaluate influence of added cations on ζ potential
- Examine influence of doping on slurry rheology

Doped TiO_2 scaffolds **Paper I-III**

- Characterization of doped TiO_2 scaffolds
- Investigation of grain boundary composition

High compressive strength after exposure to acidic environment **Paper II-III**

- Evaluate corrosion behavior in acidic environment
- Optimization of grain boundary corrosion by changing sintering conditions, and thereby, grain boundary composition
- Ensure sufficient scaffold properties after corrosion

Biocompatibility of produced scaffolds **Paper II**

- Asses biocompatibility of doped TiO_2 scaffolds

2.2 EXPERIMENTAL DESIGN

To investigate the defined specific objectives, an experimental design was developed. A schematic flow chart shows the connection and single steps to prove the hypothesis stated above (Figure 2-1).

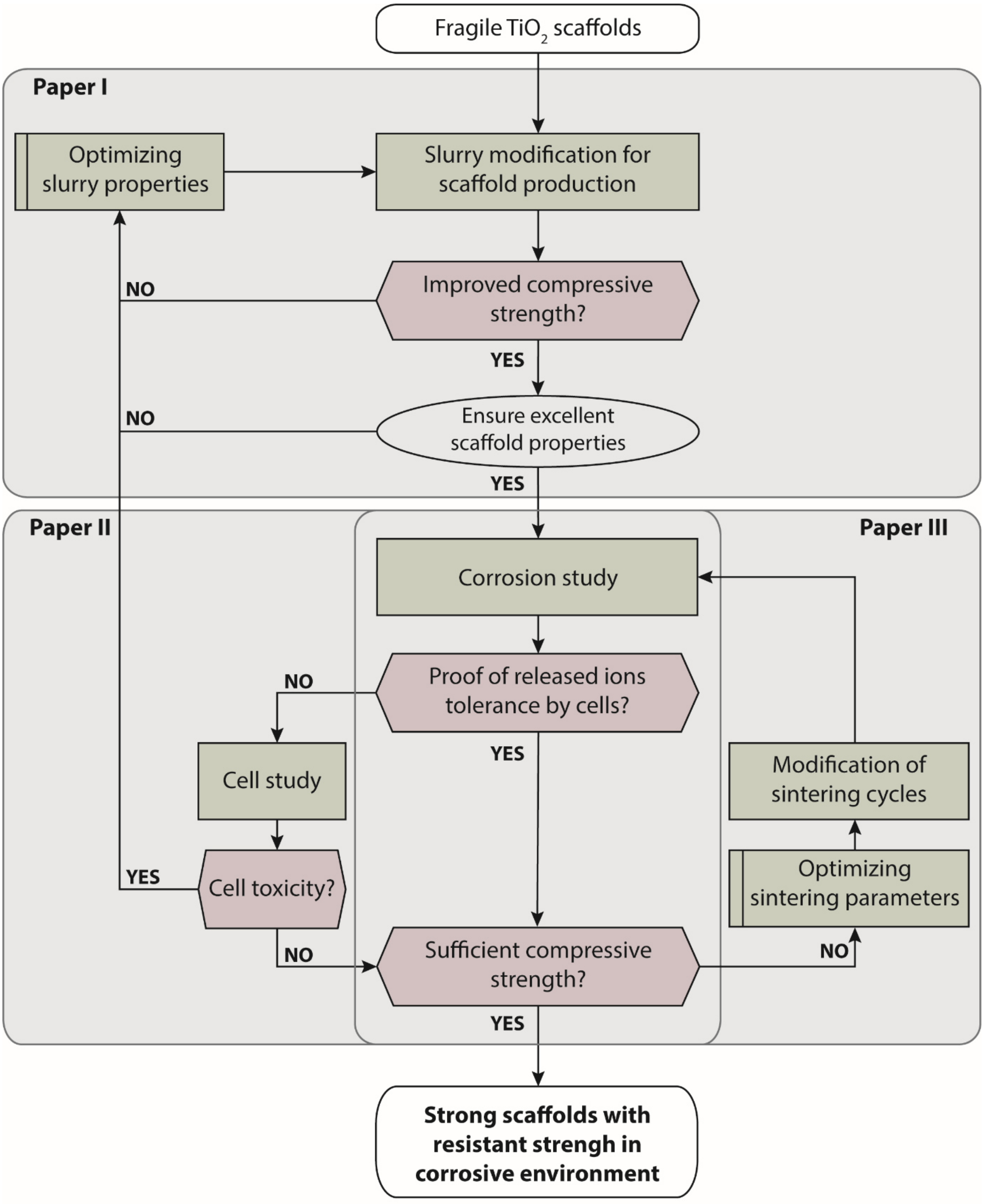

Figure 2-1: Experimental design followed in this thesis to produce biocompatible scaffolds high in compressive strength after exposure to acidic environment

3 EXPERIMENTAL CONSIDERATIONS

3.1 TiO_2 SCAFFOLD FABRICATION

Ideally, the fabrication method for macroporous ceramics produces foams that have controllable pore size and pore shape and that are adaptable to complex shapes. Furthermore, the fabrication process should be reproducible and economical.[121] The replica method, patented by Schwartzwalder and Somers in 1963, fulfills these criteria and has been used to fabricate TiO_2 scaffolds high in porosity and pore size.[106] In this method, polymer foams are coated with a ceramic suspension to replicate their structure. The polymer is burned out at low temperatures and the ceramic is sintered at high temperatures, as shown in Figure 3-1. The replica method is the most common method to produce macroporous ceramics for different industrial applications.[80,122,123] The processing route directly influences the microstructural features of produced ceramic foams. Because the fabricated scaffolds are replicates of the used polymer foams, scaffold properties can be determined by the macroporous foam template.[80] Consequently, the shape and dimensions of the fabricated scaffolds can be easily adjusted by changing the foam shape. Complete evaporation of the polymer foam and the absence of additives result in non-toxic ceramics. Thus, the replica method enables the fabrication of non-toxic ceramic scaffolds with sufficient macroscale properties, which can be used as bone scaffolds in tissue engineering application.[118,124-126]. Further advantages of this method are high reproducibility and cost-effectiveness.

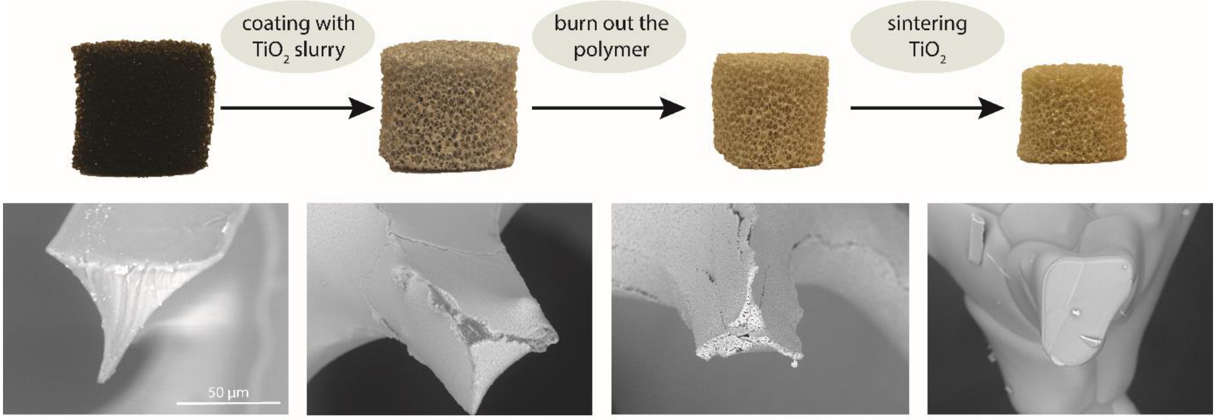

Figure 3-1: Replica method to produce macroporous ceramic bone scaffolds. Polymer foams are coated with a ceramic suspension. The polymer is burned out at low temperatures and the green body is sintered at high temperatures.

3.1.1 SUSPENSION STABILITY

Ceramic suspension properties have been shown to directly influence scaffold properties when using the replica method. Shear-thinning behavior and high viscosity have been shown to improve scaffold porosity, interconnectivity and compressive strength.[81] Suspensions rheology, including as shear-thinning behavior and viscosity, is governed by the suspension stability. A common method to investigate the suspension stability is the ζ potential measurement, in which repulsive forces between charges particles are determined. Additionally, the viscosity can be measured to investigate changes caused by the ζ potential and to guarantee shear-thinning behavior.

To investigate the influence of different electrolytes on TiO_2 slurry properties, the ζ potential as a function of pH was measured by electrophoretic light scattering (ELS). Using ELS, a voltage is applied to the sample and charged particles start to move, as shown in Figure 3-2.[127] A laser beam that scatters depending on the motion of charged particles in the applied voltage is detected. Comparison with a reference beam enables the detection of small frequency shifts depending on the velocity of the charged particles. The measured shift is equal to the velocity and the recorded electrophoretic mobility is thereby directly linked to the ζ potential.[128,129]

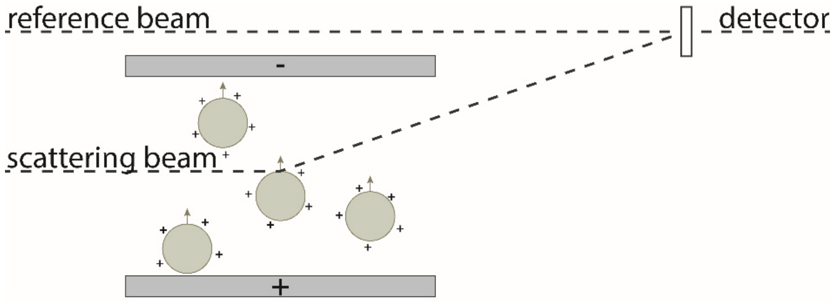

Figure 3-2: Electrophoretic light scattering. An applied voltage causes movement of charged particles, which is depending on the ζ potential of the particles.

As the measurement is based on the detection of the scattered light beam, the sample must be light transparent.[130] As the prepared ceramic slurries were not light transparent due to their high particle content (>70wt%) the measured samples needed to be diluted, and consequently, exhibited a different particle-to-liquid ratio compared to the suspensions used for scaffold fabrication. While the IEP of the tested suspension should not be strongly affected by the measurement conditions, the reproducibility of the measured ζ potentials can be increased by optimizing conditions such as solid-to-liquid ratio and aging.[131] Hence, different liquid-to-particle ratio and aging times were tested to find the optimal measurement conditions which guaranteed high reproducibility of measurements for doped TiO_2 suspensions. The solid content of 25 mg/l in prepared samples showed optimal light transparency and reproducible measurements. The optimal sample aging was different for the measured samples. While all other samples were aged for three days, NaCl samples needed to age for six days to show constant ζ potential for the of dispersed TiO_2 particles. Measurements without aging showed high deviations in ζ potential measurements, while measurements after aging showed high reproducibility. Feasible surface reactions could cause different surface charges and thus differences in ζ potentials. Due to aging of prepared samples, possible surface reactions were completed and caused stable surface charges und ζ potential measurements. The optimal solid content (25 mg/l) and aging (3-6 days) showed reliable results in high reproducibility and were chosen for the performed ζ potential measurement.

To be able to measure the ζ potential as a function of pH, the pH of the sample has to be changed during the measurement. Changing the pH of the prepared samples involves a change in ionic strength. The complex surface reactions depend on the titration direction and titration time, which causes a hysteresis effect.[132,133] Thus, the ζ potential and the measured pH_{IEP} can differ between samples titrated from low to high pH values or vice versa.[134,135] To minimize this hysteresis effect, separate samples were measured for acidic and basic pH values. Starting from the native pH of the suspension (pH 5-9, depending on used electrolyte), HCl was added to reach acidic pH values (≈pH 1.7). NaOH was used to titrate the measured samples to basic pH values (≈pH 9). The presented ζ potential curve for each suspension represents the average of three measurements of three completely independent suspensions for each titration direction.

As mentioned before, the IEP remains mostly unaffected by sample preparation. However, the influence of different ions on the electric double layer, and thus, ζ potential dependent on the particle-to-ion ratio.[104] Thus, the measured ζ potential value is expected to differ between the measured samples (highly diluted slurries) and the ceramic slurries prepared for scaffold production. To measure the ζ potential of TiO_2 particles in highly concentrated slurries as close to the native slurry conditions as possible using ELS, the ζ potential measurement of the supernatant from the slurry was performed. For this purpose, prepared slurries were centrifuged for 15 min at 5500g. To avoid influences caused by other ions than the ions present within the suspension, the ζ potential was measured at the native slurry pH. Consequently, any influences caused by titration and the addition of HCl and NaOH were eliminated. To compare the measured titration curve and the supernatant measurement, a second slurry for each group at a higher pH was mixed and measured.

The performed sample preparation and the used technique provided valuable results to explain the general influence of different ions on slurry behavior and ζ potential of TiO_2 particles. However, only an assumption regarding the ζ potential in the ceramic slurries can be made because of the large differences in particle concentration between the measured samples and the slurries used for scaffold production. Thus, the transfer of results between the two samples is limited as changes in particle-to-ion ratio and different EDL thicknesses can cause discrepancies in the measured and true ζ potential values in the slurry.

Another technique available for measuring the ζ potential in ceramic suspensions would be the electroacoustic method. Using this technique, the electric sonic amplitude of charged particles, which depends on ζ potential, is measured. The advantage of this method is that a particle ratios up to 40 wt% can be measured because light transparency of the sample is not necessary.[136,137] Although higher particle-to-liquid ratios can be measured, the direct measurement of highly concentrated slurries is still not possible. Consequently, the use of electroacoustic method would not prevent the need for sample dilution the same limitations caused by sample dilutions apply for both techniques. Nonetheless, the electroacoustic technique could have been used to confirm results of the supernatant measurements.

3.1.2 SLURRY VISCOSITY

The measurement of the ζ potential depending on electrolytes was used to investigate the suspension stability in highly concentrated ceramic slurries. Forces between dispersed particles are responsible for the characteristic flow behavior of the suspension. Thus, the ζ potential can be used to determine the repulsive forces between the particles. When the ζ potential, and thus, the repulsive forces between the particles is high, particle agglomeration in the suspension is prevented. Agglomeration has a pronounced effect on the flow behavior of a suspension, typically resulting in an increased viscosity.[138] Consequently, the measurement of the flow behavior of the produced doped slurries was used to indirectly confirm the slurry stability. To monitor changes in flow behavior depending on the chloride salt and its concentration, the viscosity of the prepared slurries was measured as function of shear rate. The slurry was exposed between two concentric cylinders. The inner cylinder was rotated at different speeds (ranging from 2.46-100 1/s) while the shear rate, shear stress and viscosity were recorded.

Best fit rheological model analysis was done by using standard Bohlin viscometer software to confirm shear-thinning behavior of doped and undoped ceramic slurries. The used setup showed a high surface area in contact with the tested material and is therefore accurate and reliable measurements even at low shear rates and viscosities. Further advantages of this technique is the use of the same slurry for viscosity measurement and scaffold production.

3.2 SCAFFOLD CHARACTERIZATION

3.2.1 PORE ARCHITECTURE AND MICROSTRUCTURE

Bone ingrowth and vascularization within the scaffold are crucial for bone regeneration. Previous studies have shown that pore size, interconnectivity and porosity are some of the most important scaffold properties for bone ingrowth.[49,139] While scaffolds with small pores showed the ingrowth of unmineralized and fibrous tissue, scaffolds with larger pores showed substantial ingrowth of bone.[140,141] Thus, pore size can directly influence the tissue formation within the scaffold.[83] A minimum pore size of 100 µm is known to be required for the formation of an osteon, and thus, the possibility of vascularization. To enhance new bone formation pore sizes between 300-400 µm are recommended.[82,142-144] Consequently, the characterization of the pore size of the fabricated scaffolds is of special interest. Therefore, microcomputer tomography (microCT) was used to compare doped scaffold to undoped scaffolds and to analyze the influence of slurry properties and sintering conditions on scaffold properties.

Using microCT, X-rays are emitted by a source and pass though the sample material. The attenuated beam is detected and a 2D image recorded. Different 2D images taken from different angles can be combined to a 3D model. On the basis of this 3D model, the scaffold parameters, such as porosity, pore size and strut thickness, can be calculated, as shown in Figure 3-3. All these properties can affect mechanical properties of the scaffold, the possibility of vascularization and the formation of new bone.[83] Advantage of this technique is the non-destructive measurement of several scaffolds at the same time. Thus, the same samples that have been scanned can be used for further investigations, for example, mechanical testing and electron microscopy. This enables the correlation of small variations in scaffold features on the compressive strength of the produced scaffolds.

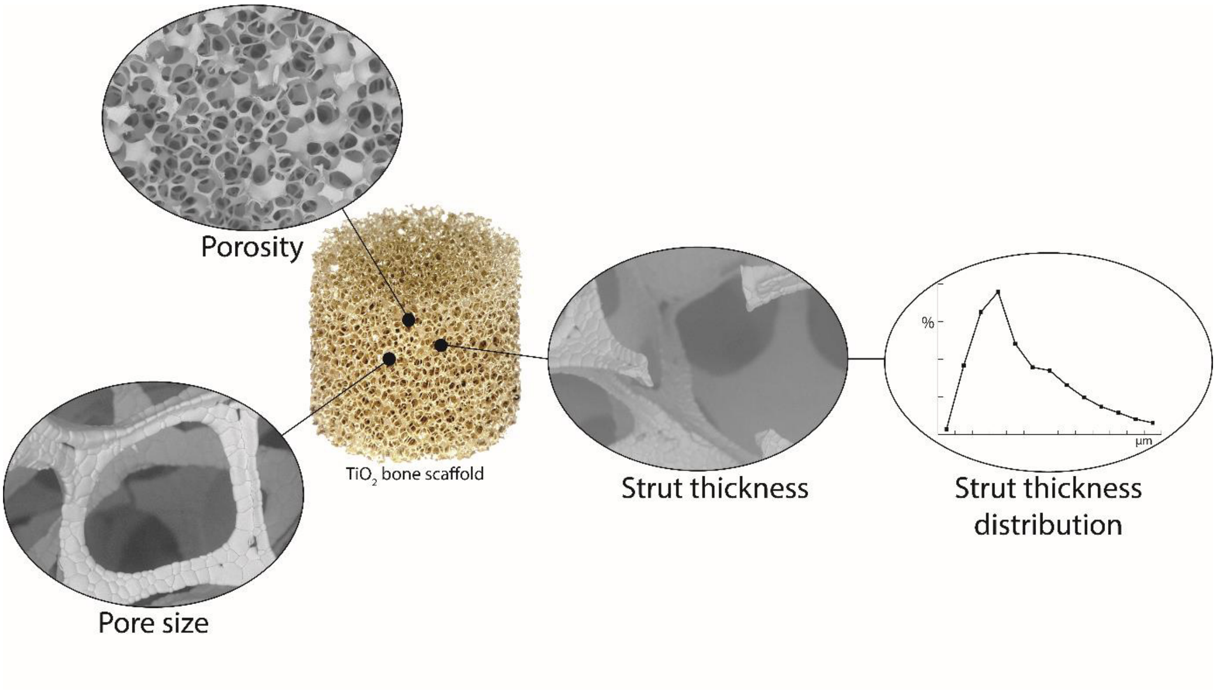

Figure 3-3: Porosity, pore size and strut thickness as important scaffold properties calculated with the microCT.

The calculated values for the key pore architectural properties of the scaffold enables the comparison between differently doped scaffolds and the influence of sintering and slurry conditions on the scaffold microstructure. Although microCT is a very powerful technique, because of the simple sample preparation and the non-destructive sample characterization, the use of other techniques is also necessary to confirm and expand the microstructural evaluation of the scaffolds. For example, when evaluating the strut thickness in TiO_2 scaffolds, the average strut thickness calculated based on the microCT data does not provide enough information about the strut architecture. Figure 3-4 illustrates the relationship between calculated average strut thickness (dashed line) and strut architecture. Despite the fact that all three struts exhibit a different strut architecture, the calculated average strut size based on microCT data is similar, as demonstrated with the dashed line. Thus, scanning electron microscopy (SEM) was used to evaluate changes in the strut architecture of the doped TiO_2 scaffolds. Although no exact quantitative values of strut diameter are available using SEM, the combination of microCT data and SEM can be used to investigate changes in scaffold properties, such as compressive strength. To analyze influence of doped suspensions on homogenous foam coatings, the strut thickness distribution calculated from the microCT data was used. The calculated strut thickness distribution shows the distribution as a function of strut thickness. Due to this distribution, the peak position and peak width (narrow vs. wide range) gives information about homogenous struts and the amount of blocked pores.

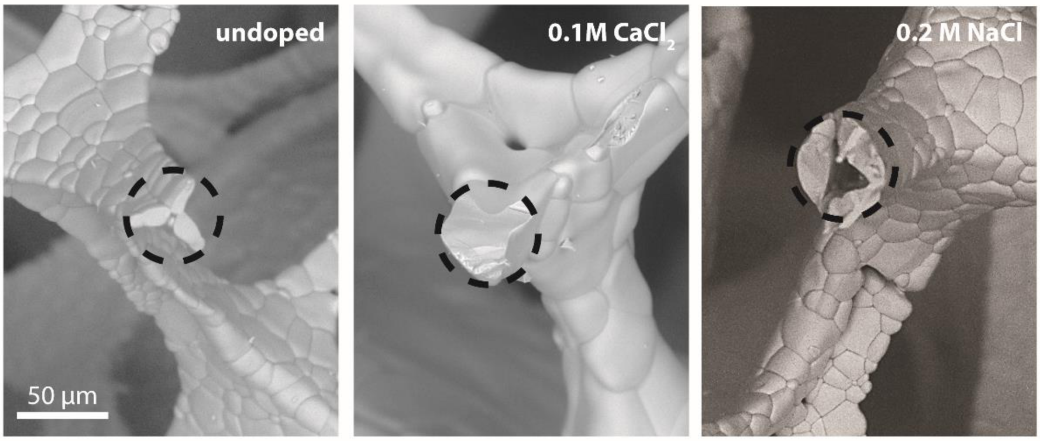

Figure 3-4: Strut thickness in differently doped TiO_2 scaffolds. While the calculated strut thickness average (dashed lines) is similar using microCT, SEM images show differences in strut morphology.

SEM imaging can also be used to analyse the influence of changes in the sintering conditions on grain growth in the doped TiO_2 scaffolds. For this purpose, an image analysis algorithm was used to detect differences in grain size in SEM images of locally flat areas on the scaffold struts. Thus, different areas of three independent scaffolds were used to calculate the grain diameter of more than 30 grains in total to further calculate the average grain diameter. Since the detection of grains using the algorithm is dependent on contrast between the grain boundary and bulk material, the used SEM image has a high impact on the quality of the results. The depth of field, and thus, the focus of the used images is limited to small regions and affects the sharpness and the contrast between grain boundaries and the bulk material.

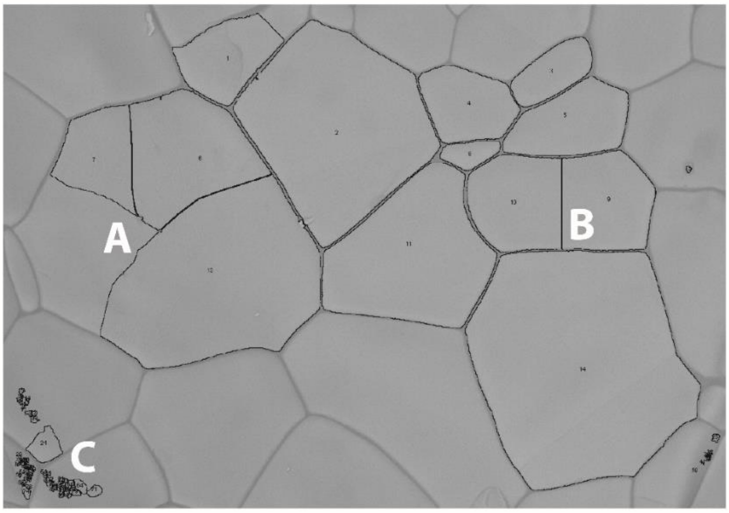

Figure 3-5: Different detection artefacts when using an image analysis algorithm for grain size calculation. The contrast-dependent detection of grains can cause incomplete detection of a grain (A), the division of a single grain into several grains (B) or a combination of both (C).

The resulting artefacts are shown in Figure 3-5. Possible artefacts were grains that were not fully detected (A), the separation of one grain in several smaller grains (B) or the combination of both (C). While artefacts A and C were discarded, B could be manually corrected. Using an image analysis algorithm, a fast and easy first estimation of the overall grain size enables the comparison of grain growth in differently treated scaffolds produced using different processing parameters.

3.2.2 MECHANICAL PROPERTIES

Compressive strength was stated as one of the most important scaffold properties to improve within this study. Consequently, the mechanical characterization of these scaffolds is an important element of scaffold characterization. A stress-strain diagram of porous materials shows typically three different sections: a linear elasticity phase, a plateau phase and further densification, as shown in Figure 3-6. After first struts collapse, a decrease in compression and a plateau stress is present while the strain further increases. Because of the densification of the material, the compression increases again until total failure of the scaffold. The calculated strength was taken at the end of the linear elasticity phase, as highlighted in Figure 3-6. Using a previously established method for compressive testing of TiO_2 scaffolds enables direct comparison of compressive strength results for the doped TiO_2 scaffolds to previous findings.[81,111,145]

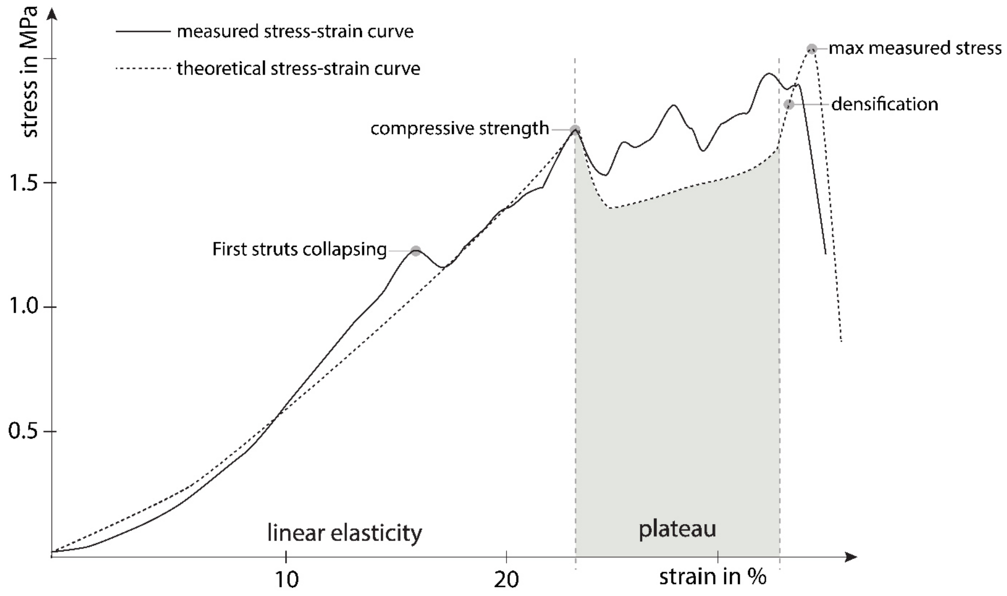

Figure 3-6: Stress-strain diagram of TiO_2 bone scaffolds. After first struts collapse, the stress is further increased until the maximum compressive stress is reached. The densification of collapsed struts causes a plateau phase and further increase in measured compressive stress.

3.2.3 CORROSION TEST

Scaffold strength is an important parameter during bone remodeling to support bone to form and remodel. Especially during the first phases, where injured bone is resorbed and new bone forms, an acidic environment can be present and influence scaffold strength by grain boundary dissolution, as shown in Figure 3-7.[111] During inflammation, macrophages and osteoclasts are present at the defect site and can cause a drop in local pH to values of 3.0 - 3.7.[114] To simulate this pH drop and to investigate the effect of grain boundary corrosion on the compressive strength of the doped scaffolds, the scaffolds were exposed to 1 mM HCl (pH 3) at 37°C under static conditions. To investigate corrosion in a neutral environment, scaffolds were exposed to deionized water (dH_2O) as well. Different time points were chosen to evaluate time dependent dissolution effects. After corrosion test, scaffolds were rinsed with dH_2O and dried for 24 h at 37°C before further characterization and measurements were performed. The compressive strength of corroded scaffolds was used as the main indicator to determine corrosion. For further investigation regarding details of grain boundary dissolution in different treated scaffolds, SEM images and EDX were used.

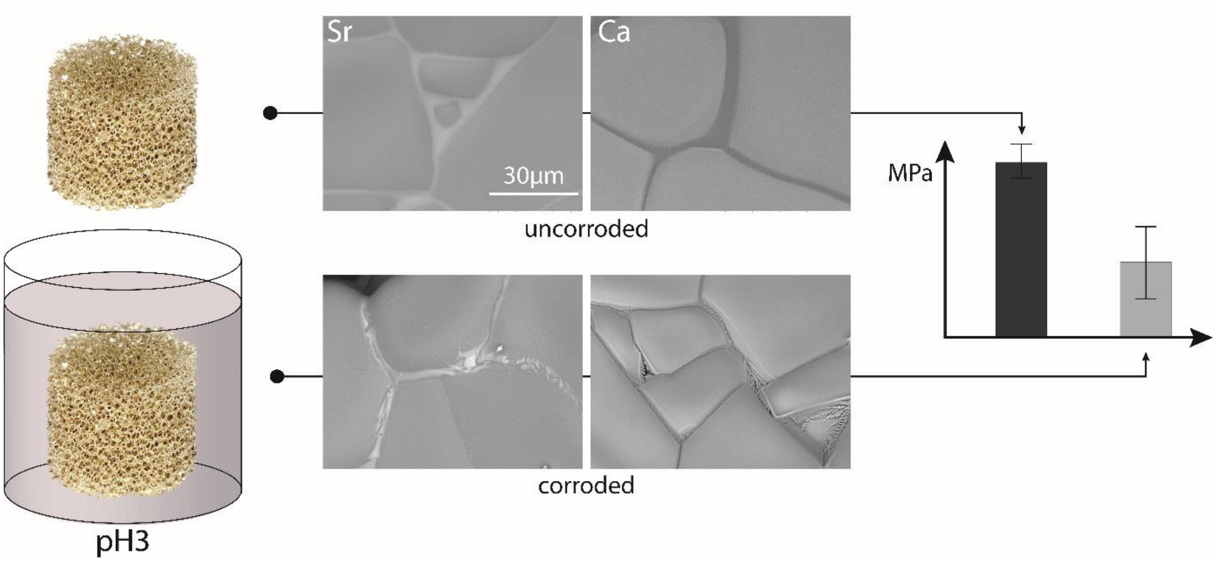

Figure 3-7: Corrosion in doped ceramic scaffolds. A decreased compressive strength was used to determine corrosion, while SEM images showed dissolution concentrated in the grain boundaries.

3.2.4 ATOMIC ABSORPTION SPECTROSCOPY

Corrosion in polycrystalline ceramics occurs by ion dissolution that is typically concentrated in the grain boundaries.[111] As shown in Figure 3-7, grain boundary dissolution was present in acidic solutions. Therefore, the concentration of released dopant ions from grain boundaries present in the liquid can be quantified. Atomic absorption spectroscopy (AAS) was used to measure the release profile of these ions and further quantify and characterize the magnitude of the dissolution in grain boundaries. Using this technique, samples are vaporized. The existing free gaseous atoms absorb electromagnetic radiation at an absorption wavelength that is specific for each atom. Because of a proportional correlation between the absorption signal and the atomic concentration, the number of atoms of interest present in the sample can be determined.[146] To analyze the ion-release profile as a function of time, corrosion samples were prepared for each time point and thus a cumulative presentation was chosen.

Disadvantage of this method is the limitation of atoms which can be detected using AAS. Metalloids, for example silicon, have a high electronegativity, which leads to high ionization.[147] Consequently, resonance lines are at very short wavelengths and the potential of interferences with emission from the atomizer are significantly higher.[148,149] Silicon has been shown to be present in TiO_2 grain boundaries and released after corrosion.[111] Determining a silicon release profile for all the doped TiO_2 scaffolds could give more information about their grain boundary chemistry and the dissolved phase after corrosion. However, the inadequate detection of silicon was also observed for other spectroscopic techniques such as ICP-MS.[150]

3.3 GRAIN BOUNDARY INVESTIGATION

Grain boundaries are of special interest in ceramics, because of their influence on mechanical properties. Especially when ceramics are used as porous bone scaffolds, most grain boundaries are exposed to the corrosive environment due to the high porosity and high surface area-to-volume ratio. Corrosion in ceramics is typically concentrated in the grain boundaries. Thus, grain boundary dissolution is the most important influence on the corrosion behavior. Evaluating grain boundaries is of special interest to investigate differences in the corrosion mechanism. However, the investigation of grain boundaries is still a big challenge. Because of the small volume of grain boundaries compared to the large volume of grains within the scaffold, some techniques and their analytical capability are not specific enough to investigate the influence of dopants on grain boundary formation and dissolution. X-ray diffraction (XRD), for example, could give information about new phase formation within the grain boundaries by detecting crystal structures. In this technique, scattered x-rays are detected. Constructive interference of scattered x-rays is detectable when x-ray wavelength (λ), beam angle (θ) and crystal plane distance (d) satisfy Bragg's law (Figure 3-8).[151] Thus, the diffraction pattern is depending on the specific crystal structure and gives information about the crystallographic phases within the sample.

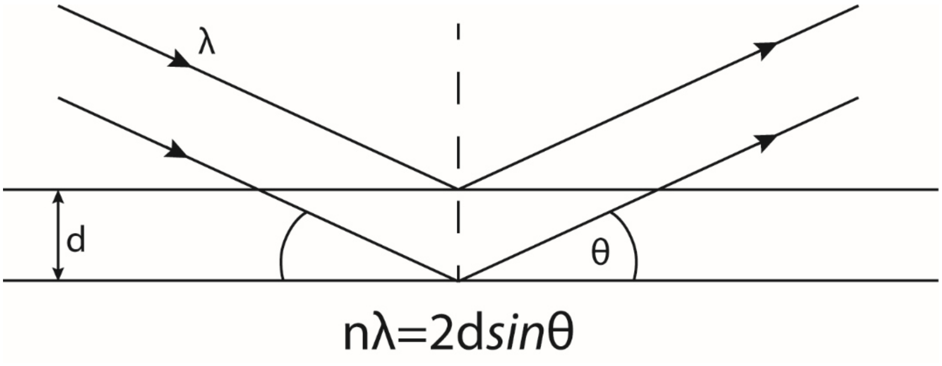

Figure 3-8: Constructive inference occurs when x-ray wavelength (λ), beam angle (θ) and crystal plane distance (d) satisfy Bragg's law.

However, a strong TiO_2 signal caused by the large number of bulk grains overlaps a possible low signal of crystals within the grain boundary. Thus, the spatial resolution of this technique is not sufficient to focus on the investigation of very small areas within grain boundaries instead of the bulk material. Other techniques such as energy dispersive x-ray spectroscopy (EDX), for example, showed the same challenge as XRD. The high grain-to-grain boundary ratio leads to overlapping of signal sources. For the investigation of very small regions of interest, a transmission electron microscope (TEM) can be used. Consequently, a combination of SEM, TEM and EDX was used in the present study to evaluate grain boundary composition and dissolution.

3.3.1 ENERGY DISPERSIVE X-RAY SPECTROSCOPY

EDX is an effective and simple tool to detect elemental compositions in grains and grain boundaries. While SEM uses backscattered or secondary electrons to detect an image of the sample surface, EDX uses the x-ray continuum generated by an electron beam. The primary electron beam displaces inner shell electrons of atoms within the sample. To form a charge balance, electrons from the outer shells fall to the inner shells and x-rays with element specific energies are emitted. With EDX, the energy of emitted x-rays are measured and can be referred to the elements present in the sample.[152] The advantage of this technique is that elements in large areas can be investigated at high spatial resolution via elemental mapping. In combination with SEM, the investigated area is defined and location information about grain boundaries is available. With mapping, the distribution of ions in grains and grain boundaries can be detected as shown in Figure 3-9.

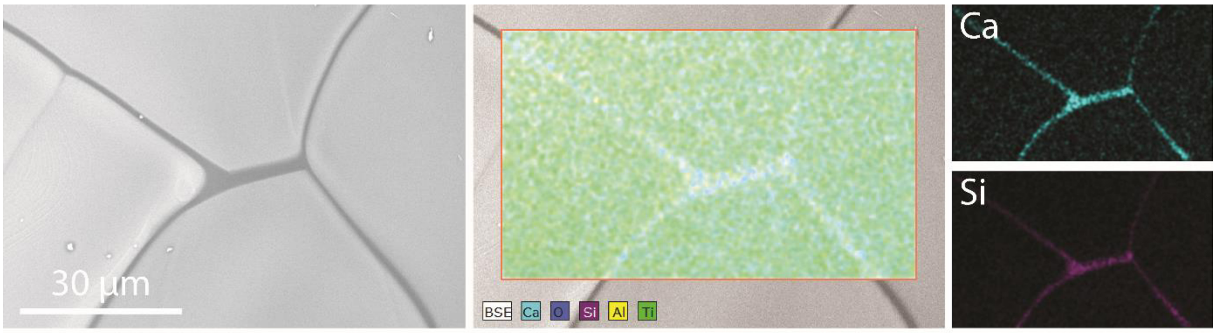

Figure 3-9: EDX mapping is used to investigate elements present within the sample. While Ti is highly concentrated within the grains, Ca and Si are highly concentrated in the grain boundaries.

While elemental mapping is a very easy and powerful technique to detect different ion ratio in the grains and grain boundaries, further investigations of composition within the grain boundaries using EDX did not show high accuracy. As shown in Figure 3-10, a line scan can be detected along grain boundaries. When the distance between regions of highly concentrated ions is large enough (A), these ions and their concentration along the scanned line can be detected. However, when the features are too close together, resolution for the location information for the atomic concentration is not sufficient anymore (B)

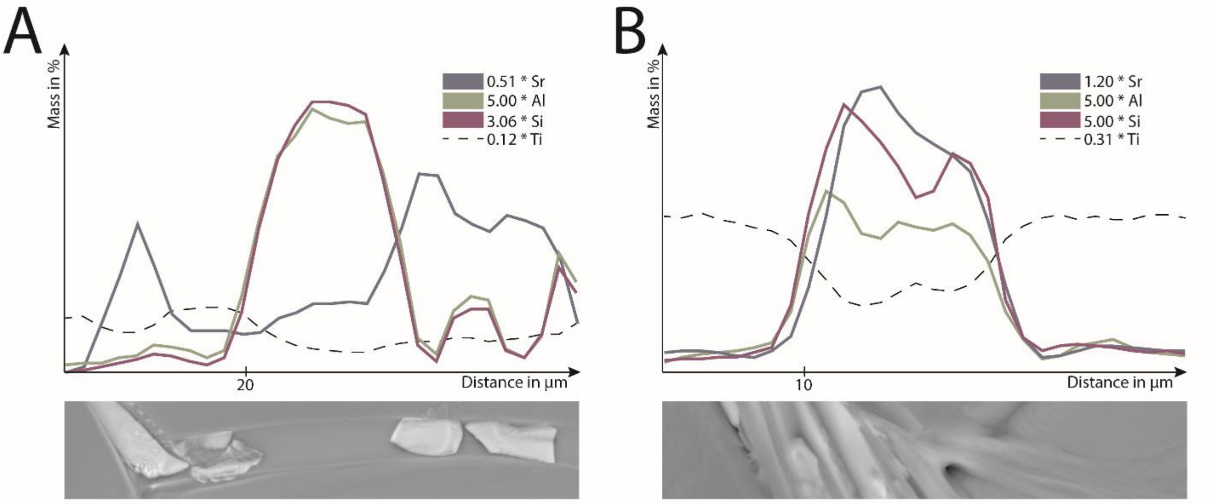

Figure 3-10: Line scan of grain boundaries in doped TiO_2 scaffolds. Zoom factor of signals are used to intensify the local differences in elements and are shown in the legend. The distance between crystals is sufficient to detect differences in ion concentration distribution (A). While higher Sr, Al and Si signals identify typical doped grain boundaries, differences in signals are not sufficient to investigate the crystalline phase within the grain boundary.

The photons detected by EDX originate from deeper regions than the electrons used for SEM. When analyzing grain boundaries, the information about the third dimension of the investigated grain boundary is unknown. Thus, the signal detected with EDX can originate from a different area of the analyzed sample volume than the intended volume of interest, as shown in Figure 3-11.

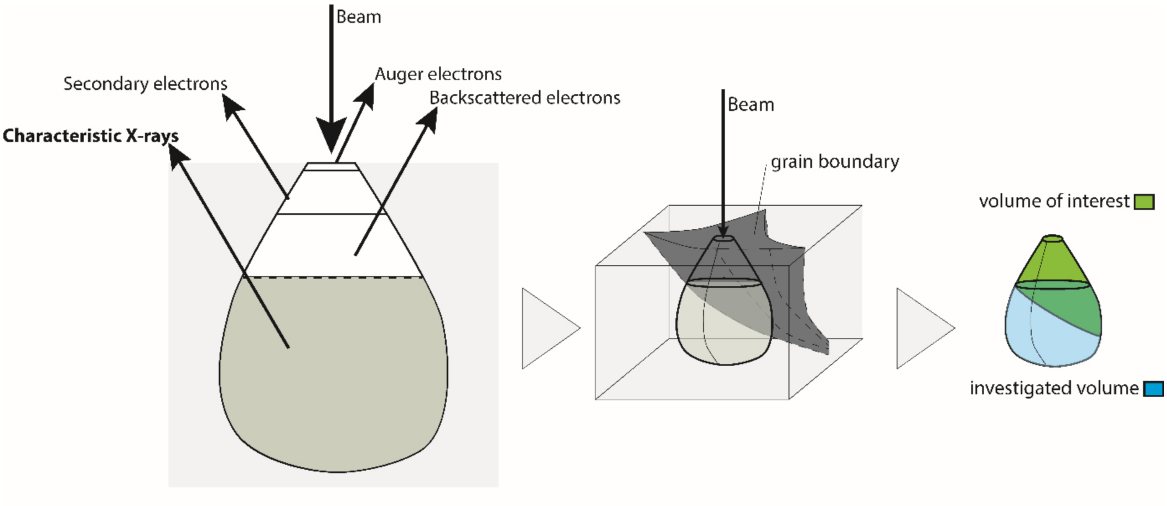

Figure 3-11: Problem of 3D information and region of emitted photons for EDX. The investigated volume can differ from the volume of interest. Consequently, signals from the grains can overlap the signals from the grain boundaries.

Although the electron beam is focused within a grain boundary, the detected signal can originate from underlying grains or other parts of the grain boundary. The detected signals from both the grain boundary and its neighboring region are overlapping and not strong enough for an accurate analysis. By changing the voltage of the incident beam, the interaction volume of the electron beam can be altered. Thus, lower voltages are causing a smaller interaction volume from which signals are detected. However, measurements using different acceleration voltages did not show any change in the EDX results.

3.3.2 FOCUSED ION BEAM AND TRANSMISSION ELECTRON MICROSCOPY

The resolution of the used method limits the size of the region that can be investigated. SEM and EDX were shown to be very effective methods to investigate grain boundary phases. However, a limitation for these techniques is the overlapping of signals from grains and grain boundaries. Therefore, TEM was used to investigate thin sections of the grain boundary region at high spatial resolution and to circumvent the problems associated with the large interaction volume of the electron beam when using SEM and EDX. However, the main advantage of using TEM to investigate the grain boundaries is that electron diffraction patterns of very small defined regions can be collected, and thus, the different phases present in the grain boundary can be determined. Using the diffraction mode of TEM, an incident electron beam is directed into a material and the outgoing scattered beam is detected in direction and intensity. Electrons interfere constructively or destructively depending on the crystal structure. Constructive interference is described by Bragg's law and shown in Figure 3-8.[153] As shown in Figure 3-12, different diffraction patterns of selected areas (SAP) are available due to tilting the sample towards the electron beam. The specific diffraction pattern and the known tilt angle of the crystal enables the determination of the crystal itself.[154,155] The advantage of TEM is that images and diffraction patterns of the selected area are available. Thus, crystalline phases (SAP1) and amorphous phases (SAP2) within the TEM sample can be directly assigned within the sample (Figure 3-12).

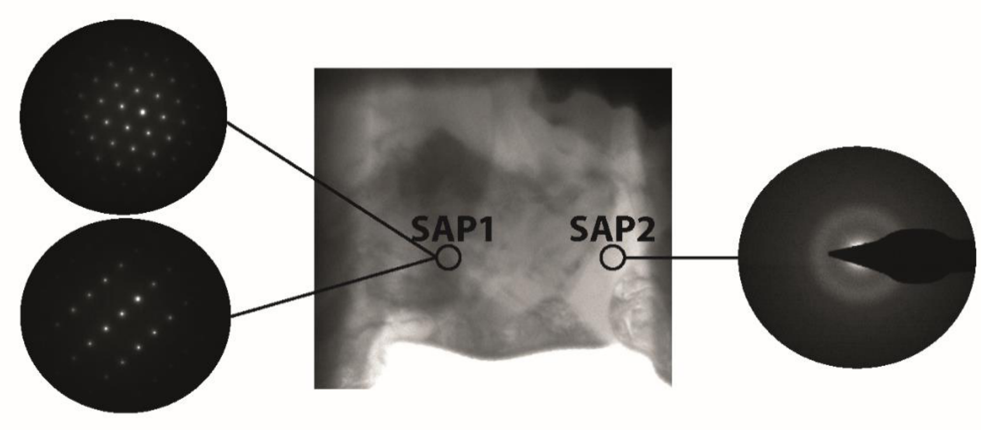

Figure 3-12: Identification of different phases present in a TEM sample via diffraction mode. While SAP1 shows diffraction pattern of two different angles of the same crystal, SAP2 indicates an amorphous phase.

Diffraction can only occur, when electrons are able to pass through the material. Thus, samples should exhibit a maximum thickness of 100 nm to ensure electron transparency. Although several techniques to prepare TEM samples are available, the preparation of very thin samples is very challenging for highly porous, brittle materials. The most typical preparation techniques for TEM samples are cutting or grinding of the sample, combined with a final thinning procedure with ion beam milling or electro-polishing.[156] However, cutting and grinding techniques are not applicable for highly porous TiO_2 scaffolds. For brittle materials such as ceramics, cutting is not an option. Even when highly porous scaffolds are embedded in a support structure, for example a resin, the uncontrolled material failure of the ceramic during cutting due to the brittleness of the material results in an unspecific sample for further investigations. In contrast, grinding is, in general, an easy technique to prepare thin TEM samples of ceramics. Because of the highly porous structure of TiO_2 scaffolds, grinding causes uncontrolled damage to TiO_2 struts. To stabilize porous ceramic structures and thus prevent of uncontrolled damage, the sample can be embedded into resin. However, the control of selecting the areas within the TEM samples is very poor when using grinding. Consequently, it is impossible to guarantee the existence of a grain boundary, the very small region of interest compared to large TiO_2 grains, within the prepared section. Thus, the use of grinding as TEM sample preparation is rather recommended for investigation of the bulk material, because of the very low chance that thin TEM samples prepared by grinding contains a grain boundary.

A technique that allows more control of the region of interest within the prepared TEM sample is focused ion beam (FIB) milling using a SEM combined with an ion beam [154]. The advantage of using this technique is that the location of the TEM sample can be directly controlled. Highly porous scaffolds need to be embedded into resin to fill the open porous structure and guarantees flat surfaces, which are crucial for imaging (SEM) and cutting out the TEM sample (FIB). Furthermore, the use of ions to cut out a region of interest requires electron conductivity as charging could distract the focused beam and cause damage to the sample. Therefore, the scaffolds were embedded into a graphite-loaded resin to ensure sufficient electron conductivity. As shown in Figure 3-13, grain boundaries can be detected within the cross section of the scaffold section (A). An ion beam is used for milling areas next to the area of interest (B). After removing the material around the region of interest, a lamella is formed (C). When the gas tungsten is present within the FIB chamber, the ion beam can be used for deposition as well. This is used for the fixation between a nanomanipulator and the prepared lamella. After this fixation, an undercut and the final cut to separate the lamella from the bulk material is performed (dashed lines Figure 3-13C). The lamella is then fixed to a TEM grid using tungsten deposition, which enables the transportation between FIB and TEM, and furthermore, inserting the sample to the TEM. The last important step is to thin the lamella with ion beam milling to ensure electron transparency (D).

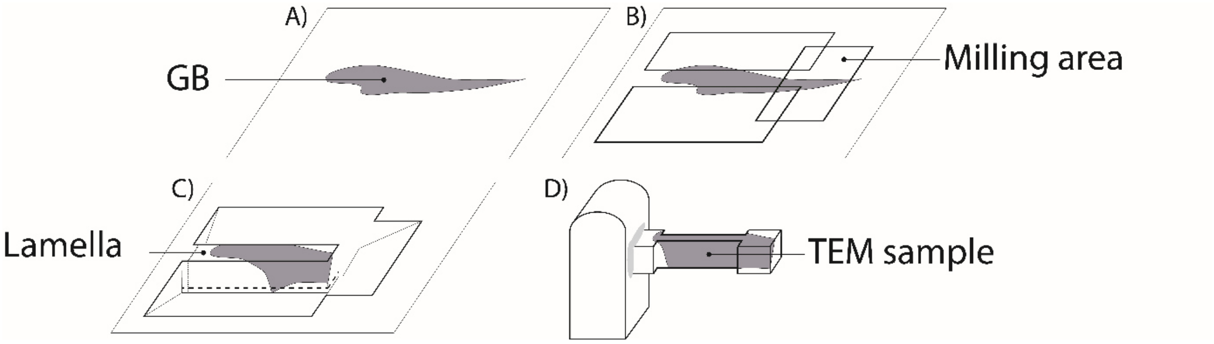

Figure 3-13: TEM sample preparation by using FIB. The area around the grain boundary (A) is removed by milling (B) and a lamella forms (C). Further milling reduces sample thickness (D)

3.4 BIOLOGICAL COMPATIBILITY

Based on previous studies, corrosion in TiO_2 scaffolds can cause the release of impurity ions which may influence the biocompatibility and osteoconduction of the fabricated scaffolds.[111] Thus, it is important to consider the biological compatibility to the doped TiO_2 scaffolds. If the material or parts of it harm the surrounding tissue, regeneration is not possible. The undoped TiO_2 scaffolds have been shown to sustain growth of MC3T3 cells of an osteoblast precursor cell line towards a differentiated state.[157] However, to guarantee the biological compatibility of doped TiO_2 scaffolds, the influence of ions released from the doped scaffolds on cell toxicity must be investigated. Therefore, human adipose-derived stem cells (hASCs) were cultured in the doped TiO_2 scaffolds. For all cell experiments, undoped scaffolds were used as a control. hASCs were used because of their easy access from the human body. Considering future applications, hASCs are simple to isolate from human adipose tissue and could be used for pre-cultivation of ceramic scaffolds to generate implantable osteogenic grafts.[158]

3.4.1 CYTOTOXICITY

Cytotoxicity test is an in vitro test to determine cell death caused by toxic substances released from the material or by direct contact between cells and material.[159] Thus, the measurement of an intact cell membrane, which is crucial for cell viability, is fundamental for several cell cytotoxicity tests. Lactate dehydrogenase (LDH), for example, is an intracellular enzyme, which is present in almost all cells and is released to the extracellular medium, when the cell membrane is damaged. Because cell membrane damage correlates with cell death, LDH activity is an indicator of cell viability. LDH catalyzes the oxidation of lactate to pyruvate by the reduction of NAD^+ to NADH. Hence, the amount of released LDH can be quantified by measuring the concentration of NADH. Because of spontaneous cell death caused by apoptosis, the spontaneous LDH released is used as a negative control. The positive control is the LDH amount after cell membrane damage using a surfactant, for example Triton X. Thus, LDH release and cytotoxicity are depending on spontaneous and maximum LDH activity.[160,161]

Live/dead stainings can be used to verify LDH results. Using calcein AM and propidium iodide (PI), living cells can be stained green and dead cells appear red under a confocal microscope. Calcein AM is a cell membrane permeable dye that is converted to green fluorescent calcein after intracellular hydrolysis. PI is membrane impermeable and generally excluded from viable cells. When the cell membrane is damaged, the PI is present inside the cell, binds to DNA, and thus, cell death can be identified.

However, both methods give information about the membrane integrity. Thus, further assays are necessary to evaluate metabolic activity of cells seeded on doped TiO_2 scaffolds. To get more information about cell viability, alamarBlue assay can be used. Resazurin-based alamarBlue molecules added to the cell culture change their color depending on cellular metabolism. Thus, the fluorescence of the media is directly proportional to cellular metabolism and an indicator for cells health. Although this method provides valuable complimentary information about the influence of the doped scaffolds on cell viability, it was not possible to implement this method in the present work. The results of the alamarBlue assay revealed that alamarBlue solution was not homogenously distributed within the cell culture media inside the complex pore structure of the scaffolds. Difference in concentration inside and outside of the scaffold could be detected, causing large variations in the measured fluorescence. Consequently, alamarBlue could not be use as an indicator for cellular metabolism in the cell experiments including 3D scaffolds as the proportional dependence of fluorescence and metabolic activity could not be determined.

3.4.2 CELL DIFFERENTIATION

For further investigations on the influence of released ions on osteogenic differentiation, real-time polymerase chain reaction (real-time PCR) was performed. Using this method, replications of a specific DNA sequence are produced and the particular DNA fragment of interest can be detected. Thus, expression levels of important genes during bone formation can be compared and used to determine whether the cells are differentiating toward the osteogenic lineage.[162] First, RNA has to be isolated from the cultured cells and characterized to ensure that each sample has the same amount of RNA at the beginning of the measurement. Real-time PCR multiplies defined regions of complementary DNA (cDNA) that is transcribed from the isolated RNA. The reaction to generate the multiplied DNA sequences is divided in three steps, namely denaturation, annealing and elongation, as shown in Figure 3-14. During denaturation, the sample is heated to approximately 95°C, where hydrogen bonds break and the double-stranded DNA is denatured into single-stranded DNA. Annealing occurs after cooling the temperature down to approximately 60°C. Hydrogen bonds are able to form again, but this time between primers present in the reaction solution and single-strand template molecules. The primers are short single-stranded DNA sequences complementary to the DNA sequence of interest, and therefore, determine the DNA fragment that will be copied several times. After the primers have bonded to the DNA of the target gene and the temperature is increased again, the enzyme DNA polymerase starts to build up replications of the DNA sequence of interest and synthesizes complementary DNA strands. Depending on the primers, the specific region that is to be duplicated can be determined. All three steps are performed in multiple cycles to produce between million and billion molecules of DNA with uniform length, which can be detected reliably.[163] To measure the amount of produced DNA copies in real time, fluorescence such as SYBR Green are used.[164,165] The fluorescence of SYBR Green is measured at the end of every cycle. Because SYBR Green binds to double-stranded DNA molecules, its fluorescence can be used to determine the amount of copied DNA.

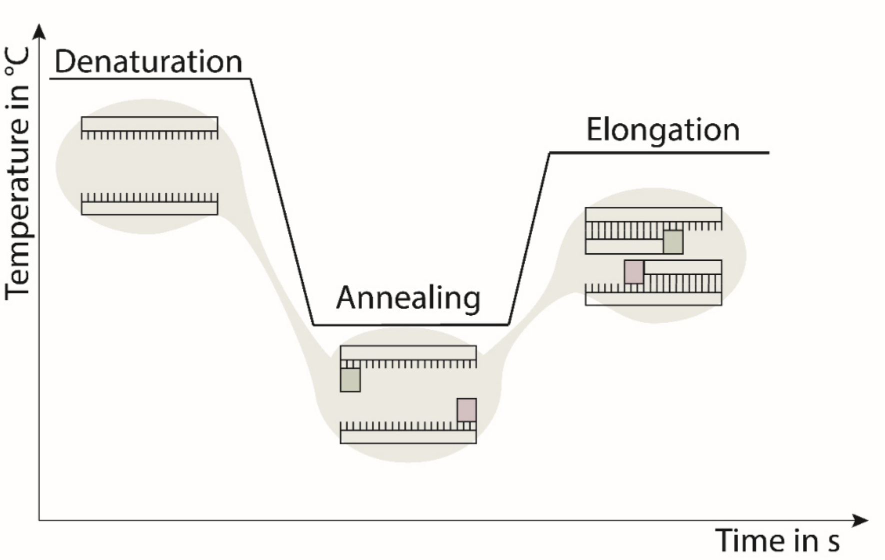

Figure 3-14: Real-time PCR. Hydrogen bonds of double-stranded DNA break during denaturation. The primers bond during annealing and the DNA sequence of interest is replicated. Real-time PCR multiplies between million and billion molecules of a specific DNA sequence of interest, which can be detected.

To calculate specific gene expressions, a normalization strategy that takes into consideration the amount of starting material, amplifications and differences between parallel samples within each sample group is essential. Therefore, the gene expressions are presented as a ratio depending on the expression of glyceraldehyde-3-phosphate dehydrogenase (GAPDH) and β-actin. Both genes are so-called housekeeping genes and are commonly used to normalize PCR results because of their constitutional expression by all cell types [166].

During different phases of bone regeneration, different tissue-specific genes are dominant. As shown in Figure 3-15, gene expression of collagen I is highest within pre-osteoblasts, ALP in mature osteoblasts and BSP within mature osteoblasts and osteocytes.[167,168] Because of the connection between expression level peak and bone formation, these genes could be measured with real-time PCR, for example.

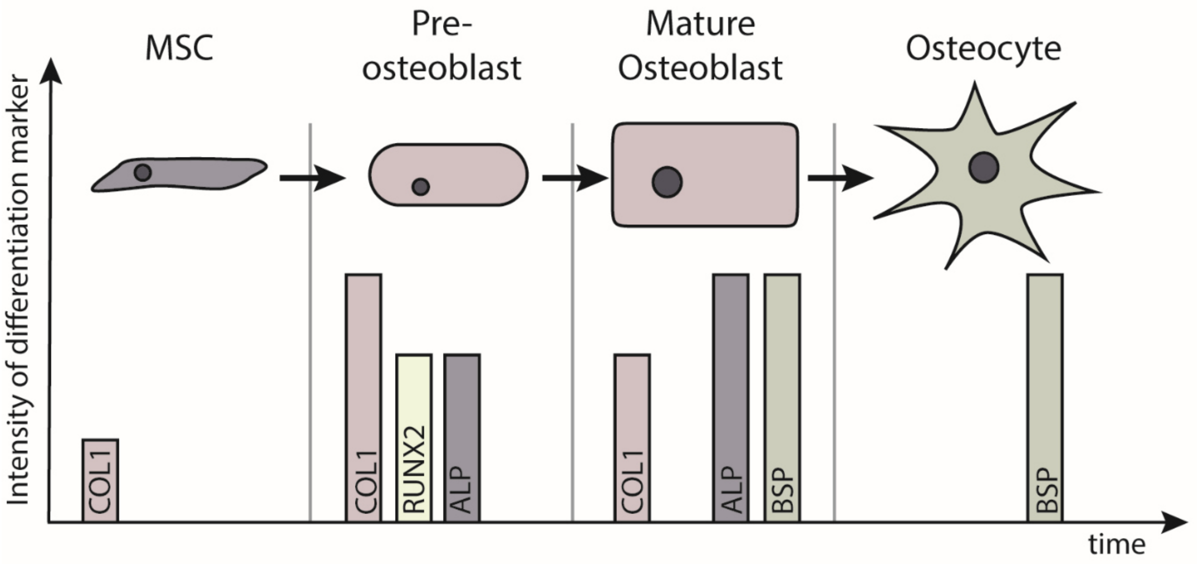

Figure 3-15: Differentiation markers during MSC differentiation to osteocyte. Adapted from Miron and Zhang.[168] COL1 shows the highest intensity in pre-osteoblast. RUNX2 is only present in pre-osteoblast. The highest ALP intensity is in mature osteoblast. BSP is high in mature osteoblast and osteocytes.

Alizarin red staining is another method that can be used to investigate mineral formation in cultured cells, and thereby, the terminal osteogenic differentiation of these cells. Alizarin binds to calcium present in bone. After washing the sample, the bound alizarin red is extracted and the UV/vis absorbance of the dye gives information about the calcium content and bone formation within the sample. Measurements involving staining failed for TiO_2 scaffolds because of their complex 3D structure. The washing process did not remove all of the excess dye. Consequently, remaining dye was present within 3D scaffolds, similar to alamarBlue experiments. Thus, the measured absorbance cannot be used as an indicator for calcium deposition in the cells because the proportional dependency to calcium is not guaranteed with the influence of remaining dye within scaffolds causing large errors.

4 KEY FINDINGS

4.1 CATIONIC DOPING OF TiO_2 SLURRIES (PAPER I)

- 0.1 M NaCl as electrolyte in TiO_2 slurries showed an inert behavior
- 0.1 M KCl and all used 0.1 M divalent salts ($CaCl_2$, $SrCl_2$ and $MgCl_2$) showed a non-inert behavior resulting in an IEP shift. The same non-inert behavior was observed for higher NaCl concentration of 0.2 M
- All doped slurries showed a shear-thinning behavior
- The viscosity of doped slurries was increased depending on the chloride concentration. Thus, 0.2 M NaCl and all divalent doped slurries showed higher viscosity at low shear rates compared to 0.1 M NaCl and KCl slurries

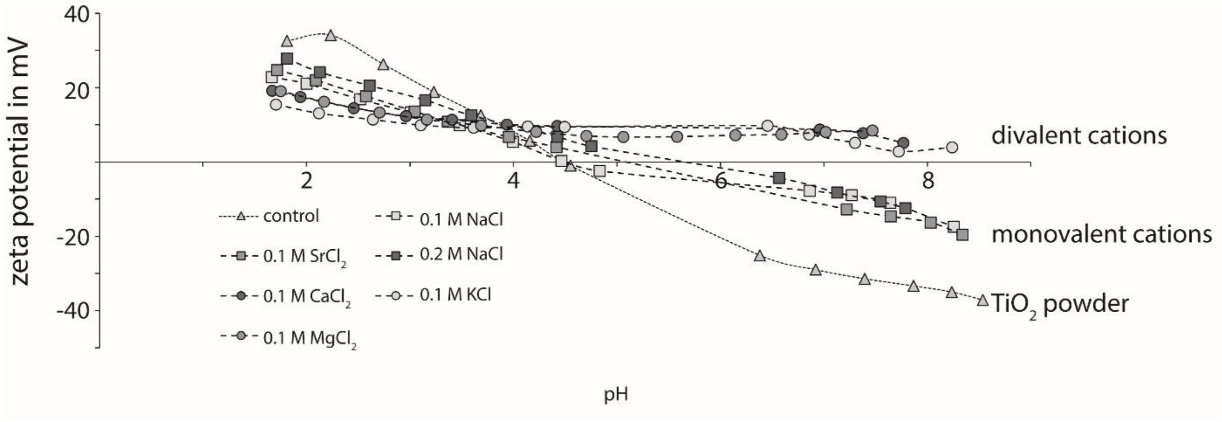

Figure 4-1: Zeta potential as a function of pH for TiO_2 particles dissolved in dH_2O and different electrolyte solutions.

4.2 DOPED TiO_2 SCAFFOLDS (PAPER I-III)

- No significant change in overall pore architecture determined by the foam
- Divalent doping resulted in significant change in strut architecture and increased grain size. Furthermore, the higher densification resulted in an increased compressive strength
- Divalent doping resulted in formation of distinct new grain boundary phases. While grain boundaries in Ca-doped scaffolds exhibited an amorphous grain boundary phase, Sr doping caused the formation of a crystalline phase ($SrTiO_3$) within grain boundaries.
- The effect on grain boundaries and the increase in compressive strength was dependent on doping concentration

4.3 GRAIN BOUNDARY CORROSION IN TiO_2 SCAFFOLDS (PAPER II - III)

- Significant loss of compressive strength in Sr-, Ca- and Mg-doped scaffolds when exposed to acidic environment
- Loss of compressive strength is caused by dissolution of amorphous phases within the grain boundary
- The reduction of impurities during sintering reduced corrosion in Sr-doped scaffolds
- Fast cooling rates affect the grain boundary morphology resulting in further increase of compressive strength
- Corrosion in Ca-doped scaffolds could not be reduced by changing sintering conditions

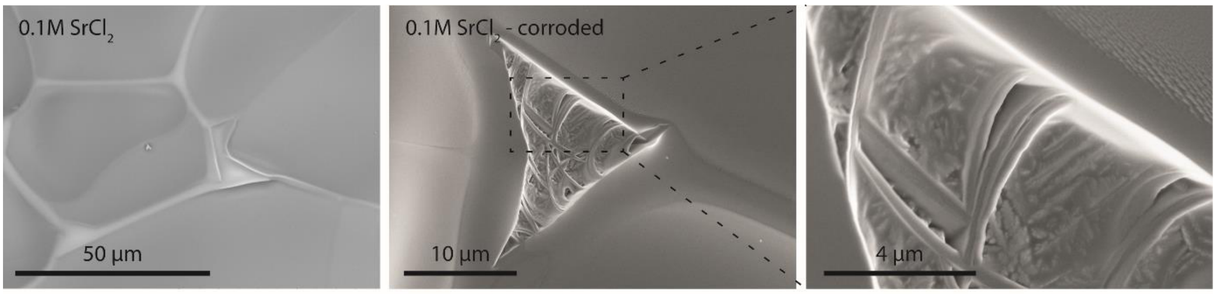

Figure 4-2: Uncorroded and corroded grain boundaries of 0.1 M $SrCl_2$ doped TiO_2 scaffolds

4.4 BIOCOMPATIBILITY OF TiO_2 SCAFFOLDS (PAPER II)

- All doped scaffolds were biocompatible as no cytotoxic effects were observed
- Burst release of Sr and Ca at early time points did not have an effect on osteogenic differentiation
- Continuous release of Mg significantly increased the osteogenic differentiation of hACSs

5 DISCUSSION

Sufficient bone volume is a basic prerequisite to ensure primary implant stability and to improve osteointegration of dental implants. Bone grafts can be used to support bone during regeneration, allow cell ingrowth and vascularization, and thus, ensure a sufficient bone volume.[169,170] The gold standard for bone grafts is autologous grafts.[15] Because of the high risk of infection, especially due to the need of a second surgery, there is a high demand for synthetic bone grafts. Nowadays, ceramics can be used as synthetic bone graft materials.[171] When producing bone scaffolds, the crucial properties to allow regeneration, including vascularization and diffusion of nutrients, are high porosity, interconnected pores and compressive strength similar to natural bone.[22,57-60,172] Several techniques are available to produce ceramic bone grafts, where the replica method is the most common method to produce highly porous materials.[79,80,122,123] When using this method, the suspension properties directly influence the scaffold properties and are therefore of special interest.[80,81,173] To ensure the important shear-thinning behavior of viscous ceramic slurries, additional ions were used in the present study to control interparticle forces in the slurry, and thus, optimize the viscosity of TiO_2 suspensions. To guarantee an efficient support structure during bone regeneration, scaffolds should further exhibit similar compressive strength to natural bone. Previous studies showed either low compressive strength for TiO_2 bone scaffolds or very complex fabrication procedures, such as double coatings, to increase this strength.[69,81,174,175] The main aim for the slurry doping was therefore to simplify the scaffold production. Finally, the scaffolds also have to maintain their properties, especially their compressive strength when implanted to the human body. Thus, the potential corrosive effects of low pH conditions encountered during inflammation in the body were investigated in terms of material dissolution and mechanical integrity of the doped scaffolds. As release of metal cations can cause toxic reaction in the surrounding tissue, the biocompatibility of the scaffolds was verified by culturing cells in contact with the doped TiO_2 scaffolds.

5.1 CATIONIC DOPING OF TiO_2 SLURRIES

The ceramic suspension plays a key role in fabricating ceramic scaffolds using the replica method. Hence, scaffold properties can be directly influenced by the suspension rheology. To get sufficient properties for osteogenesis, such as interconnected pores and high compressive strength, the foam template should be fully covered with the slurry without blocking open pores. Furthermore, the ceramic suspension should exhibit a shear-thinning behavior to ensure a homogenous impregnation of the foam and open pores. Shear-thinning ceramic suspensions are fluid suspensions at high shear rates and allow excess slurry to be removed from the foam template, while their viscous behavior at lower shear rates reduces dripping.[80] Additionally, a stable and controllable process needs a stable suspension without agglomerations of particles. Thus, the optimal slurry properties for scaffold fabrication are well known. However, controlling the stability and rheology of highly concentrated ceramic suspensions still remains a challenge. Because of high attractive forces between TiO_2 particles, represented by a high Hamaker constant, influencing and controlling the repulsive forces in concentrated TiO_2 suspensions is of particular interest.[176] There are several mechanisms for controlling and stabilizing ceramic suspensions. In electrostatic stabilization additional ions adsorb on the particle surfaces and change their electrical double layer, causing repulsive forces between the particles and preventing them from touching each other. Electrosteric stabilization, on the other hand, controls the suspensions stability with added macromolecules, which attach to the particle surfaces creating an adsorbed layer. Even a combination of both is an option.[85,107]

A common method to produce optimal ceramic suspensions for scaffold fabrication via replica method is the use of binders and plasticizers to stabilize the suspension, prevent agglomeration and simultaneously increase the viscosity of the suspension by ensuring shear-thinning behavior.[69,174,175] Poly-D,L-lactic acid (PDLLA), dimethyl carbonate (DMC), polyvinyl alcohol (PVA), ethylene glycol and polysaccharides are common additives present during fabrication of highly concentrated ceramic slurries.[69,118,174,175] The sintered scaffold should be free of the additives because of the high process temperature during sintering and the burn out of polymers at such elevated temperatures. Nevertheless, there is still a risk of remaining impurities in the sintered ceramic, which can influence the surrounding tissue after implantation. Furthermore, the use of plasticizer and binder is a complex interaction between different components, making this strategy very difficult. To avoid the complexity of the optimal ratio between ceramic particles, binder and plasticizer, the present study showed that the use of chloride salts and pH adjustment can be used to optimize slurry properties as well.

Considering the stability of ceramic suspensions, the repulsive forces between particles should be dominant to prevent agglomeration of particles. Thus, the work pH of slurries should be far away from the pH_{IEP} to guarantee a sufficient ζ potential of particles. Tiainen et al. showed that a pH shift to acidic region can result in stable suspensions without any agglomeration.[81] Furthermore, slurries at higher pH values (9-11) showed to be unstable with agglomeration of particles, although the particles were expected to have a high ζ potential similar to the potential at low pH regions. This leads to the assumption that the prevention of agglomeration in highly concentrated ceramic suspensions is dependent on more than simply the ζ potential. To enable the suspension stability without particle agglomeration, a work pH of 1.7 was chosen for the present study. Chloride as anions were chosen to keep the influence of additional ions at low pH constant and comparable to a previous study.[81] To ensure that no toxic ions can be released from the bone scaffolds in situ, the cations of the used chloride salts were selected based on their roles in bone biology.[177-182] While calcium and strontium, for example, has shown positive influence during bone regeneration due to its influence on osteogenic differentiation of MSCs, magnesium has shown to improve osteoblast adhesion to implants and stimulates osteoblastic differentiation of MSCs.[183-189] The main purpose of the used chloride salts was the optimization of slurry properties during fabrication. As shown in Paper II, lower concentration than 0.1 M resulted in an insufficient increase in compressive strength. Higher concentrations (0.2 M) resulted in inhomogeneous grain boundary compositions and even lower compressive strength compared to the undoped scaffolds (see APPENDIX A). Thus, an optimal concentration of 0.1 M was chosen for further optimization (Paper III).

Due to the addition of chloride salts, TiO_2 suspensions could be optimized in viscosity and shear-thinning behavior. To characterize the influence of ions on the ceramic suspension, changes in ζ-potential and pH_{IEP} of TiO_2 particles were investigated in different electrolytes. Depending on the charge of the cation, the electrolytes differed in their counterion ratios (Paper I). The ζ potential of all doped suspensions was shown to decrease due to compression of the electrical double layer. Furthermore, inert and non-inert behavior depending on the used electrolyte, the concentration and the nature of the dissolved particles were investigated. The 1-2 electrolytes showed non-inert behavior, which was confirmed by an IEP shift because of specific bonding between the ions and the particle surface. This is in accordance with other studies investigating the concentration dependency of electrolytes and their inert or non-inert behavior on suspensions and the influence on ζ-potential of TiO_2 particles.[102,104,190,191]

The change in ζ potential in the presence of different electrolytes is well-studied. The transfer of results to highly concentrated suspensions and especially their viscosity is still challenging. As mentioned before, Tiainen et al. recorded that highly concentrated ceramic suspensions are too viscous at high pH values even before adding all the powder, although the ζ potential is expected to be sufficient for dominant repulsive forces.[81] This expands the assumption of another dominant influence than the ζ potential made above. This additional influence is hypothesized to be dependent on hydrogen (H^+) ion concentration, which is high in the acidic pH region. While added chloride ions were shown to decrease the ζ potential of TiO_2 particles, hydrogen ions cause a hydration force, which prevents the formation of agglomeration. Exactly this hydration force is not present at higher pH values. The different suspension stability at high and low pH values shows that the ζ potential of highly concentrated suspensions is just one factor to describe the interparticle forces. This conclusion is supported by measurements of suspension supernatants at higher pH values. Because of a lower hydration force caused by a lower concentration of H^+ ions, the ζ potential is not sufficient to prevent particle agglomeration. Additionally, Davies and Binner have shown, that the addition of salts can lead to coagulation in highly concentrated suspensions, whereby coagulation is defined as network of non-touching particles, which results in higher suspension viscosity.[192] Within the present study, coagulation of particles caused by the addition of ions lead to an increase in viscosity. The combination of the repulsive force between the TiO_2 particles and the hydration force caused by the H^+ ions resulted in highly viscous suspension, which showed the important rheology properties, high viscosity and shear-thinning behavior, needed for scaffold production.

5.2 SINTERING OF TiO_2 SCAFFOLDS

Although stable suspension and ideal rheological behavior are important for scaffold production using the replica method, the suspension stability alone does not govern the physical properties of the produced scaffolds. Several other factors, for example, the influence on ions on TiO_2 sintering behavior and sintering conditions have to be considered when producing ceramic bone scaffolds. After the different ceramic slurries had been analyzed, they were used to fabricate ceramic scaffolds by using the replica method. During sintering, the TiO_2 particles coalesce and densify, lattice defects are eliminated and the scaffold increases in compressive strength [85,107]. The scaffolds characterized in Paper I were sintered at 1500°C for 20 h based on the conditions used in previous studies[81,111], and were considered the standard sintering conditions for TiO_2 scaffolds.

One of the most important scaffold properties is a similar compressive strength to natural bone.[22] Especially for non-resorbable TiO_2 scaffolds, the high porosity is essential to ensure enough space for bone formation within the scaffold pore volume over time. However, increasing the porosity and pore size of a scaffold result in a decrease in its compressive strength as less material is present to sustain the load. Cationic doping was found to increase the compressive strength of the scaffolds while the high porosity remained unaffected (Paper I). A change in strut morphology was found to cause higher compressive strength. The influence of the strut architecture on the compressive strength of ceramic foams has been shown in previous studies.[145,193] A common problem using the replica method is the presence of hollow struts that is caused by the evaporation of the polymer template inside the ceramic coating, resulting in low mechanical strength. In addition to hollow struts, struts exhibiting a characteristic V-shaped morphology also reduces mechanical strength. Thus, a change in compressive strength can be achieved by a change in strut shape.[193,194]

Different strut shapes and changes in compressive strength were observed in monovalent and divalent doped scaffolds. Na- and K-doped scaffolds did not show any change in strut architecture or compressive strength compared to the undoped scaffolds (Paper I). Furthermore, Na- and K-doped scaffolds showed a homogenous distribution of impurity ions in grains and grain boundaries and similar grain size compared to undoped scaffolds. Thus, both monovalent cations did not influence the sintering behavior of TiO_2 and the density of Na- and K-doped TiO_2 was similar compared to the undoped TiO_2. Small cavities within the scaffold struts are still present and cause their low compressive strength. Even with higher Na concentration (0.2 M), no change in grain size was observed. This shows that higher densification of doped TiO_2 cannot be reached by increasing the concentration of Na^+ ions. The increased compressive strength observed for the scaffolds doped with 0.2 M Na is likely to result from the increased slurry viscosity as more TiO_2 slurry is coated on the polymer template[81], resulting in thicker strut walls in comparison to undoped and 0.1 M Na-doped TiO_2 scaffolds (Paper I). This observation is in accordance with previous findings from Davies and Binner showing a higher green density for higher viscosity slurries.[192] In general, no significant improvement in compressive strength was observed when the TiO_2 scaffolds were doped with monovalent cations.

Divalent cations, on the other hand, changed the grain size, strut architecture and compressive strength in comparison to the undoped scaffolds (Paper I-III). A dense strut morphology without any cavity and an increase in compressive strength could be observed for scaffolds doped with divalent cations. This led to the assumption that the divalent cations influence the sintering mechanism and result in improved TiO_2 densification during the heat treatment. Doping of ceramics to change their sintering behavior is a common technique to optimize material or fabrication properties, such as melting temperature. For example, Ca- and Sr-doping has been shown to increase the densification of Y_2O_3, and thus, improves its sinterability.[195] On this basis, cations can be used to decrease the sintering temperature for optimal material densification. Sr-doping of TiO_2, for example, has been shown to decrease the sintering temperature of the material and enable sintering with silver, which is of special interest for the fabrication of components for electronic applications.[196] Similar to the present study, the additional ions caused liquid phase sintering in which more rapid grain boundary diffusion kinetics and high grain boundary mobility are present. Consequently, the grain size of TiO_2 crystals was increased. Due to faster grain growth, the strut morphology was dense and no cavity was observed.

While the present study showed a simple strategy to improve the compressive strength of TiO_2 scaffolds by cationic doping, several studies have used complex recoating strategies to improvement the compressive strength of highly porous bone scaffolds.[145,175] Novak et al. showed that hollow spaces in the struts could be filled by an additional polymer coating, and thus, the compressive strength could be increased. This is a common method to improve the strength of scaffolds. While polymers are often used for recoatings, Tiainen et al. used a second low viscous ceramic suspension for recoating and filling cracks along the struts.[81,145] Nonetheless, recoating increases the complexity and time of the scaffold production. Ceramic double coatings especially require a sintering procedure, which doubles the time of heat treatment of ceramic scaffolds. Additionally, there is a risk that recoating can decrease the porosity of the fabricated scaffolds.[175] However, thinking of bone tissue engineering applications, the bone ingrowth and vascularization requires a high porosity.[197] Thus, the reduction in porosity is not a promising strategy to improve compressive strength. Overall, the doping of ceramic suspension caused a change in strut architecture, which further caused an increase in compressive strength. The suspension doping enables a stable and easy way to manipulate and improve the scaffold production. The elimination of additional coatings minimize the failure in improving the compressive strength caused by an inhomogeneous coating.

Grain boundaries have an important influence on mechanical properties. Thus, besides the investigation of strut morphology, the grain boundary formation of doped TiO_2 scaffolds is of special interest when investigating the compressive strength. Si and Al originating from the sintering environment, especially from the heating rods (SiC) and oven insulation (Al_2SiO_5) were observed in grain boundaries of all fabricated scaffolds. While homogenous distribution of Na^+ and K^+ was observed in the scaffolds doped with monovalent cations, divalent cations Ca^{2+} and Sr^{2+} were found to segregate to the grain boundaries during sintering. The observed grain boundary segregation depending on the specific ions was in agreement with previous studies.[196,198-201] Yan et al. observed Sr segregation to grain boundaries as well in context of Sr-doped TiO_2 for the fabrication of components for electronic application.[202] The present study showed amorphous grain boundaries in Ca-doped scaffolds and the formation of a crystalline phase was found in Sr-doped scaffolds. Thus, the crystal $SrTiO_3$ was observed within grain boundaries (Paper II). Santhosh et al. have shown that the addition of Nb_2O_5, $SrCO_3$ and Bi_2O_3 in TiO_2 result in the formation of strontium titanate after sintering. While the used ratio of 100:0.25:1:1 (TiO_2 : Nb_2O_3 : $SrCO_3$: Bi_2O_3) were dry mixed and sintered at temperatures between 1100 to 1350°C, the formation of strontium titanate was observed as secondary phase in 1100°C samples.[203] However, the doped TiO_2 scaffolds that were sintered using the standard sintering parameters did not match the crucial scaffold properties in terms of high compressive strength. The scaffolds showed compressive strength below the minimum strength of cancellous bone. Therefore, the influence of sintering parameters on strut morphology, grain boundary composition and the resulting compressive strength were investigated in Paper III.

Densification of ceramics is influenced by sintering parameters such as heating rate, sintering temperature, holding time and cooling rate.[107,110] Different diffusion mechanism can be affected by changing the sintering temperature or heating rate, resulting in different grain size and degree of densification.[204-206] Especially for three dimensional complex structures such as the produced scaffolds, increased densification of the material by increasing the sintering time can cause dense strut architectures which result in higher compressive strength.[145] Furthermore, changing the cooling rate was shown to influence the grain boundary composition of undoped TiO_2 scaffolds.[111] The effects of dopants on sintering mechanism are very complex and factors such as segregation at the grain boundaries, influence on surface and grain boundary energies and the formation of a second phase can be influenced simultaneously.[110] The general influence of sintering parameters on TiO_2 sintering mechanism and additionally the influence of different dopants on these mechanisms were investigated in Paper III. To investigate the influence of individual sintering parameters, just one parameter was changed at a time. The best results, defined by the highest compressive strength, were then chosen for further process changes. Due to a fixed order of changes, cross-influences of sintering parameters on densification cannot be detected. Nevertheless, a general overview of different influences caused by change in sintering parameters on TiO_2 scaffolds was possible. While strut morphology was similar after changing the sintering parameters, changes in sintering parameters caused different compressive strength and thus changes within the grain boundaries.

The formation of $SrTiO_3$ was observed in the grain boundaries (Paper II). Furthermore, the compressive strength of the scaffold could be increased by controlling the sintering conditions, indicating that the strength is influenced by the $SrTiO_3$ crystal growth within TiO_2 grain boundaries (Paper III). Whereas the heating parameters did not show any significant changes in the compressive strength of Sr-doped TiO_2 scaffolds, the cooling rate affected the strength significantly. The crystal growth is mainly influenced by the cooling rate. Consequently, faster cooling rates lead to smaller $SrTiO_3$ crystals within the grain boundaries, which caused the higher compressive strength of the fabricated scaffolds. Thus, controlling the crystal growth can be used to increase the compressive strength of Sr-doped scaffolds. The importance of grain boundaries on the compressive strength can be demonstrated by comparing the scaffold strength between air quenched (AQ) scaffolds and scaffolds cooled with 2 K/min. While both scaffolds demonstrate dense struts, different crystal formation was observed at the doped grain boundaries. Fast cooling rate led to a higher amount of small crystals at the grain boundaries and higher compressive strength compared to standard sintered Sr-doped scaffolds (Paper III). In contrast, the scaffolds produced with slow cooling rate of 2 K/min showed very large $SrTiO_3$ crystals at the grain boundaries (Appendix B) and the mechanical strength of the scaffolds was too low to be detected by the used instrument. This proves the importance of the grain boundary composition on the compressive strength of the doped scaffolds.

The Mg-doped scaffolds showed similar changes in their compressive strength caused by changing sintering parameters as Sr-doped scaffolds. While heating rate, heating temperature and holding time did not show any effect on compressive strength, an increase in cooling rate led to a significant increase in compressive strength. Although not proven by electron diffraction, the SEM images (Appendix C) and the similar compressive strength pattern depending on the sintering conditions led to the assumption that crystalline $MgTiO_3$ forms in grain boundaries. The formation of $MgTiO_3$ has been observed in MgO-TiO_2 systems, for a magnesium content of 10 wt% and 50 wt%.[207,208] While such high amounts of magnesium were not added into the slurry in the present study, high local Mg^{2+} concentrations can exist in some areas within the grain boundary. Although no dominant grain boundary segregation was observed in Mg-doped scaffolds, Mg-rich spots within the grain boundaries were observed. Furthermore, the significant release of Mg ions over 7 days during the corrosion test indicates that magnesium is bound to a crystalline structure rather than being instantly released from an amorphous grain boundary phase (Paper II).

5.3 HIGH COMPRESSIVE STRENGTH AFTER EXPOSURE TO ACIDIC ENVIRONMENT

However, the increase in compressive strength by cationic doping of TiO_2 slurries is just one important parameter considering bone scaffolds. The improved scaffold properties, particularly the compressive strength, should be maintained during bone regeneration. During the early inflammatory phase of bone regeneration, osteoclasts and macrophages are secreting HCl to resorb bone tissue and a local pH drop to values of pH 3.6-3.7 occurs.[114] Ceramics exposed to such acidic environment can undergo corrosion. H^+ ions are the main trigger for dissolution of grain boundaries resulting in a dramatic loss in compressive strength.[115,209] Furthermore, dramatic and sudden loss of mechanical support provided by the bone scaffold may lead to unsuccessful bone healing. While undoped scaffolds and scaffolds doped with monovalent cations did not show any visible signs of corrosion or loss in compressive strength after 8 weeks in acidic environment, scaffolds doped with divalent cations showed a significant loss in strength already after 4 h exposure to acidic environment (APPENDIX D, Paper II and III). Thus, impurity segregation in divalent scaffolds was shown to change the grain boundary composition and cause grain boundary corrosion. Although the grain boundary corrosion is an obvious drawback of the cationic doping, the additional ions were found necessary to significantly increase the compressive strength of the fabricated scaffolds. Thus, the grain boundary compositions needed to be optimized in order to find the best compromise between compressive strength and corrosion resistant.

Sr- and Mg-doped scaffolds doped with more than 0.06 M and Ca-doped scaffolds with 0.1 M divalent cations in the slurry developed a distinct dopant-rich grain boundary phase and showed reduction in compressive strength when exposed to 1 mM HCl irrespective of the used salt concentration (Paper II). However, corroded grain boundaries showed visible differences between Ca-doped scaffolds, which exhibited amorphous grain boundaries, and Sr-doped scaffolds, which exhibited crystalline grain boundaries. Amorphous grain boundaries showed homogenous distribution of all detected impurities (Al, Si and Ca). Increasing salt content in the slurry led to more dominant grain boundaries, but up to a concentration of 0.08 M $CaCl_2$ the corrosion seemed to be homogenous throughout the grain boundary phase and no significant change in compressive strength was observed after 7 days. As the $CaCl_2$ concentration was increased to 0.1 M, formation of TiO_2 lamellae within the grain boundaries was observed. This lamella formation caused inhomogeneous grain boundary corrosion and a significant loss in compressive strength (Paper II). By changing the sintering conditions of these scaffolds to higher sintering temperatures and longer sintering times, higher densification was obtained, which in turn resulted in higher compressive strength. However, the grain boundary composition seemed to remain similar as significant loss in compressive strength due to corrosion was still observed. For all 0.1 M Ca-doped scaffolds sintered at different conditions, dissolution of the amorphous grain boundary phase resulted in a significant loss in compressive strength.

In contrast to corrosion in amorphous grain boundary phases, a crystalline phase within grain boundaries was shown to affect the corrosion behavior of Sr-doped scaffold. On the one hand, increasing the $SrCl_2$ concentration during scaffold fabrication caused an increase in crystal formation, corrosion and loss of compressive strength (Paper II). On the other hand, increasing the sintering time and cooling rate of Sr-doped scaffolds produced with slurries containing 0.1 M $SrCl_2$ resulted in even higher compressive strengths, which were maintained even after corrosion (Paper III). Further investigations showed that the crystal formation was different for differently treated scaffolds. While the $SrTiO_3$ crystals showed corrosion resistance, dissolution of the amorphous phase within the grain boundaries was still present. Thus, the present study shows that corrosion in doped TiO_2 scaffolds is always present concentrated in amorphous region within the grain boundaries.

To influence the impurity segregation to grain boundaries, and thereby, the corrosion behavior of scaffolds exposed to acidic environment, the sintering parameters were changed. Especially rapid cooling rates have been described to influence impurity segregation.[210] This has also shown for undoped TiO_2 scaffolds as decreased amount of impurities was detected within the grain boundaries following an air quenching process, where the scaffolds are cooled as fast as possible to room temperature.[111] In contrast, the same study showed increased grain boundary corrosion for the air quenched scaffolds in acidic environments. Thus, the prevention of corrosion is not successful by simply reducing the grain boundary impurities. Within the present study, different ovens were used for different heat treatments. For a higher sintering temperature of 1600°C, an oven with an Al_2SiO_5 isolation of SiC heating rods decreased the amount of impurities in the grain boundaries. However, scaffolds sintered in an oven with isolated heating rods, and thus, a decreased amount of impurities still showed highly corroded amorphous grain boundaries and a significant loss in compressive strength (Paper III). In accordance, the arrangement of grain boundaries and the movement of impurities towards free surface of particles has been described to cause more efficient Si dissolution.[211] Consequently, prevention of dissolution of silica-rich amorphous grain boundaries is neither successful by changing the heat treatment nor the sintering impurities present during fabrication.

As shown in Paper II, the formation of $SrTiO_3$ increases as the Sr content in the slurry is increased, and simultaneously, the grain boundary corrosion increases as well. Thus, the improvement in compressive strength correlates with increased corrosion. The decrease in the amount of Sr ions did not result in sufficient compressive strength for the use as bone grafts. Nevertheless, sintering of Sr-doped scaffolds in an impurity reduced environment already resulted in corrosion resistant scaffolds and the compressive strength was maintained after exposure to acidic environment (Paper III). The different corrosion behavior of Ca- and Sr-doped scaffolds sintered in different ovens demonstrates the importance of the $SrTiO_3$ crystal itself. However, corrosion and the loss in compressive strength was observed for Sr-doped scaffolds sintered in impurity-rich environments (Paper III). Thus, the simple formation of $SrTiO_3$ within grain boundaries do not prevent of dramatic loss in compressive strength of doped scaffolds. The properties of the $SrTiO_3$ crystal itself has to be important to get a strong crystal within grain boundaries, which is maintained after corrosion of the amorphous phase and sustain the compressive strength of scaffolds. This leads to the assumption, that a reduction of impurities during sintering can cause higher densification of $SrTiO_3$ crystal formation. Thus, $SrTiO_3$ crystal properties can be influenced by the sintering conditions. This specific strong $SrTiO_3$ crystal, sintered in impurity reduced sintering environment, is a support structure between TiO_2 grains which maintain the strength after corrosion while dissolution of the amorphous phase was present in between the $SrTiO_3$ crystals. Further increase in compressive strength of Sr-doped scaffolds could be observed for higher sintering temperatures and faster cooling rates. This could be explained by an improvement of $SrTiO_3$ properties caused by higher sintering temperatures and faster cooling rates as well. In conclusion, a high compressive strength and corrosion resistance in Sr-doped TiO_2 bone scaffolds was reached by combining the optimal sintering environment and sintering conditions. While reducing impurities in the sintering was shown to mainly affect the corrosion resistance, the heating parameters influenced the growth of $SrTiO_3$ crystals within the grain boundaries and thus the compressive strength.

The importance of corrosion resistant scaffolds is of special interest during the early inflammatory phase of bone healing. Macrophases and osteoclasts secrete HCl, which can cause dissolution in the grain boundary. As shown in Papers II and III, a decrease in pH caused a significant reduction in compressive strength. Furthermore, this dramatic loss of compressive strength already occurred after 4 h exposure to acidic environment. Although the optimized Sr-doped scaffolds maintained their compressive strength for over 8 weeks when exposed to acidic environment (pH 3), the question is, for how long the scaffolds should exhibit high compressive strength to support bone regeneration. In vivo studies have shown, that the compressive strength of implanted bone grafts strongly correlates with bone ingrowth.[212,213] Already after three weeks, a significant ingrowth of bone, and therefore, a significant increase in compressive strength could be observed. Further increase in bone graft strength was observed after longer implantation times (6 and 9 weeks).[214,215] Consequently, the fabricated scaffolds with a high compressive strength for 8 weeks can be assumed to successfully support bone regeneration during the first weeks of healing. If the loss in compressive strength of the ceramic material occurred at a later time point, the increase in strength caused by bone ingrowth is expected to guarantee sufficient strength during bone healing. However, further investigations are necessary to validate these assumptions.

5.4 BIOCOMPATIBILITY OF PRODUCED SCAFFOLDS

The biocompatibility of the produced scaffolds may be different compared to the undoped scaffolds. A previous study has shown that cell growth towards a differentiated state can be sustained by the undoped TiO_2 scaffolds in vitro.[157] Cells cultured on these scaffolds also showed significantly higher cell viability and cell proliferation in comparison to a number of commercially available bone graft materials.[120] Furthermore, a similar osseointegration compared to autologous bone blocks, the evidence of vascularization and formation of bone lamellae within the inner regions of the scaffold has been confirmed in vivo.[117,119] Thus, the fabricated undoped TiO_2 scaffolds are convincing bone grafts because of the pore interconnection and the important relative orientations of pore channels.[216,217] As confirmed in Paper I, the microstructure of fabricated scaffolds did not change significantly. Thus, the doped scaffolds also exhibit the important scaffold properties such as pore size, porosity and the interconnections between pores.

The release of ions from the material can influence the surrounding cells and the bone regeneration process. As shown in Paper II, the corrosion of scaffolds doped with divalent cations lead to a release of the different dopant ions, which in theory could transform the used biocompatible ceramic into a toxic material. Therefore, scaffolds with the highest corrosion, and consequently, the highest amount of released ions were chosen for the cell experiments. This high amount of released ions simulates the worst case as lower ion concentrations are assumed to be tolerated by surrounding tissue if no toxicity is observed for the highest released concentration. It is not known whether the concentration of the released ions depends on the location. To mimic in vivo conditions, cells were therefore seeded directly on the doped scaffolds and were growing on and into the scaffolds. As shown in Paper II, there was no cytotoxic effect on cells caused by released ions. Rather the opposite was observed for cells seeded on Mg-doped scaffolds which showed increased osteogenic differentiation.

6 CONCLUSIONS AND RESEARCH PROSPECTS

The combination of corrosion resistance and high compressive strength is mandatory for ceramic TiO_2 scaffolds. A similar compressive strength as natural bone ensures a support structure during bone regeneration and corrosion resistance ensures the stability of this support structure during the inflammatory phase of bone healing. Several studies have focused on improving the compressive strength by different coatings.[69,81,174,175] However, these strategies are complex and time-consuming processes, especially when a mass production of promising ceramic scaffolds is considered.

The present study introduced a novel way of suspension doping which enables a simple, fast and stable method to fabricate TiO_2 scaffolds with high reproducibility. Due to the addition of ions in highly concentrated ceramic suspensions, the viscosity and shear-thinning effect were optimized concerning the necessary requirements using the replica method. The doped scaffolds showed thicker and dense struts and a significant increase in compressive strength. However, high dopant concentrations that resulted in higher compressive strength also increased corrosion in the grain boundaries. Hence, the formation of the crystalline phase present in Sr-doped scaffolds was adjusted. High sintering temperatures and fast cooling rates led to the formation of a strong $SrTiO_3$ network within the grain boundaries. While the amorphous phase in between this crystalline structure still showed dissolution in acidic environment, $SrTiO_3$ crystals stabilized the compressive strength.

All in all, doping of ceramic suspensions and optimizing the sintering conditions resulted in significantly increased compressive strength, corrosion resistance, and thus, stable strength over 4 weeks when exposed to acidic environment. Additionally, important scaffold properties, such as sufficient specific pore size, porosity and interconnected pores were kept the same as for undoped scaffolds.

However, although the compressive strength showed to be stable, dissolution of the amorphous phase within grain boundaries was still present in the doped TiO_2 scaffolds. The release of Mg from Mg-doped TiO_2 grain boundaries showed a significant increase in osteogenic differentiation of hASCs in vitro. Consequently, a further optimization of doped scaffolds could be a controlled release of ions to improve osteogenesis. Current studies have shown that a controlled drug release of coatings can cause antibacterial effects[218]. Considering future application, the controlled release of ions could be used to develop bioactive bone scaffolds. The positive influence of Sr^{2+} on bone cells is well known.[187,219,220] The amount of released Sr^{2+}

was shown to be too low for significant changes in osteogenic differentiation (Paper II). Further optimizations of Sr-doping and scaffold production could result in the combination of corrosion resistant scaffolds high in compressive strength with bioactive potential.

7 REFERENCES

1. Romeo, E., et al., *Long-term survival and success of oral implants in the treatment of full and partial arches: a 7-year prospective study with the ITI dental implant system.* International Journal of Oral & Maxillofacial Implants, 2004. **19**(2).
2. Lombardo, G., et al., *Cumulative success rate of short and ultrashort implants supporting single crowns in the posterior maxilla: A 3-year retrospective study.* International journal of dentistry, 2017. **2017**.
3. Verma, S., S.K. Srivastava, and A. Khemka, *Success rate of dental implants in medically compromised patients: A retrospective study.* Journal of Advanced Medical and Dental Sciences Research, 2019. **7**(12).
4. Papaspyridakos, P., et al., *Success criteria in implant dentistry: a systematic review.* Journal of dental research, 2012. **91**(3): p. 242-248.
5. Ekfeldt, A., et al., *A retrospective analysis of factors associated with multiple implant failures in maxillae.* Clinical Oral Implants Research, 2001. **12**(5): p. 462-467.
6. Turkyilmaz, I. and E.A. McGlumphy, *Influence of bone density on implant stability parameters and implant success: a retrospective clinical study.* BMC Oral Health, 2008. **8**(1): p. 32.
7. Levin, L., D. Nitzan, and D. Schwartz-Arad, *Success of dental implants placed in intraoral block bone grafts.* Journal of periodontology, 2007. **78**(1): p. 18-21.
8. Schwartz-Arad, D., L. Levin, and L. Sigal, *Surgical success of intraoral autogenous block onlay bone grafting for alveolar ridge augmentation.* Implant dentistry, 2005. **14**(2): p. 131-138.
9. Proussaefs, P., et al., *The use of titanium mesh in conjunction with autogenous bone graft and inorganic bovine bone mineral (bio-oss) for localized alveolar ridge augmentation: a human study.* International Journal of Periodontics & Restorative Dentistry, 2003. **23**(2).
10. Donos, N., N. Mardas, and V. Chadha, *Clinical outcomes of implants following lateral bone augmentation: systematic assessment of available options (barrier membranes, bone grafts, split osteotomy).* Journal of clinical periodontology, 2008. **35**: p. 173-202.
11. Pape, H.C., A. Evans, and P. Kobbe, *Autologous bone graft: properties and techniques.* Journal of orthopaedic trauma, 2010. **24**: p. S36-S40.
12. Wang, W. and K.W.K. Yeung, *Bone grafts and biomaterials substitutes for bone defect repair: A review.* Bioactive Materials, 2017. **2**(4): p. 224-247.
13. Laurencin, C., Y. Khan, and S.F. El-Amin, *Bone graft substitutes.* Expert Review of Medical Devices, 2006. **3**(1): p. 49-57.
14. Shibuya, N. and D.C. Jupiter, *Bone Graft Substitute: Allograft and Xenograft.* Clinics in Podiatric Medicine and Surgery, 2015. **32**(1): p. 21-34.
15. Zimmermann, G. and A. Moghaddam, *Allograft bone matrix versus synthetic bone graft substitutes.* Injury, 2011. **42**: p. S16-S21.
16. Velnar, T., et al., *Biomaterials and host versus graft response: a short review.* Bosnian journal of basic medical sciences, 2016. **16**(2): p. 82.
17. Younger, E.M. and M.W. Chapman, *Morbidity at bone graft donor sites.* Journal of Orthopaedic Trauma, 1989. **3**(3): p. 192-195.
18. Nandi, S., et al., *Orthopaedic applications of bone graft & graft substitutes: a review.* Indian Journal of Medical Reseach, 2010. **132**(1): p. 15-30.
19. Buck, B., T.I. Malinin, and M.D. Brown, *Bone transplantation and human immunodeficiency virus. An estimate of risk of acquired immunodeficiency syndrome (AIDS).* Clinical orthopaedics and related research, 1989(240): p. 129-136.
20. Stevenson, S., *Biology of bone grafts.* Orthopedic Clinics, 1999. **30**(4): p. 543-552.

21. Oryan, A., et al., *Bone regenerative medicine: classic options, novel strategies, and future directions.* Journal of orthopaedic surgery and research, 2014. **9**(1): p. 18.
22. Goldberg, V.M. and S. Akhavan, *Biology of Bone Grafts*, in *Bone Regeneration and Repair*. 2005, Springer. p. 57-65.
23. Damien, C.J. and J.R. Parsons, *Bone graft and bone graft substitutes: a review of current technology and applications.* Journal of Applied Biomaterials, 1991. **2**(3): p. 187-208.
24. Oryan, A., S. Monazzah, and A. Bigham-Sadegh, *Bone injury and fracture healing biology.* Biomedical and environmental sciences, 2015. **28**(1): p. 57-71.
25. Morgan, E.F., G.L. Barnes, and T.A. Einhorn, *The bone organ system: form and function*, in *Osteoporosis*. 2013, Elsevier. p. 3-20.
26. Ralston, S.H., *Bone structure and metabolism.* Medicine, 2013. **41**(10): p. 581-585.
27. Mountziaris, P.M. and A.G. Mikos, *Modulation of the inflammatory response for enhanced bone tissue regeneration.* Tissue Engineering Part B: Reviews, 2008. **14**(2): p. 179-186.
28. Tariverdian, T., et al., *10 - Scaffold for BoneTtissue Engineering*, in *Handbook of Tissue Engineering Scaffolds: Volume One*, M. Mozafari, F. Sefat, and A. Atala, Editors. 2019, Woodhead Publishing. p. 189-209.
29. Burn, E.D., *Promoting healing of bone tissue.* AORN Journal, 1982. **35**(6): p. 1186-1191.
30. Marsell, R. and T.A. Einhorn, *The biology of fracture healing.* Injury, 2011. **42**(6): p. 551-555.
31. Sfeir, C., et al., *Fracture Repair*, in *Bone Regeneration and Repair*. 2005, Springer. p. 21-44.
32. Metzger, C.E. and S.A. Narayanan, *The Role of Osteocytes in Inflammatory Bone Loss.* Frontiers in Endocrinology, 2019. **10**(285).
33. Tsiridis, E., N. Upadhyay, and P. Giannoudis, *Molecular aspects of fracture healing: which are the important molecules?* Injury, 2007. **38**(1): p. S11-S25.
34. Gerstenfeld, L.C., et al., *Three-dimensional reconstruction of fracture callus morphogenesis.* Journal of Histochemistry & Cytochemistry, 2006. **54**(11): p. 1215-1228.
35. Long, M.W., et al., *Regulation of human bone marrow-derived osteoprogenitor cells by osteogenic growth factors.* The Journal of clinical investigation, 1995. **95**(2): p. 881-887.
36. Keramaris, N., et al., *Fracture vascularity and bone healing: a systematic review of the role of VEGF.* Injury, 2008. **39**: p. S45-S57.
37. Mansour, A., et al., *Alveolar bone grafting: Rationale and clinical applications*, in *Dental Implants and Bone Grafts*. 2020, Elsevier. p. 43-87.
38. Rocchietta, I., F. Fontana, and M. Simion, *Clinical outcomes of vertical bone augmentation to enable dental implant placement: a systematic review.* Journal of clinical periodontology, 2008. **35**: p. 203-215.
39. Hoornaert, A. and P. Layrolle, *Bone Regenerative Issues related to Bone Grafting Biomaterials*, in *Dental Implants and Bone Grafts*. 2020, Elsevier. p. 207-215.
40. Hämmerle, C.H. and R.E. Jung, *Bone augmentation by means of barrier membranes.* Periodontology 2000, 2003. **33**(1): p. 36-53.
41. Wang, H.-L. and L. Boyapati, *"PASS" principles for predictable bone regeneration.* Implant dentistry, 2006. **15**(1): p. 8-17.
42. Linde, A., et al., *Osteopromotion: a soft-tissue exclusion principle using a membrane for bone healing and bone neogenesis.* Journal of periodontology, 1993. **64**: p. 1116-1128.

43. Ramalingam, S., et al., *Alveolar Bone Science: Structural Characteristics and Pathological Changes*, in *Dental Implants and Bone Grafts*. 2020, Elsevier. p. 1-22.
44. Intini, G., et al., *Alveolar bone loss: mechanisms, potential therapeutic targets, and interventions.* Advances in dental research, 2014. **26**(1): p. 38-46.
45. Retzepi, M. and N. Donos, *Guided bone regeneration: biological principle and therapeutic applications.* Clinical oral implants research, 2010. **21**(6): p. 567-576.
46. Khan, S.N., et al., *The biology of bone grafting.* JAAOS-Journal of the American Academy of Orthopaedic Surgeons, 2005. **13**(1): p. 77-86.
47. Schroeder, J.E. and R. Mosheiff, *Tissue engineering approaches for bone repair: concepts and evidence.* Injury, 2011. **42**(6): p. 609-613.
48. Sutherland, D. and M. Bostrom, *Grafts and Bone Graft Substitutes*, in *Bone Regeneration and Repair*. 2005, Springer. p. 133-156.
49. Mauffrey, C., et al., *Bone graft substitutes for articular support and metaphyseal comminution: what are the options?* Injury, 2011. **42**: p. S35-S39.
50. Lichte, P., et al., *Scaffolds for bone healing: concepts, materials and evidence.* Injury, 2011. **42**(6): p. 569-573.
51. De Long, W., et al., *Bone grafts and bone graft substitutes in orthopaedic trauma surgery.* The Journal of Bone & Joint Surgery, 2007. **89**(3): p. 649-658.
52. Joneschild, E. and J.R. Urbaniak, *Biology of the vascularized fibular graft*, in *Bone Regeneration and Repair*. 2005, Springer. p. 93-112.
53. Finkemeier, C.G., *Bone-grafting and bone-graft substitutes.* JBJS, 2002. **84**(3): p. 454-464.
54. Herford, A.S., E. Stoffella, and C.M. Stanford, *Bone Grafts and Bone Substitute Materials*, in *Principles and Practice of Single Implant and Restorations*. 2014, Elsevier. p. 75-86.
55. Guo, J.L., T.C. Piepergerdes, and A.G. Mikos, *Chapter 6 - Bone graft engineering: Composite scaffolds*, in *Dental Implants and Bone Grafts*, H. Alghamdi and J. Jansen, Editors. 2020, Woodhead Publishing. p. 159-181.
56. Moore, W.R., S.E. Graves, and G.I. Bain, *Synthetic bone graft substitutes.* ANZ journal of surgery, 2001. **71**(6): p. 354-361.
57. Davy, D.T., *Biomechanical issues in bone transplantation.* Orthopedic Clinics, 1999. **30**(4): p. 553-563.
58. Goldberg, V.M., *Selection of bone grafts for revision total hip arthroplasty.* Clinical Orthopaedics and Related Research (1976-2007), 2000. **381**: p. 68-76.
59. Carter, D.R. and W.C. Hayes, *Bone compressive strength: the influence of density and strain rate.* Science, 1976. **194**(4270): p. 1174-1176.
60. Leteve, M. and N. Passuti, *Current Concepts in Bone Graft Substitutes.* New Journal of Glass and Ceramics, 2018. **08**: p. 39-54.
61. Calori, G., et al., *The use of bone-graft substitutes in large bone defects: any specific needs?* Injury, 2011. **42**: p. S56-S63.
62. Bohner, M., *Calcium orthophosphates in medicine: from ceramics to calcium phosphate cements.* Injury, 2000. **31**: p. D37-D47.
63. Holzapfel, B.M., et al., *How smart do biomaterials need to be? A translational science and clinical point of view.* Advanced drug delivery reviews, 2013. **65**(4): p. 581-603.
64. Murshed, M., et al., *Unique coexpression in osteoblasts of broadly expressed genes accounts for the spatial restriction of ECM mineralization to bone.* Genes & development, 2005. **19**(9): p. 1093-1104.
65. Radin, S., et al., *In vivo tissue response to resorbable silica xerogels as controlled-release materials.* Biomaterials, 2005. **26**(9): p. 1043-1052.

66. Fleming, J.E., C.N. Cornell, and G.F. Muschler, *Bone cells and matrices in orthopedic tissue engineering.* Orthopedic Clinics, 2000. **31**(3): p. 357-374.
67. Fernandez de Grado, G., et al., *Bone substitutes: a review of their characteristics, clinical use, and perspectives for large bone defects management.* Journal of tissue engineering, 2018. **9**: p. 2041731418776819.
68. Campana, V., et al., *Bone substitutes in orthopaedic surgery: from basic science to clinical practice.* Journal of Materials Science: Materials in Medicine, 2014. **25**(10): p. 2445-2461.
69. Novak, S., et al., *TiO_2 foams with poly-(d, l-lactic acid)(PDLLA) and PDLLA/Bioglass® coatings for bone tissue engineering scaffolds.* Journal of materials science, 2009. **44**(6): p. 1442-1448.
70. Vallet-Regí, M., *Evolution of bioceramics within the field of biomaterials.* Comptes Rendus Chimie, 2010. **13**(1-2): p. 174-185.
71. Tengvall, P. and I. Lundström, *Physico-chemical considerations of titanium as a biomaterial.* Clinical materials, 1992. **9**(2): p. 115-134.
72. Ellingsen, J.E., *A study on the mechanism of protein adsorption to TiO_2.* Biomaterials, 1991. **12**(6): p. 593-596.
73. Lindberg, F., et al., *Hydroxylapatite growth on single-crystal rutile substrates.* Biomaterials, 2008. **29**(23): p. 3317-3323.
74. Forsgren, J., et al., *Formation and adhesion of biomimetic hydroxyapatite deposited on titanium substrates.* Acta Biomaterialia, 2007. **3**(6): p. 980-984.
75. Svetina, M., et al., *Deposition of calcium ions on rutile (110): a first-principles investigation.* Acta Materialia, 2001. **49**(12): p. 2169-2177.
76. Nygren, H., P. Tengvall, and I. Lundström, *The initial reactions of TiO_2 with blood.* Journal of Biomedical Materials Research: An Official Journal of The Society for Biomaterials and The Japanese Society for Biomaterials, 1997. **34**(4): p. 487-492.
77. Tsukimura, N., et al., *The effect of superficial chemistry of titanium on osteoblastic function.* Journal of Biomedical Materials Research Part A: An Official Journal of The Society for Biomaterials, The Japanese Society for Biomaterials, and The Australian Society for Biomaterials and the Korean Society for Biomaterials, 2008. **84**(1): p. 108-116.
78. Jones, J.R. and L.L. Hench, *Regeneration of trabecular bone using porous ceramics.* Current Opinion in Solid State and Materials Science, 2003. **7**(4-5): p. 301-307.
79. Li, F., X. Huang, and G.J. Zhang, *Preparation of Ultra-High Temperature Ceramics–Based Materials by Sol-Gel Routes.* Recent Applications in Sol-Gel Synthesis, 2017: p. 39.
80. Studart, A.R., et al., *Processing routes to macroporous ceramics: a review.* Journal of the American Ceramic Society, 2006. **89**(6): p. 1771-1789.
81. Tiainen, H., et al., *Ultra-porous titanium oxide scaffold with high compressive strength.* Journal of Materials Science. Materials in Medicine, 2010. **21**(10): p. 2783-2792.
82. Kuboki, Y., Q. Jin, and H. Takita, *Geometry of carriers controlling phenotypic expression in BMP-induced osteogenesis and chondrogenesis.* JBJS, 2001. **83**(1_suppl_2): p. S105-S115.
83. Karageorgiou, V. and D. Kaplan, *Porosity of 3D biomaterial scaffolds and osteogenesis.* Biomaterials, 2005. **26**(27): p. 5474-5491.
84. French, R.H., *Origins and applications of London dispersion forces and Hamaker constants in ceramics.* Journal of the American Ceramic Society, 2000. **83**(9): p. 2117-2146.
85. Rahaman, M.N., *Ceramic Processing and Sintering*. 2017: CRC press.

86. Derjaguin, B., *A theory of interaction of particles in presence of electric double layers and the stability of lyophobe colloids and disperse systems.* Progress in Surface Science, 1993. **43**(1): p. 1-14.
87. Derjaguin, B. and L. Landau, *Theory of the stability of strongly charged lyophobic sols and of the adhesion of strongly charged particles in solutions of electrolytes.* Progress in Surface Science, 1993. **43**(1): p. 30-59.
88. Verwey, E., *Theory of the stability of lyophobic colloids.* The Journal of Physical Chemistry, 1947. **51**(3): p. 631-636.
89. Israelachvili, J.N., *Intermolecular and Surface Forces*. 2011: Academic press.
90. Hiemenz, P.C. and R. Rajagopalan, *Principles of Colloid and Surface Chemistry, revised and expanded*. Vol. 14. 1997: CRC press.
91. Park, S.-J. and M.-K. Seo, *Chapter 1 - Intermolecular Force*, in *Interface Science and Technology*, S.-J. Park and M.-K. Seo, Editors. 2011, Elsevier. p. 1-57.
92. Brown, M.A., A. Goel, and Z. Abbas, *Effect of Electrolyte Concentration on the Stern Layer Thickness at a Charged Interface.* Angewandte Chemie International Edition, 2016. **55**: p. 3790-3794.
93. Widegren, J. and L. Bergström, *Electrostatic stabilization of ultrafine titania in ethanol.* Journal of the American Ceramic Society, 2002. **85**(3): p. 523-528.
94. Brant, J., H. Lecoanet, and M.R. Wiesner, *Aggregation and deposition characteristics of fullerene nanoparticles in aqueous systems.* Journal of Nanoparticle Research, 2005. **7**(4-5): p. 545-553.
95. Kosmulski, M., J. Gustafsson, and J.B. Rosenholm, *Correlation between the zeta potential and rheological properties of anatase dispersions.* Journal of colloid and interface science, 1999. **209**(1): p. 200-206.
96. Grahame, D.C., *The electrical double layer and the theory of electrocapillarity.* Chemical reviews, 1947. **41**(3): p. 441-501.
97. Jiang, J., G. Oberdörster, and P. Biswas, *Characterization of size, surface charge, and agglomeration state of nanoparticle dispersions for toxicological studies.* Journal of Nanoparticle Research, 2009. **11**(1): p. 77-89.
98. Kosmulski, M. and J.B. Rosenholm, *High ionic strength electrokinetics of anatase in the presence of multivalent inorganic ions.* Colloids and Surfaces A: Physicochemical and Engineering Aspects, 2004. **248**(1-3): p. 121-126.
99. Kosmulski, M. and J.B. Rosenholm, *High ionic strength electrokinetics.* Advances in colloid and interface science, 2004. **112**(1-3): p. 93-107.
100. López Valdivieso, A., et al., *Temperature effect on the zeta potential and fluoride adsorption at the α-Al2O3/aqueous solution interface.* Journal of Colloid and Interface Science, 2006. **298**(1): p. 1-5.
101. de Lint, W.S., et al., *Ion adsorption parameters determined from zeta potential and titration data for a γ-alumina nanofiltration membrane.* Langmuir, 2003. **19**(14): p. 5861-5868.
102. Gustafsson, J., et al., *The influence of pH and NaCl on the zeta potential and rheology of anatase dispersions.* Colloids and Surfaces A: Physicochemical and Engineering Aspects, 2000. **175**(3): p. 349-359.
103. Grzadka, E. and S. Chibowski, *Influence of a kind of electrolyte and its ionic strength on the adsorption and zeta potential of the system: Polyacrylic acid/MnO2/electrolyte solution*. Vol. 43. 2009. 31-42.
104. Kosmulski, M. and J.B. Rosenholm, *Electroacoustic Study of Adsorption of Ions on Anatase and Zirconia from Very Concentrated Electrolytes.* The Journal of Physical Chemistry, 1996. **100**(28): p. 11681-11687.

105. Günther, L. and W. Peukert, *Control of coating properties by tailored particle interactions: relation between suspension rheology and film structure.* Colloids and Surfaces A: Physicochemical and Engineering Aspects, 2003. **225**(1): p. 49-61.
106. Schwartzwalder, K. and A. Somers, *Patent: US 3090094.* Method of making porous ceramic articles, 1963.
107. Carter, C.B. and M.G. Norton, *Ceramic Materials: Science and Engineering*. Vol. 716. 2007: Springer.
108. Tanaka, H., et al., *Strongly connected ex situ MgB_2 polycrystalline bulks fabricated by solid-state self-sintering.* Superconductor Science and Technology, 2012. **25**(11): p. 115022.
109. Kwon, O.-H., *Liquid Phase Sintering: Ceramics*, in *Encyclopedia of Materials: Science and Technology*. 2001.
110. De Jonghe, L., M. Rahaman, and S. Somiya, *Handbook of Advanced Ceramics, Chapter 4, Sintering of Ceramics*. 2003, Elsevier Science & Technology Books, Amsterdam, Netherlands.
111. Müller, B., et al., *Grain boundary corrosion of highly porous ceramic TiO_2 foams is reduced by annealing and quenching.* Journal of the European Ceramic Society, 2016. **36**(1): p. 179-188.
112. Kamachimudali, U., T. Sridhar, and B. Raj, *Corrosion of bio implants.* Sadhana, 2003. **28**(3-4): p. 601-637.
113. Teitelbaum, S.L., *Bone resorption by osteoclasts.* Science, 2000. **289**(5484): p. 1504-1508.
114. Silver, I., R. Murrills, and D. Etherington, *Microelectrode studies on the acid microenvironment beneath adherent macrophages and osteoclasts.* Experimental cell research, 1988. **175**(2): p. 266-276.
115. White, W.B., *Theory of corrosion of glass and ceramics.* Corrosion of glass, ceramics and ceramic superconductors, 1992: p. 2-28.
116. McCauley, R.A., *Corrosion of Ceramic and Composite Materials*. 2004: CRC Press.
117. Tiainen, H., et al., *Bone formation in TiO_2 bone scaffolds in extraction sockets of minipigs.* Acta biomaterialia, 2012. **8**(6): p. 2384-2391.
118. Haugen, H., et al., *Ceramic TiO2-foams: characterisation of a potential scaffold.* Journal of the European Ceramic Society, 2004. **24**(4): p. 661-668.
119. Verket, A., et al., *TiO_2 scaffolds in peri-implant dehiscence defects: an experimental pilot study.* Clinical oral implants research, 2016. **27**(10): p. 1200-1206.
120. Sabetrasekh, R., et al., *A novel ultra-porous titanium dioxide ceramic with excellent biocompatibility.* Journal of biomaterials applications, 2011. **25**(6): p. 559-580.
121. Deville, S., E. Saiz, and A.P. Tomsia, *Freeze casting of hydroxyapatite scaffolds for bone tissue engineering.* Biomaterials, 2006. **27**(32): p. 5480-5489.
122. Colombo, P. and J.R. Hellmann, *Ceramic foams from preceramic polymers.* Materials Research Innovations, 2002. **6**(5-6): p. 260-272.
123. Colombo, P., *Conventional and novel processing methods for cellular ceramics.* Philosophical Transactions of the Royal Society A: Mathematical, Physical and Engineering Sciences, 2006. **364**(1838): p. 109-124.
124. Fu, Q., et al., *Mechanical and in vitro performance of 13–93 bioactive glass scaffolds prepared by a polymer foam replication technique.* Acta biomaterialia, 2008. **4**(6): p. 1854-1864.
125. Gervaso, F., et al., *High-Performance hydroxyapatite scaffolds for bone tissue engineering applications.* International Journal of Applied Ceramic Technology, 2012. **9**(3): p. 507-516.

126. Ochoa, I., et al., *Permeability evaluation of 45S5 Bioglass®-based scaffolds for bone tissue engineering.* Journal of biomechanics, 2009. **42**(3): p. 257-260.
127. Xu, R., *Electrophoretic light scattering: Zeta potential measurement.* Particle characterization: Light scattering methods, 2002: p. 289-343.
128. Bhattacharjee, S., *DLS and zeta potential–what they are and what they are not?* Journal of Controlled Release, 2016. **235**: p. 337-351.
129. Henry, D., *The cataphoresis of suspended particles. Part I.—The equation of cataphoresis.* Proceedings of the Royal Society of London. Series A, Containing Papers of a Mathematical and Physical Character, 1931. **133**(821): p. 106-129.
130. Clogston, J.D. and A.K. Patri, *Zeta potential measurement*, in *Characterization of nanoparticles intended for drug delivery*. 2011, Springer. p. 63-70.
131. Kosmulski, M., *Chapter 2 Methods*, in *Surface Charging and Points of Zero Charge*. 2009, CRC press.
132. Bremmell, K.E. and J. Addai-Mensah, *Interfacial-chemistry mediated behavior of colloidal talc dispersions.* Journal of colloid and interface science, 2005. **283**(2): p. 385-391.
133. Hackley, V.A., et al., *Analysis of the isoelectric point in moderately concentrated alumina suspensions using electroacoustic and streaming potential methods.* Journal of dispersion science and technology, 2002. **23**(5): p. 601-617.
134. Kosmulski, M., *Chapter 1 Introduction*, in *Surface Charging and Points of Zero Charge*. 2009, CRC press.
135. Bousse, L., et al., *Zeta potential measurements of* Ta_2O_5 *and* SiO_2 *thin films.* Journal of Colloid and Interface Science, 1991. **147**(1): p. 22-32.
136. O'brien, R., D. Cannon, and W. Rowlands, *Electroacoustic determination of particle size and zeta potential.* Journal of Colloid and Interface Science, 1995. **173**(2): p. 406-418.
137. Guerin, M. and J.C. Seaman, *Characterizing clay mineral suspensions using acoustic and electroacoustic spectroscopy-A review.* Clays and Clay Minerals, 2004. **52**(2): p. 145-157.
138. Song, J.H. and J.R.G. Evans, *The effect of undispersed agglomerates on the relative viscosity of ceramic moulding suspensions.* Journal of Materials Science Letters, 1994. **13**(22): p. 1642-1644.
139. Yunos, D.M., O. Bretcanu, and A.R. Boccaccini, *Polymer-bioceramic composites for tissue engineering scaffolds.* Journal of Materials Science, 2008. **43**(13): p. 4433-4442.
140. Hulbert, S., et al., *Potential of ceramic materials as permanently implantable skeletal prostheses.* Journal of biomedical materials research, 1970. **4**(3): p. 433-456.
141. Lan Levengood, S.K., et al., *Multiscale osteointegration as a new paradigm for the design of calcium phosphate scaffolds for bone regeneration.* Biomaterials, 2010. **31**(13): p. 3552-3563.
142. Murphy, C.M., M.G. Haugh, and F.J. O'Brien, *The effect of mean pore size on cell attachment, proliferation and migration in collagen–glycosaminoglycan scaffolds for bone tissue engineering.* Biomaterials, 2010. **31**(3): p. 461-466.
143. Tsuruga, E., et al., *Pore size of porous hydroxyapatite as the cell-substratum controls BMP-induced osteogenesis.* The Journal of Biochemistry, 1997. **121**(2): p. 317-324.
144. Schwartz, I., et al., *Calvarial bone repair with porous D, L-polylactide.* Otolaryngology—Head and Neck Surgery, 1995. **112**(6): p. 707-713.
145. Tiainen, H., D. Wiedmer, and H.J. Haugen, *Processing of highly porous* TiO_2 *bone scaffolds with improved compressive strength.* Journal of the European Ceramic Society, 2013. **33**(1): p. 15-24.

146. Fernández, B., L. Lobo, and R. Pereiro, *Atomic Absorpton Spectrometry | Fundamentals, Instrumentation and Capabilities*, in *Encyclopedia of Analytical Science (Third Edition)*, P. Worsfold, et al., Editors. 2019, Academic Press: Oxford. p. 137-143.
147. McGregor, D.A., et al., *Direct determination of nonmetals in solution with atomic spectrometry.* Analytical Chemistry, 1988. **60**(19): p. 1089A-1098A.
148. Resano, M., M.R. Flórez, and E. García-Ruiz, *Progress in the determination of metalloids and non-metals by means of high-resolution continuum source atomic or molecular absorption spectrometry. A critical review.* Analytical and Bioanalytical Chemistry, 2014. **406**(9): p. 2239-2259.
149. Mello, P.A., et al., *Analytical methods for the determination of halogens in bioanalytical sciences: a review.* Analytical and bioanalytical chemistry, 2013. **405**(24): p. 7615-7642.
150. Liu, H.-t. and S.-J. Jiang, *Dynamic reaction cell inductively coupled plasma mass spectrometry for determination of silicon in steel.* Spectrochimica Acta Part B: Atomic Spectroscopy, 2003. **58**(1): p. 153-157.
151. Bowen, D.K. and B.K. Tanner, *High Resolution X-ray Diffractometry and Topography*. 1998: CRC press.
152. Zhou, W., et al., *Fundamentals of Scanning Electron Microscopy (SEM)*, in *Scanning Microscopy for Nanotechnology*. 2006, Springer. p. 1-40.
153. Fultz, B. and J.M. Howe, *Transmission Electron Microscopy and Diffractometry of Materials*. 2012: Springer Science & Business Media.
154. Williams, D. and C. Carter, *Part 1: Basics.* Transmission Electron Microscopy, 2009: p. 1-193.
155. Mittemeijer, E.J., *Crystallography*, in *Fundamentals of Materials Science: The Microstructure–Property Relationship Using Metals as Model Systems*. 2011, Springer Berlin Heidelberg: Berlin, Heidelberg. p. 103-200.
156. Carter, C.B. and D.B. Williams, *Transmission Electron Microscopy: Diffraction, Imaging, and Spectrometry*. 2016: Springer.
157. Gómez-Florit, M., et al., *TiO2 scaffolds sustain differentiation of MC3T3-E1 cells.* Journal of Biomaterials and Tissue Engineering, 2012. **2**(4): p. 336-344.
158. Scherberich, A., et al., *Adipose tissue-derived progenitors for engineering osteogenic and vasculogenic grafts.* Journal of cellular physiology, 2010. **225**(2): p. 348-353.
159. Ramakrishna, S., et al., *6 - Safety Testing of a New Medical Device*, in *Medical Devices*, S. Ramakrishna, et al., Editors. 2015, Woodhead Publishing. p. 137-153.
160. Legrand, C., et al., *Lactate dehydrogenase (LDH) activity of the number of dead cells in the medium of cultured eukaryotic cells as marker.* Journal of biotechnology, 1992. **25**(3): p. 231-243.
161. Chan, F.K.-M., K. Moriwaki, and M.J. De Rosa, *Detection of Necrosis by Release of Lactate Dehydrogenase Activity*, in *Immune Homeostasis*. 2013, Springer. p. 65-70.
162. Kadri, K., *Polymerase Chain Reaction (PCR): Principle and Applications*, in *Perspectives on Polymerase Chain Reaction*. 2019, IntechOpen.
163. Bustin, S., et al., *Quantitative real-time RT-PCR–a perspective.* Journal of molecular endocrinology, 2005. **34**(3): p. 597-601.
164. Kubista, M., et al., *The real-time polymerase chain reaction.* Molecular aspects of medicine, 2006. **27**(2-3): p. 95-125.
165. Arya, M., et al., *Basic principles of real-time quantitative PCR.* Expert Review of Molecular Diagnostics, 2005. **5**(2): p. 209-219.
166. Kreuzer, K.-A., et al., *Highly sensitive and specific fluorescence reverse transcription-PCR assay for the pseudogene-free detection of β-actin transcripts as quantitative reference.* Clinical Chemistry, 1999. **45**(2): p. 297-300.

167. Stein, G.S., et al., *Transcriptional control of osteoblast growth and differentiation.* Physiological reviews, 1996. **76**(2): p. 593-629.

168. Miron, R. and Y. Zhang, *Osteoinduction: a review of old concepts with new standards.* Journal of dental research, 2012. **91**(8): p. 736-744.

169. Fuh, L.J., et al., *Variations in bone density at dental implant sites in different regions of the jawbone.* Journal of oral rehabilitation, 2010. **37**(5): p. 346-351.

170. Lioubavina-Hack, N., N.P. Lang, and T. Karring, *Significance of primary stability for osseointegration of dental implants.* Clinical oral implants research, 2006. **17**(3): p. 244-250.

171. Giannoudis, P.V., H. Dinopoulos, and E. Tsiridis, *Bone substitutes: an update.* Injury, 2005. **36**(3): p. S20-S27.

172. Giannoudis, P.V., T.A. Einhorn, and D. Marsh, *Fracture healing: the diamond concept.* Injury, 2007. **38**: p. S3-S6.

173. Deisinger, U. *Generating porous ceramic scaffolds: processing and properties*. in *Key Engineering Materials*. 2010. Trans Tech Publ.

174. Narkevica, I., et al., *Electrically active and 3D porous TiO_2-x ceramic scaffolds for bone tissue regeneration.* Journal of the European Ceramic Society, 2017. **37**(2): p. 833-840.

175. Stipniece, L., et al., *Novel scaffolds based on hydroxyapatite/poly (vinyl alcohol) nanocomposite coated porous TiO2 ceramics for bone tissue engineering.* Ceramics International, 2016. **42**(1): p. 1530-1537.

176. Ackler, H.D., R.H. French, and Y.-M. Chiang, *Comparisons of Hamaker constants for ceramic systems with intervening vacuum or water: From force laws and physical properties.* Journal of Colloid and Interface Science, 1996. **179**(2): p. 460-469.

177. Jung, G.-Y., Y.-J. Park, and J.-S. Han, *Effects of HA released calcium ion on osteoblast differentiation.* Journal of Materials Science: Materials in Medicine, 2010. **21**(5): p. 1649-1654.

178. Marie, P.J., D. Felsenberg, and M.L. Brandi, *How strontium ranelate, via opposite effects on bone resorption and formation, prevents osteoporosis.* Osteoporosis International, 2011. **22**(6): p. 1659-1667.

179. Zreiqat, H., et al., *Mechanisms of magnesium-stimulated adhesion of osteoblastic cells to commonly used orthopaedic implants.* Journal of Biomedical Materials Research, 2002. **62**(2): p. 175-184.

180. Nielsen, S.P., *The biological role of strontium.* Bone, 2004. **35**(3): p. 583-588.

181. Blair, H.C., et al., *Calcium and bone disease.* Biofactors, 2011. **37**(3): p. 159-167.

182. Castiglioni, S., et al., *Magnesium and osteoporosis: current state of knowledge and future research directions.* Nutrients, 2013. **5**(8): p. 3022-3033.

183. Leite, A.l.J., et al., *Strontium-doped bioactive glass nanoparticles in osteogenic commitment.* ACS applied materials & interfaces, 2018. **10**(27): p. 23311-23320.

184. Gu, H., et al., *The stimulation of osteogenic differentiation of human adipose-derived stem cells by ionic products from akermanite dissolution via activation of the ERK pathway.* Biomaterials, 2011. **32**(29): p. 7023-7033.

185. Marie, P.J., et al., *Mechanisms of action and therapeutic potential of strontium in bone.* Calcified Tissue International, 2001. **69**(3): p. 121-129.

186. Yamasaki, Y., et al., *Synthesis of functionally graded $MgCO_3$ apatite accelerating osteoblast adhesion.* Journal of Biomedical Materials Research, 2002. **62**(1): p. 99-105.

187. Peng, S., et al., *Strontium promotes osteogenic differentiation of mesenchymal stem cells through the Ras/MAPK signaling pathway.* Cellular Physiology and Biochemistry, 2009. **23**(1-3): p. 165-174.

188. Wang, G., et al., *Magnesium ion implantation on a micro/nanostructured titanium surface promotes its bioactivity and osteogenic differentiation function.* International journal of nanomedicine, 2014. **9**: p. 2387.
189. Barradas, A.M., et al., *A calcium-induced signaling cascade leading to osteogenic differentiation of human bone marrow-derived mesenchymal stromal cells.* Biomaterials, 2012. **33**(11): p. 3205-3215.
190. Shih, Y.-h., et al., *The effect of electrolytes on the aggregation kinetics of titanium dioxide nanoparticle aggregates.* Journal of Nanoparticle Research, 2012. **14**(8): p. 924.
191. Suttiponparnit, K., et al., *Role of surface area, primary particle size, and crystal phase on titanium dioxide nanoparticle dispersion properties.* Nanoscale Research Letters, 2011. **6**(1): p. 27.
192. Davies, J. and J. Binner, *Coagulation of electrosterically dispersed concentrated alumina suspensions for paste production.* Journal of the European Ceramic Society, 2000. **20**(10): p. 1555-1567.
193. Brezny, R., D.J. Green, and C.Q. Dam, *Evaluation of Strut Strength in Open-Cell Ceramics.* Journal of the American Ceramic Society, 1989. **72**(6): p. 885-889.
194. Brown, D.D. and D.J. Green, *Investigation of strut crack formation in open cell alumina ceramics.* Journal of the American Ceramic Society, 1994. **77**(6): p. 1467-1472.
195. Kodo, M., et al., *Doping effect of divalent cations on sintering of polycrystalline yttria.* Journal of the European Ceramic Society, 2010. **30**(13): p. 2741-2747.
196. Chen, C.-J. and J.-M. Wu, *The effect of niobium, calcium and lanthanum dopants on the crystallite growth of TiO2 powders.* Materials Science and Engineering: B, 1990. **5**(3): p. 377-383.
197. Hannink, G. and J.C. Arts, *Bioresorbability, porosity and mechanical strength of bone substitutes: what is optimal for bone regeneration?* Injury, 2011. **42**: p. S22-S25.
198. Terwilliger, C.D. and Y.-M. Chiang, *Size-dependent solute segregation and total solubility in ultrafine polycrystals: Ca in TiO2.* Acta Metallurgica et Materialia, 1995. **43**(1): p. 319-328.
199. Zhang, F., et al., *Effect of cation dopant radius on the hydrothermal stability of tetragonal zirconia: Grain boundary segregation and oxygen vacancy annihilation.* Acta Materialia, 2016. **106**: p. 48-58.
200. Matsui, K., H. Yoshida, and Y. Ikuhara, *Nanocrystalline, ultra-degradation-resistant zirconia: its grain boundary nanostructure and nanochemistry.* Scientific reports, 2014. **4**: p. 4758.
201. Zhang, F., et al., *Highly-translucent, strong and aging-resistant 3Y-TZP ceramics for dental restoration by grain boundary segregation.* Acta biomaterialia, 2015. **16**: p. 215-222.
202. Yan, M.F. and W.W. Rhodes, *Preparation and properties of TiO_2 varistors.* Applied Physics Letters, 1982. **40**(6): p. 536-537.
203. Santhosh, P.N., D.K. Kharat, and S.K. Date, *Effect of strontium substitution in (Nb, Bi) doped TiO_2 varistors.* Materials Letters, 1996. **28**(1): p. 37-41.
204. Chen, I.-W. and X.-H. Wang, *Sintering dense nanocrystalline ceramics without final-stage grain growth.* Nature, 2000. **404**(6774): p. 168-171.
205. Kim, B.-N., et al., *Effects of heating rate on microstructure and transparency of spark-plasma-sintered alumina.* Journal of the European Ceramic Society, 2009. **29**(2): p. 323-327.
206. Mazaheri, M., A. Zahedi, and S. Sadrnezhaad, *Two-step sintering of nanocrystalline ZnO compacts: effect of temperature on densification and grain growth.* Journal of the American Ceramic Society, 2008. **91**(1): p. 56-63.

207. López, T., et al., *Synthesis and Characterization of TiO2−MgO Mixed Oxides Prepared by the Sol−Gel Method.* Langmuir, 1999. **15**(18): p. 5689-5693.
208. Bokhimi, X., et al., *Structure and Composition of the Nanocrystalline Phases in a MgO−TiO2 System Prepared via Sol−Gel Technique.* Chemistry of Materials, 1999. **11**(10): p. 2716-2721.
209. Mikeska, K.R., S.J. Bennison, and S.L. Grise, *Corrosion of ceramics in aqueous hydrofluoric acid.* Journal of the American Ceramic Society, 2000. **83**(5): p. 1160-1164.
210. Kingery, W., *Plausible Concepts Necessary and Sufficient for Interpretation of Ceramic Grain-Boundary Phenomena: II, Solute Segregation, Grain-Boundary Diffusion, and General Discussion.* Journal of the American Ceramic Society, 1974. **57**(2): p. 74-83.
211. Sciti, D., S. Guicciardi, and A. Bellosi, *Effect of annealing treatments on microstructure and mechanical properties of liquid-phase-sintered silicon carbide.* Journal of the European Ceramic Society, 2001. **21**(5): p. 621-632.
212. Martin, R., et al., *Bone ingrowth and mechanical properties of coralline hydroxyapatite 1 yr after implantation.* Biomaterials, 1993. **14**(5): p. 341-348.
213. Martin, R., et al., *Effects of bone ingrowth on the strength and non-invasive assessment of a coralline hydroxyapatite material.* Biomaterials, 1989. **10**(7): p. 481-488.
214. Tamai, N., et al., *Novel hydroxyapatite ceramics with an interconnective porous structure exhibit superior osteoconduction in vivo.* Journal of Biomedical Materials Research: An Official Journal of The Society for Biomaterials and The Japanese Society for Biomaterials, 2002. **59**(1): p. 110-117.
215. Trecant, M., et al., *Mechanical changes in macro-porous calcium phosphate ceramics after implantation in bone.* Clinical materials, 1994. **15**(4): p. 233-240.
216. Bohner, M., et al., *Commentary: deciphering the link between architecture and biological response of a bone graft substitute.* Acta biomaterialia, 2011. **7**(2): p. 478-484.
217. Botchwey, E.A., et al., *Tissue engineered bone: Measurement of nutrient transport in three-dimensional matrices.* Journal of Biomedical Materials Research Part A: An Official Journal of The Society for Biomaterials, The Japanese Society for Biomaterials, and The Australian Society for Biomaterials and the Korean Society for Biomaterials, 2003. **67**(1): p. 357-367.
218. Wiedmer, D., et al., *Antibacterial surface coating for bone scaffolds based on the dark catalytic effect of titanium dioxide.* ACS applied materials & interfaces, 2018. **10**(42): p. 35784-35793.
219. Yang, F., et al., *Strontium enhances osteogenic differentiation of mesenchymal stem cells and in vivo bone formation by activating Wnt/catenin signaling.* Stem cells, 2011. **29**(6): p. 981-991.
220. Isaac, J., et al., *Effects of strontium-doped bioactive glass on the differentiation of cultured osteogenic cells.* European Cells & Materials Journal, 2011. **21**: p. 130-43.

8 APPENDIX

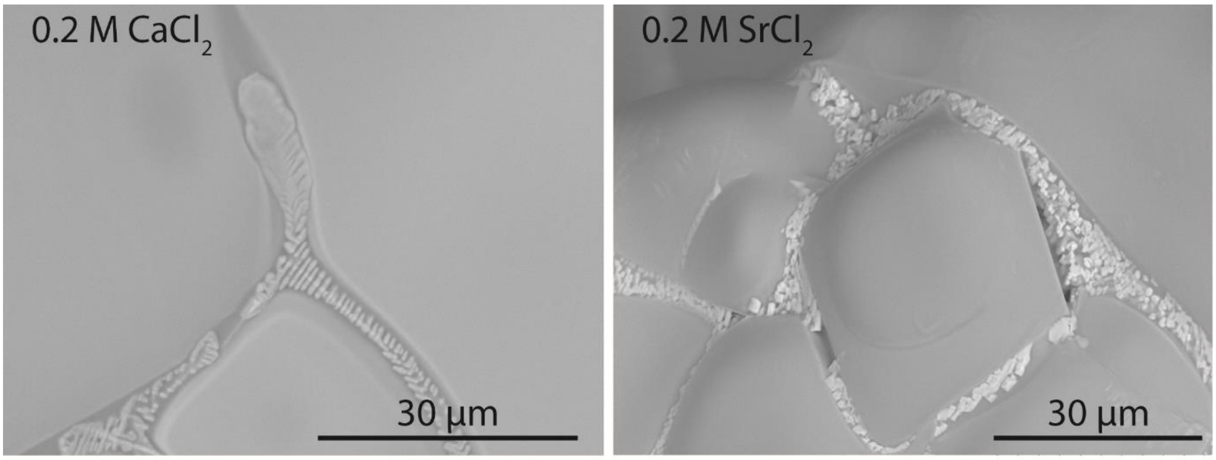

Appendix A: Grain boundary of 0.2 M $CaCl_2$ and $SrCl_2$ doped TiO_2 scaffolds

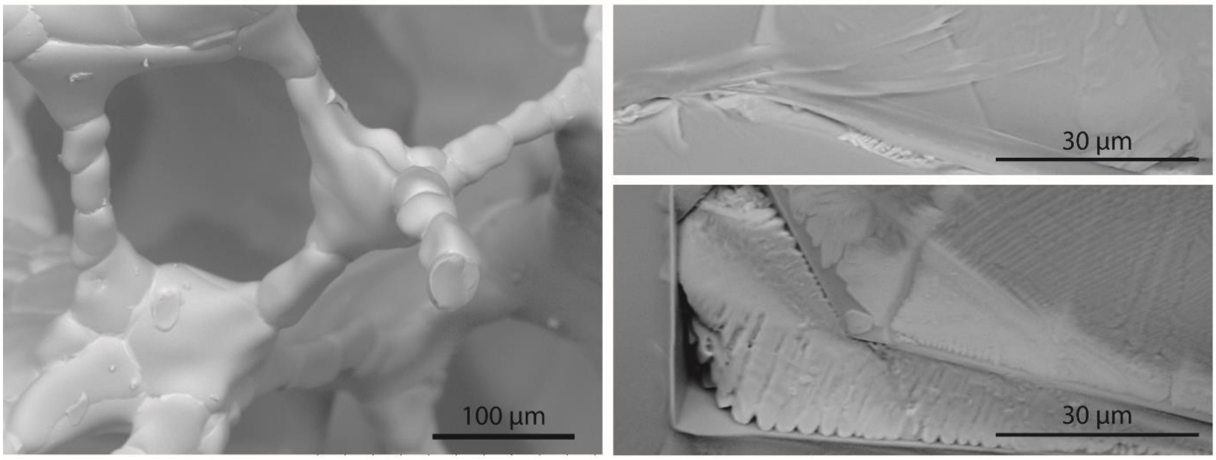

Appendix B: Strut morphology and grain boundaries of 0.1 M $SrCl_2$ scaffolds sintered at 1600°C and cooled with a slow cooling rate of 2 K/min

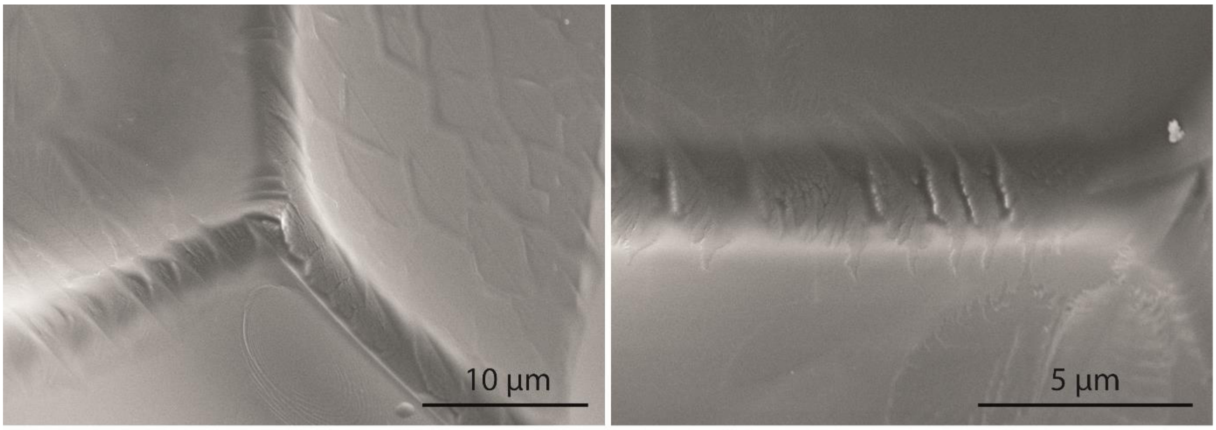

Appendix C: Grain boundaries of 0.1 M $MgCl_2$ doped TiO_2 scaffolds sintered at 1600°C and air quenched

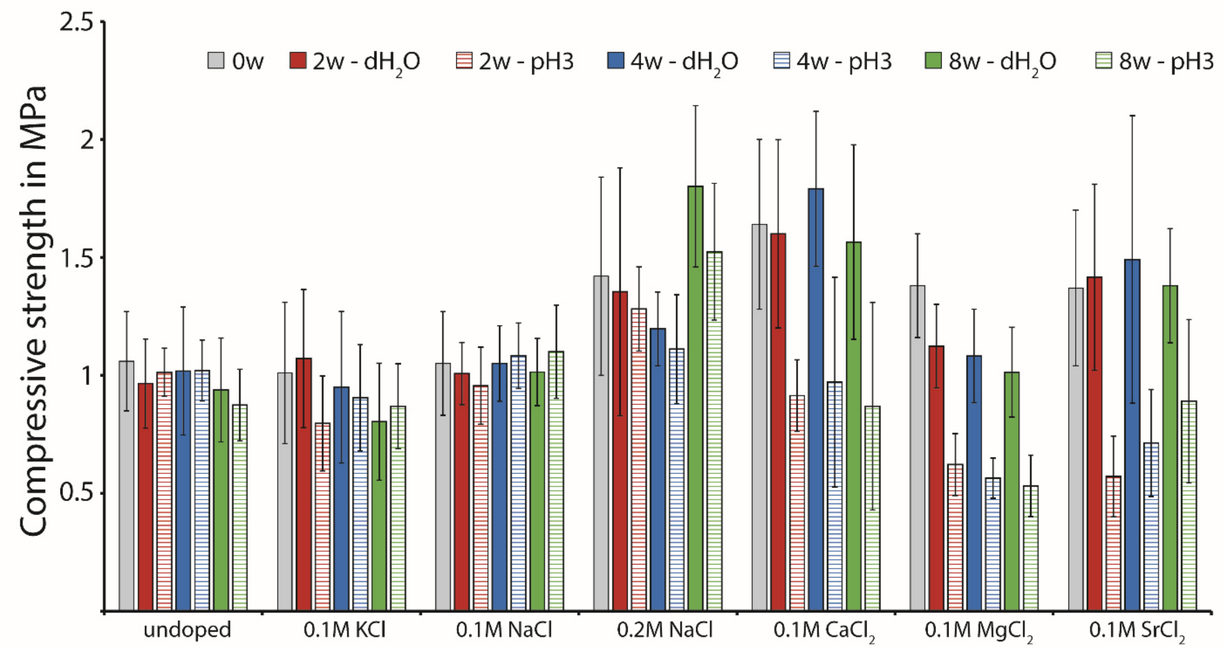

Appendix D: Long term corrosion test of differently doped TiO_2 scaffolds exposed to dH_2O and 1 mM HCl (pH3) solution for 2, 4 and 8 weeks

Ceramics International 44 (2018) 6265–6271

Contents lists available at ScienceDirect

Ceramics International

journal homepage: www.elsevier.com/locate/ceramint

Coagulated concentrated anatase slurry leads to improved strength of ceramic TiO_2 bone scaffolds

Anne Klemm, Hanna Tiainen*

University of Oslo, Department of Biomaterials, Institute of Clinical Dentistry, P.O. Box 1109 Blindern, 0317 Oslo, Norway

ARTICLE INFO

Keywords:
TiO_2
Zeta potential
Concentrated suspension
Grain boundary formation
Porous ceramic

ABSTRACT

Slurry behaviour has an important influence on the properties of ceramic scaffolds produced by the polymer sponge method. By adding chloride salts to the TiO_2 slurry, the viscosity was increased depending on the chloride concentration at low pH and high particle concentration. Slurries with higher viscosity led to closed and dense scaffold struts combined with high porosity, resulting in a compressive strength over 1.6 MPa. Furthermore, scaffold prepared with 0.1 M $CaCl_2$ and $SrCl_2$ showed the formation of Ca- and Sr-rich phases at the grain boundaries. These ions were also shown to reduce the activation energy for grain growth in the TiO_2 scaffold as indicated by the significantly larger grain size. Ca^{2+}-doped scaffolds had the highest compressive strength, while the strength of Sr^{2+}-doped scaffolds was reduced by the formation of a solid solution phase below the sintering temperature.

1. Introduction

Titanium dioxide is well-known for its biocompatibility in different biomedical applications and has shown potential particularly for use as a bone scaffold [1–3]. These scaffolds can be used as a support structure during the self-healing process of bone [4]. Important properties for such a non-resorbable scaffold include sufficient pore size and interconnectivity, which allow cell ingrowth and vascularization, and a large surface area-to-volume ratio, which enables cell adhesion [5]. These properties are crucial for tissue integration which is vital for the success of such scaffolds. Previous studies have shown the success of TiO_2 scaffolds during the healing process in non-critical size defects in bones of minipigs resulting in vascularization and formation of bone lamellae in the inner region of the scaffold [2,6].

Combined with a high porosity, a bone scaffold has to have a high compressive strength which should be similar to trabecular bone which has a compressive strength between 2 and 12 MPa [7]. Tiainen et al. has shown that by increasing the porosity from 82% to 94%, the compressive strength of TiO_2 scaffolds is decreased from 1.7MPa to 0.4 MPa [8]. Other studies have shown the loss in compressive strength by increasing the porosity and the other way around [9,10]. This leads to the present challenge of combining high porosity and high compressive strength in TiO_2 bone scaffolds to ensure tissue integration and a support structure that is similar to natural bone in strength.

To find the best compromise between high porosity and compressive strength, the polymer sponge replication method can be used to produce ceramic bone scaffolds [11]. Using this technique, a sponge foam is coated with TiO_2 slurry and after burning out the polymer template and sintering the green body the final strong scaffold is formed. However, it is extremely important to control the behaviour of the slurry when utilizing this technique. To obtain the necessary scaffold properties, the slurry must have a shear thinning effect, which enables the removal of excess slurry to avoid a large amount of blocked pores [12]. The presence of blocked pores causes a decrease in the overall porosity and interconnectivity within the scaffold, which can potentially hinder cell infiltration and tissue integration. A further important property of the slurry is the maximum viscosity, which should be high enough to produce a uniform coating on the polymer struts inside the foam, ensuring sufficient compressive strength. To guarantee both properties, the TiO_2 slurry must be a dispersion without agglomeration of the TiO_2 particles.

Agglomerations occur in a suspension if the attractive van der Waals forces are higher than the repulsive forces. A dispersant enables control of the balance between the two forces to get a viscous slurry without agglomerations. However, this strategy leads to residual porosity in the final ceramic body because of evaporation of the plasticizer [13]. Especially when producing highly porous bone scaffolds, micropores resulting from the evaporation of agents can cause a decrease in compressive strength. Another strategy is to influence the electrical double layer (EDL) around TiO_2 particles, which in turn affects the repulsive forces in a suspension, by changing the pH. The influence of pH on the zeta potential (ζ potential), which defines the EDL thickness, is well

---

* Corresponding author.
E-mail address: hanna.tiainen@odont.uio.no (H. Tiainen).

https://doi.org/10.1016/j.ceramint.2018.01.013
Received 3 November 2017; Received in revised form 2 January 2018; Accepted 3 January 2018

known [14]. Tiainen et al. showed that by changing the pH to 1.5–1.7, the TiO_2 slurry used for the scaffold production is stable and can be used for successful scaffold production [8]. Additionally, Davies and Binner studied the influence of ions on the ζ potential and the ceramic suspension viscosity and showed that by adding ions to the ceramic slurry, the attractive potential increases and a network of individual, non-touching particles is created [15]. In relation to the production of bone scaffolds, it is of prime interest to investigate the influence of ionic strength of the dispersion on slurry rheology, especially on the most important slurry properties, such as shear thinning, maximal viscosity and stability without agglomeration.

To achieve the goal of combining high porosity and high compressive strength of TiO_2 bone scaffolds, this study focuses on controlling the slurry stability and viscosity by adding different chloride salts to the ceramic slurry. To investigate this, general mono- and divalent salts with different ionic radii have been selected. Furthermore the effect of the used salts (NaCl, KCl, $CaCl_2$, $SrCl_2$ and $MgCl_2$) on the sintering behaviour of TiO_2 was assessed and the changes in scaffold microstructure and mechanical properties were characterized.

2. Material and methods

2.1. Sample preparation

For producing TiO_2 bone scaffolds, the polymer foam replication method was used. The slurry was prepared by adding 65 g of anatase powder (HOMBITAN FF-Pharma, Sachtleben Chemie GmbH, Duisburg, Germany) into 25 ml of 0.1 M (NaCl, KCl, $CaCl_2$, $SrCl_2$ and $MgCl_2$) or 25 ml of 0.2 M NaCl solution. Higher powder concentrations resulted in agglomerated slurries, which are not recommended for scaffold production. The slurry was adjusted to a work pH 1.5–1.7 by adding 1 M HCl and was stirred at 5000 rpm for 2.5 h at a temperature between 15 and 17 °C (Dispermat Ca-40, VMA-Gertzmann GmbH, Reichshof, Germany).

After coating the polymer foams (60 pores per inch, diameter 10 mm, height 10 mm, Bulbern S, Eurofoam GmbH, Wiesbaden, Germany) with the prepared slurry, excess slurry was squeezed out and the samples dried for 24 h at room temperature. Before sintering the scaffolds, the polymer template was burned out. Burn out of the polymer was performed at 450 °C for 1 h with a heating rate of 1 K/min for avoiding disruptions of the ceramic structure. For ensuring the total decomposition, the temperature was increased to 1100 °C for 5 h with a heating rate of 1 K/min. With a heating rate of 15.5 K/min, the scaffolds were sintered at a temperature of 1500 °C for 20 h (HTC-08/16, Nabertherm GmbH, Lilienthal, Germany) and cooled down to room temperature.

2.2. Slurry rheology

The viscometer Bohlin Visco 88 (Malvern Instruments, Malvern, UK) was used to investigate the rheology of all prepared slurries. The viscosity and shear stress were measured as a function of shear rate in the range of 2.46–100 1/s. The bob and cup was defined as C25, the measurement was at room temperature with increasing and decreasing shear rates to show possible hysteresis effects. Best fit rheological model analysis was done using standard Bohlin viscometer software.

2.3. ζ potential measurement

To investigate the effect of ionic strength and pH on the ζ potential, the Zetasizer Nano ZS with an automatic titration system MPT-2 (Malvern Instruments, UK) was used. 50 mg TiO_2 powder was added to 1 l of deionized water and the suspension was bath sonicated for 10 min. After settling down of agglomerates for 10 min, 15 ml suspension was mixed with 15 ml 0.2 M concentrated salt solution. To ensure complete surface reactions and a stable ζ potential, the measurements were done after 3 days, except for NaCl samples the measurements were done after 6 days. The measurement itself was performed from the native pH, which varied between the samples from pH 5–9 to acidic (pH 1.6) or basic (pH 9) values. For each direction, three independent samples were measured three times. The ζ potential was calculated as an average of all measurement points.

Additionally slurries at the work pH 1.7 and a higher pH around 2.4 were prepared, as described before, and the ζ potential was measured. Because the slurry was stable over time, the slurry was centrifuged for 15 min at 5500*g*. This supernatant was measured three times and the ζ potential calculated by the average of the three measurements.

To ensure no precipitation occurs between the salt cations and potential impurity ions dissolved from the TiO_2 particle surface in concentrated suspension, the particle size of the supernatant for the slurry prepared in water without the addition of chloride salt was measured using dynamic light scattering (Zetasizer Nano ZS, Malvern Instruments, UK) before and after addition of chloride salts to reach final cation concentration of 0.1 M.

2.4. X-ray photoelectron spectroscopy (XPS)

Chemical surface composition of the used anatase powder was analysed using x-ray photoelectron spectroscopy (Kratos AXIS Ultra DLD, Kratos Analytical, UK) using monochromatic Al-Kα radiation (hv = 1486.6 eV) at 10 mA current and 15 kV voltage. Survey spectrum was recorded at pass energy of 80 eV and the quantification of the detected chemical elements was performed using CasaXPS software package (Casa Software, UK). Binding energy (BE) scale was calibrated by assigning the hydrocarbon peak to BE of 284.8 eV.

2.5. Scaffold characterization

Micro computed tomography (SkyScan1172, Bruker microCT, Kontich, Belgium) was used to determine 3D scaffold parameters. Four scaffolds (n = 4) were placed in a plastic holder and by using a voltage of 100 kV, current of 100 µA, 6 µm voxel and 0.5 mm aluminium filter, three x-ray absorption images were taken every 0.4° up to a total of 180°. For reconstruction of a 3D model and calculation of parameters, the Skyscan software's NRecon, CTan and CTvox (Bruker, Billerica, USA) were used. The compared parameters were strut thickness, pore size and total porosity. For an optical verification of these parameters, scanning electron microscope TM3030 (Hitachi High-Technologies Europe GmbH, Krefeld, Germany) was used. The samples were mounted on an aluminium holder with carbon tape and copper conductive tape. SEM images were made with backscattered electrons at 15 kV voltage. The grain size was calculated from three different scaffolds using ImageJ and a magnification of 800 (control group without salt and monovalent salt scaffolds n = 3; divalent salt scaffolds n = 9). Beside the SEM, the energy dispersive x-ray spectroscopy (Quantax 70, Bruker, Billerica, USA) was used to detect the chemical elements in grain boundaries.

2.6. Compressive strength

Uniaxial mechanical testing machine Zwick/Roell Z2.5 (Zwick GmbH & Co. KG, Ulm, Germany) with a 1 kN load cell was used to investigate the compressive strength of all produced scaffolds (n = 10). The testing speed was defined as 100 mm/min, the preload as 0.5 N and the termination condition as 15% of the highest measured peak. The Test Expert II software was used to calculate the compressive strength on the basis of scaffold diameter and maximum force until failure.

2.7. Statistical analysis

Statistical comparison of compressive strength, pore size, porosity and strut thickness was performed using one-way analysis of variance

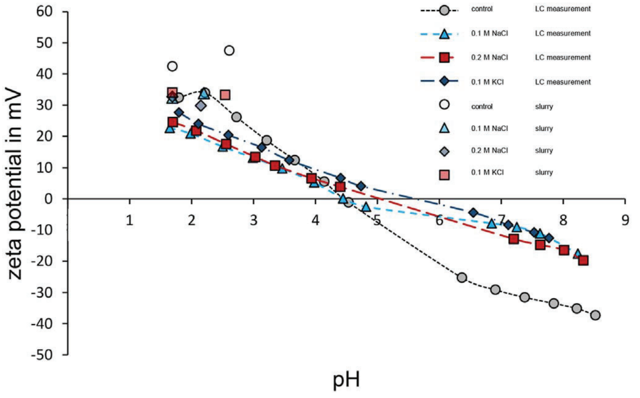

Fig. 1. ζ potential of 1.1 electrolyte samples. The lines show the ζ potential measurement with 25 mg/l particle concentration (LC – low concentration). The dots show the slurry measurement. The ζ potential of slurries with monovalent counterions is reduced and a stable suspension without agglomeration is present.

(ANOVA) test followed by pairwise comparisons performed using Holm–Sidak method. The overall significance level was $p < 0.05$ and $n = 10$ for compressive strength analysis and $n = 4$ for other scaffold properties. Statistical comparison of grain size was performed using one-way analysis of variance on Ranks (ANOVA on Ranks) test followed by pairwise comparisons performed using Tukey Test. The overall significance level was $p < 0.05$ and $n = 34$.

3. Results

3.1. Influence of chloride salts on ζ potential and slurry viscosity

As shown in Fig. 1, the isoelectric point (IEP) for the used anatase TiO_2 powder was found at pH 4.6, which is calculated by regression of the measurement points. Furthermore, this powder showed a high ζ potential around 32.5 mV at a low pH (pH 1.65) and ionic strength 0.022 mol/l.

The location of the IEP remained unchanged for 0.1 M NaCl suspensions indicating inert behaviour of the electrolyte (Fig. 1). By increasing the concentration to 0.2 M an IEP shift of 1 unit is observed. An IEP shift and therefore a non-inert behaviour was observed for 0.1 M KCl as well. At the pH 1.7 (work pH for slurries), the measurements showed a decreased ζ potential in the presence of monovalent ions. Also, the measurement with the supernatant of centrifuged slurries showed a decreased ζ potential at a low work pH at 1.7. The comparison of both measurements showed that the ζ potential in slurries is higher. Furthermore, the comparison of both measurements showed a similar development of ζ potential depending on pH.

Fig. 2 shows the ζ potential measurements for the used divalent salts. All used salts showed a non-inert behaviour manifested as an IEP shift higher than 3 units. The adsorption of $MgCl_2$ showed a fundamental change in TiO_2 particle surface properties and no IEP was observed within the measured pH range. The slurry measurement showed a similar ζ potential of approximately 29 mV for all three salts, which is lower than the ζ potential measurement of the control slurry without salt at similar pH. The $MgCl_2$ slurry measurement at pH 2.2 showed a further decreased ζ potential, which confirms the ζ potential measurement using samples with lower particle concentration (25 mg/l). Slurries prepared with 0.1 M $CaCl_2$ and $SrCl_2$ at a pH 2.2 showed to be unstable due to agglomerations and no ζ potential measurement data is available.

All investigated slurries showed a shear thinning behaviour which is defined by decreasing viscosity with increased shear rate (Fig. 3). The flow behaviour of all prepared slurries was characterized by Casson model [16]. Slurries prepared with 0.1 M NaCl and KCl showed the same rheological behaviour with similar maximum viscosities. The same was observed for 0.2 M NaCl and divalent salt slurries.

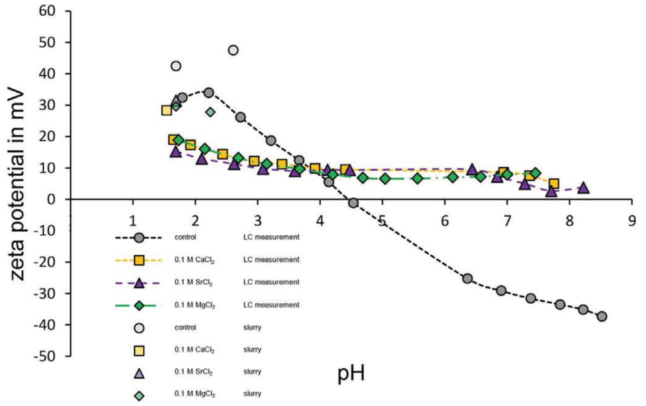

Fig. 2. ζ potential of 1–2 electrolyte samples. The lines show the ZP measurement with 25 mg/l particle concentration (LC – low concentration). The dots show the slurry measurement. The ζ potential in LC samples was seriously reduced. The slurry measurement for all samples at pH 1.7 show a reduced ζ potential, but a stable suspension. A non-stable suspension with agglomerates was observed for $CaCl_2$ and $SrCl_2$ slurries at pH ≥ 2.

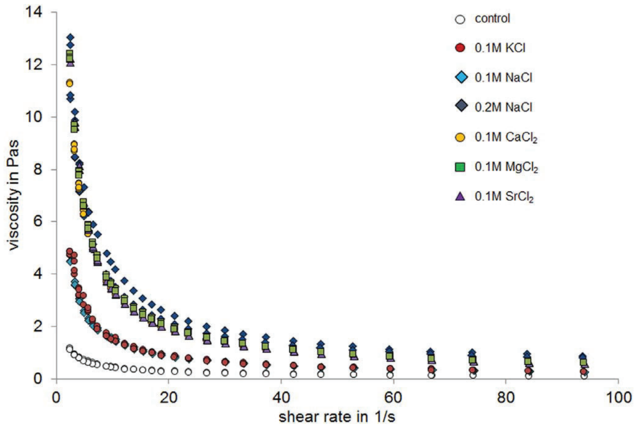

Fig. 3. Viscosity of TiO_2 slurries with different salts as additive. The slurry viscosity was increased by addition of chloride salts into the slurry. Furthermore, slurries prepared with divalent salts and 0.2 M NaCl showed similar maximal viscosities. Slurries with 0.1 M KCl and 0.1 M NaCl showed similar maximal viscosity as well, but decreased compared to divalent salt slurries.

Table 1
Chemical surface composition of the anatase powder used in this study.

Element	O	Ti	C	Al	P	Na
at%	58.2	21.5	13.7	3.1	2.1	1.5

Table 1 shows that the chemical composition of the used TiO_2 powder. Apart from titanium and oxygen, oxidised aluminium impurities were also found in the powder sample. In addition to adsorbed hydrocarbon surface contamination, low concentration of phosphorus and sodium (≤ 2 at%) were also detected on the surface of the TiO_2 particles. Phosphorus is present on the surface as phosphates, which may be dissolved from the surface in to the TiO_2 suspension, particularly at high TiO_2 particle concentrations. However, no precipitation of phosphate salts with low solubility was observed in slurry supernatants when the used mono- and divalent chloride salts were added into the slurry supernatants to obtain final salt cation concentration of 0.1 M.

3.2. Influence of chloride salts on scaffold properties

Table 2 includes the most important structural characteristics of all

Table 2
Scaffold parameters pore size, strut thickness and porosity calculated with microCT and average grain size calculated with ImageJ.

	Total porosity %	Pore size µm	Strut thickness µm	Strut thickness distribution peak (48 µm) %	Average grain size µm
Control	89 ± 1	451 ± 78	67 ± 10	17 ± 4	16.8 ± 6.3
0.1 M KCl	91 ± 1	441 ± 10	62 ± 6	20 ± 3	16.6 ± 7.1
0.1 M NaCl	93 ± 1	480 ± 3	60 ± 6	22 ± 4	17.5 ± 7.4
0.2 M NaCl	89 ± 1	391 ± 17*	62 ± 7	20 ± 3	13.6 ± 4.6
0.1 M $CaCl_2$	90 ± 2	422 ± 14	62 ± 11	26 ± 6	48.0 ± 33.0**
0.1 M $MgCl_2$	90 ± 1	422 ± 30	64 ± 7	21 ± 4	50.5 ± 28.5**
0.1 M $SrCl_2$	89 ± 2	425 ± 13	67 ± 8	20 ± 4	60.2 ± 34.5**

* $p < 0.05$, $n = 4$.
** $p < 0.001$, $n = 34$.

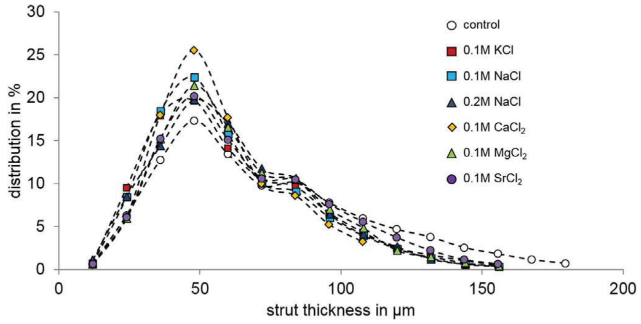

Fig. 4. Strut size distribution of all fabricated scaffolds. All salted scaffolds showed a higher and more concentrated peak at 48 µm, while 0.1 M $CaCl_2$ scaffolds showed the highest distribution (26 ± 6%) at 48 µm.

fabricated scaffolds. The pore size of scaffolds produced using slurries containing divalent cations was similar to the control scaffolds, while 0.1 M KCl and NaCl showed larger pores. 0.2 M NaCl scaffolds showed significantly smaller pore size compared to the control scaffolds. The porosity for all scaffolds was higher than 89% and the strut thickness of all scaffolds prepared with salt was decreased apart from $SrCl_2$ scaffolds which had the same strut thickness as the control scaffolds without salt. The strut thickness distribution shows a narrow distribution of $CaCl_2$ scaffolds in one peak at 48 µm instead of a wide range of strut thicknesses (Fig. 4), which is a result of a more homogenous sponge replication combined with less blocked pores. The strut thickness distribution peak is for all scaffolds with salt increased and 0.1 M $CaCl_2$ scaffolds showed the highest peak with 26%. The scaffolds could be divided into two different groups based on their compressive strength (Fig. 5). The monovalent scaffolds (0.1 M NaCl and KCl) showed a similar compressive strength compared to the control scaffolds. The second group consisting of scaffolds prepared with divalent salts (0.1 M $CaCl_2$, 0.1 M $MgCl_2$ and 0.1 M $SrCl_2$) showed increased compressive strength, whereby 0.1 M $CaCl_2$ scaffolds a significant 54.7% increase in compressive strength. 0.2 M NaCl scaffolds showed similar scaffold properties in comparison to the divalent scaffolds.

The change of strut shape in TiO_2 scaffolds by adding different salts to the slurry is shown in Fig. 6. The control scaffolds showed struts with the hollow structure typical of ceramic foams produced by polymer sponge replication or a characteristic V-shaped struts resulting from inward collapse of one of the walls of the hollow struts during sintering. Furthermore, longitudinal cracks along the strut edges were observed which contributed to the low compressive strength. Scaffolds produced with 0.1 M NaCl and KCl showed denser struts compared to the control scaffolds but cavities and cracks along the struts were still observed. Denser struts combined with cavities and cracks did not deviate significantly in compressive strength compared to the control scaffolds. The divalent and 0.2 M NaCl scaffolds showed even more dense struts without cavities and reduced cracks, leading to a higher compressive strength compared to the control and monovalent scaffolds. Furthermore, $CaCl_2$ and $SrCl_2$ scaffolds showed a large amount of Ca^{2+} and Sr^{2+} concentrated in the grain boundaries, while in all other scaffolds the additional ions showed a homogenous distribution in grains and grain boundaries (Fig. 6).

Regardless of concentration, monovalent salts did not show any effect on the grain size in sintered TiO_2 ceramic scaffolds. The average grain size of NaCl and KCl scaffolds is similar to the control scaffolds. The influence of divalent salts on grain growth is shown in Fig. 7A2-D2 and Table 2. $CaCl_2$ and $MgCl_2$ showed similar average grain size, which was more than three times larger compared to the control scaffolds. $SrCl_2$ scaffolds showed even larger grains in average which were observed to be more than four times larger than control scaffolds without salt. The increase in grain size for all scaffold groups with divalent salt was found statistically significant compared to the control without salt.

The influence of divalent salts on grain size during the polymer burn-out process at 1100 °C is shown in Fig. 7A1-D1. $MgCl_2$ did not show an effect on grain size and resulted in similar grains compared to

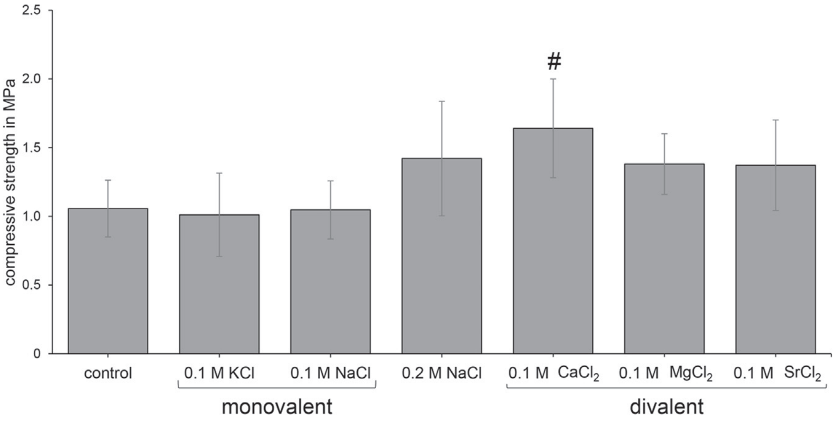

Fig. 5. Compressive strength of all fabricated scaffolds. 0.1 M $CaCl_2$ scaffold showed a statistically significant increased strength compared to the control scaffolds (# $p < 0.01$). $n = 10$.

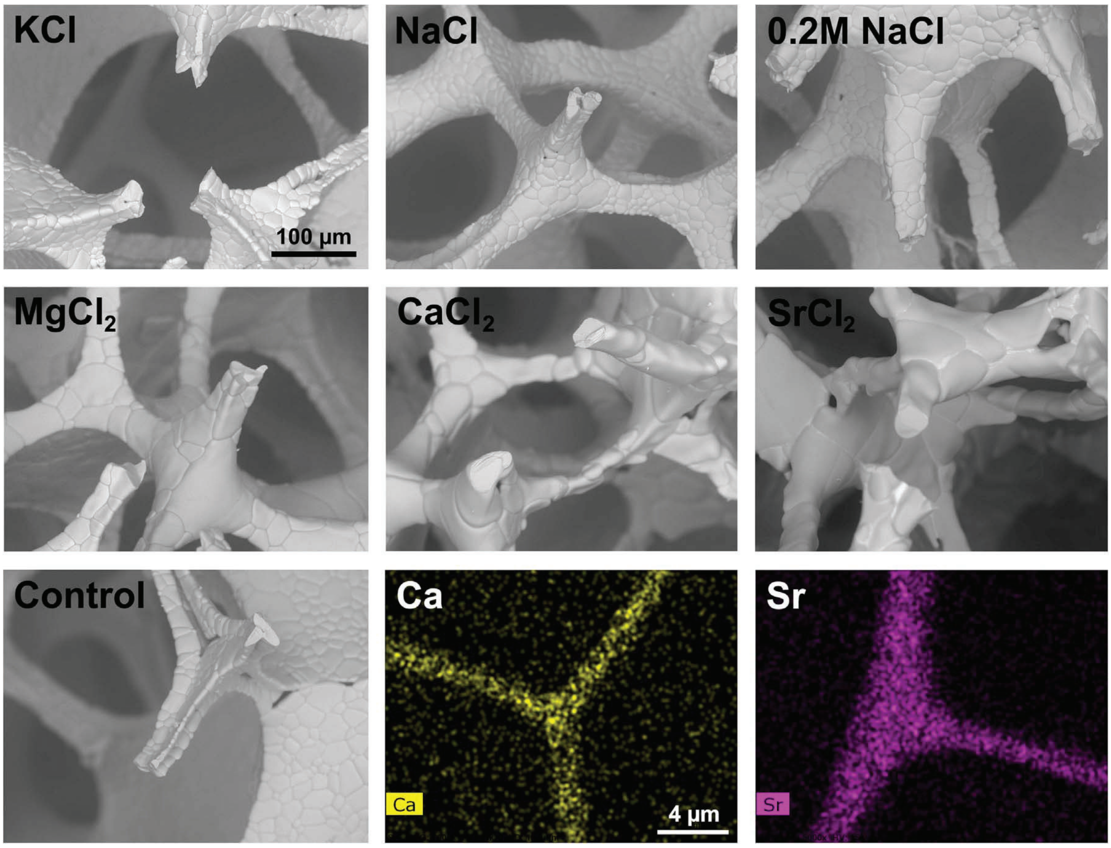

Fig. 6. Effect of different salts on the strut architecture of TiO_2 scaffolds. Scaffold struts of control scaffolds showed thin struts with a typical V-shape, which causes low compressive strength. Scaffolds fabricated with divalent salts and 0.2 M NaCl showed closed struts and especially $CaCl_2$ and $SrCl_2$ round struts without a typical V-shape.

the control scaffolds. $CaCl_2$ scaffolds showed slightly larger grains after the burn out process. $SrCl_2$ scaffolds showed larger TiO_2 grains compared to the control scaffolds and phases with a high concentration of Sr^{2+} were observed as the bright spots seen in Fig. 7D1.

4. Discussion

This study shows that the maximum viscosity of TiO_2 slurries can be increased by adding different chloride salts to the suspension. Slurries prepared with 0.1 M NaCl and KCl slurries showed similar rheological behaviour with an increased maximum viscosity compared to slurries without salts. The development of both viscosities as a function of shear rate was similar although the influence on the ζ potential was different. According to the DLVO theory the ζ potential can be measured to determine the repulsive forces between particles in a suspension, and due to this, the stability of the particle suspension can be evaluated [17,18].

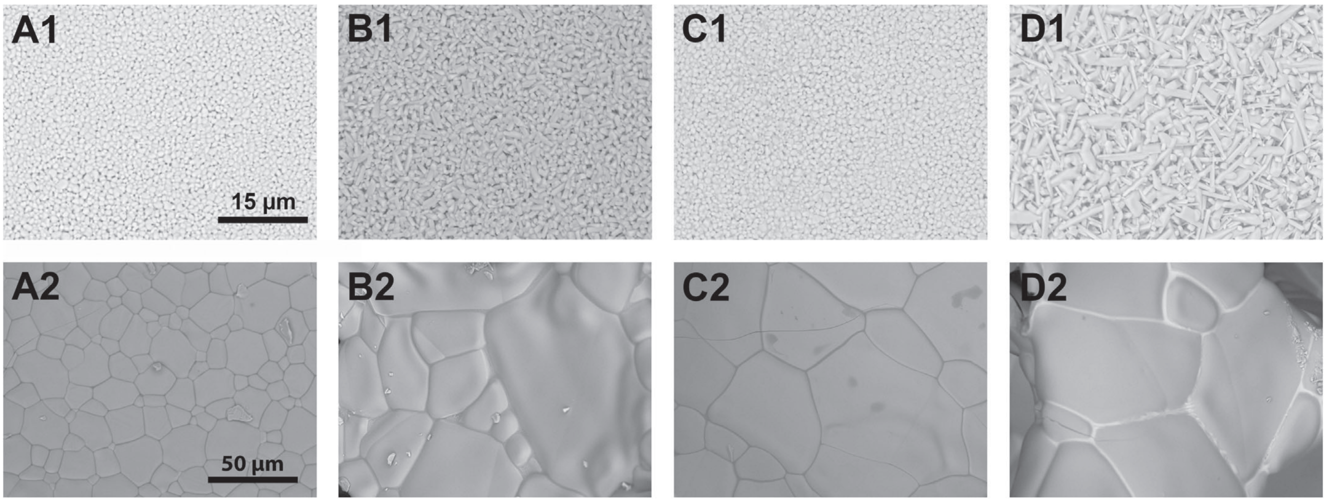

Fig. 7. Grain size after burn out (1) and after sintering (2) for the control scaffolds (A), 0.1 M $CaCl_2$ (B), 0.1 M $MgCl_2$ (C) and 0.1 M $SrCl_2$ scaffolds (D). $CaCl_2$ and $MgCl_2$ did not show a difference in grain size before sintering compared to control scaffolds, while $SrCl_2$ seems to effect the grain size before sintering. All scaffolds showed increased grain size after sintering in comparison to control scaffolds without salt addition.

Previous studies have shown that electrolytes compress the electric double layer and therefore decrease the ζ potential [17,19–21]. The ζ potential measurement of NaCl and KCl showed that the ζ potential of 0.1 M NaCl and 0.1 M KCl samples is similar. Hence, the influence of both 1-1 electrolytes on the electric double layer is similar and resulted in a higher slurry viscosity with a similar maximum viscosity compared to the control slurry. Furthermore, the similar influence of 0.1 M NaCl and KCl on the ζ potential is confirmed by showing the same decreased absolute value for the slurry measurements. The ζ potential is depending on the ions-to-TiO_2 particle ratio [21]. The TiO_2 particle concentration was markedly higher in the cloudy supernantant sample compared to LC measurements, although the exact concentration is unkown. This leads to the assumption that NaCl and KCl at the concentration of 0.1 M decreased the ζ potential in TiO_2 slurries with the same amount.

The same ζ potential was measured for a higher concentration of 0.2 M NaCl for the slurry measurement. But the slurry viscosity was approximately three times higher for 0.2 M NaCl slurries in comparison to 0.1 M NaCl and KCl slurries. According to the DLVO theory, an increased electrolyte concentration results in a decreased ζ potential and interaction energy which leads to agglomerations between single particles [15,19]. The slurries with 0.2 M NaCl had similar viscosity as the slurries with divalent salts as additive. All divalent salts acted as non-inert electrolytes, what was confirmed due to an IEP shift. This shift was not observed for the higher NaCl (0.2 M) concentration. The IEP shift occurs because of a specific adsorption of ions on TiO_2 particles [17,19,22]. This specific adsorption seemed to be present for divalent salt samples, because an IEP shift was observed. But the ζ potential measurement of divalent salt slurries showed that for a higher powder concentration the influence of divalent salts is similar to the monovalent salts despite the higher Cl^- concentration. This measurement showed that, by increasing the powder concentration, the influence of the ions on the ζ potential is not marked enough to explain the notable difference in viscosity. The $SrCl_2$ and $CaCl_2$ slurries were unstable and aggregated at a work pH 2.2, which can not be explained simply by the decreased ζ potential. Velamakanni et al. described in 1990 that the DLVO theory is not fully consistent for coagulated slurries, especially in the presence of excess salt [23]. The net energy according to the DLVO theory is not only defined due to the ζ potential, it is depending on ionic strength as well [24]. By using extreme high ionic strength, the net energy is decreased and the ζ potential shows that the electrolyte is not sufficient to stabilize the dispersion. The coagulated $CaCl_2$ and $SrCl_2$ slurries at pH 2.2 showed this effect, but the explanation of the stability of high concentrated ceramic slurries has to include the discussion of a third force as well.

In 1985, Israelachvili suggested a third force which acts as a repulsive hydration force at very small distances (< 5 nm) [25]. This additional force explains the interparticle forces in a highly concentrated suspension in the presence of salt. The hydration layer is formed at low pH, when hydrated anions interact with the positively charged TiO_2 surface [23]. The different ζ potential measurements combined with the viscosity measurement in this study agree with this theory. The viscosity increases in the presence of salt depending on the anion concentration. Hence, 0.2 M NaCl slurries showed the same viscosity as the 0.1 M divalent salt slurries and 0.1 M NaCl and KCl slurries showed a decreased maximum viscosity. Both ζ potential measurements showed that this potential is not the main influence on the stability of highly concentrated suspensions although the ζ potential is decreased for all slurries. Furthermore, the slurry measurement revealed the strong influence of the particle concentration on the ζ potential as higher ζ potential values were measured for the more concentrated samples. This confirmed that the ζ potential measurement with a low particle concentration of 25 mg/l cannot fully explain the interparticle forces in high concentrated suspensions, but gives valuable information on the general influence and adsorption of different ions on TiO_2 particle surfaces.

The measurement of ζ potential and viscosity showed that adding salt is an efficient way to increase the viscosity of concentrated TiO_2 suspensions. The slurries showed a strong shear thinning effect because of coagulation and hydration force at low interparticle distances [15,23]. The stability over time underlines that the particles are coagulated and not agglomerated. A coagulated suspension is defined as a suspension to which salt is added, the attractive forces are dominated and a network of non-touching particles are present [15]. Therefore, the highly concentrated slurries are defined as coagulated and not agglomerated because of the high ionic strength and low ζ potential. An increase in powder concentration resulted in agglomerated slurries. This effect was not observed for the used slurries in this study and shows once again that the used powder concentration leads to a stable slurry without agglomerations. Although chemical analysis revealed the presence of low concentration of phosphate impurities on the TiO_2 particle surface (Table 1), the low processing pH used for the slurry preparation (pH < 3) prevented any precipitation of insoluble calcium or strontium phosphate salts due to potential release of soluble phosphate from the particle surface. Therefore, the observed influence on the rheological properties of the prepared slurries cannot be explained by formation of impurity particles in the presence of impurity anions. This underlines that the investigated influences occur due to the additional chloride salt ions in to the TiO_2 slurry. But the low IEP of the used anatase TiO_2 powder can be explained due to the high amount of soluble phosphates present on the particle surface.

4.1. *Influence of ions on scaffold properties*

In this study, different scaffold properties of monovalent and divalent scaffolds were observed. This shows that the viscosity, which is lower for monovalent slurries compared to divalent slurries, has a direct influence on the main scaffold properties. Monovalent scaffolds showed similar compressive strength compared to control scaffolds. The strut thickness of monovalent scaffolds was slightly decreased. The strut thickness distribution showed a more concentrated distribution combined with a high peak, which is an indication for a more uniform scaffold structure compared to control scaffolds. This assumption was also confirmed by the higher porosity. In relation to control scaffolds, the strut architecture of monovalent scaffolds showed slightly denser struts with a less pronounced V-shape due to a more viscous TiO_2 slurry. All in all, the change in scaffold properties of monovalent scaffolds are not strong enough. The compressive strength of monovalent scaffolds is similar to the control scaffolds because of similar structural properties. Furthermore, cracks along the struts are still observed for all monovalent scaffolds and control scaffolds.

On the other hand, divalent scaffolds showed improved compressive strength with similar porosity values compared to control scaffolds, because of denser struts combined with a closed strut architecture. The strut thickness distribution showed more homogenous strut size with a more concentrated distribution and high peak at 48 μm (Fig. 4). The strut architecture exhibit more material, which is the result of a better polymer foam coating during the replication method.

One reason for the more uniform coating of the polymer foam is the higher viscosity of all divalent slurries. The influence of slurry viscosity on scaffold properties is shown by the comparison of divalent slurries and scaffolds with the 0.2 M NaCl slurry and scaffolds. This underlines the previous discussed important influence of the amount of Cl ions on slurry rheology and scaffold properties. The strut architecture of $MgCl_2$ and 02 M NaCl scaffolds is similar and exhibited a slightly V-shaped strut morphology. Due to more material on the struts, the densification of TiO_2 led to a cavity free architecture, resulting in an improved compressive strength. However, a more important reason for this structural densification was the influence of the different salts on the sintering behaviour of TiO_2, which was particularly pronounced for $SrCl_2$ and $CaCl_2$. With round and dense struts without a V-shape the strut architecture of $CaCl_2$ and $SrCl_2$ scaffolds shows a different morphology than all other scaffolds, especially when compared to the control scaffolds (Fig. 6). The comparison of divalent scaffolds with scaffolds from previous studies shows the importance of dense struts without a V-shape to improve the compressive strength. Tiainen et al. produced TiO_2 scaffolds using a highly viscous slurry with a maximum viscosity higher than 30 Pas due to a high Na^+ and Cl^- concentration that results from a washing procedure used to remove surface-bound contaminations from the TiO_2 particle [8,11]. But these scaffolds showed lower compressive strength compared to all scaffolds in this study with the same amount of powder in the slurry and a similar porosity values of the scaffolds [8]. The comparison of the strut architecture shows that despite a higher slurry viscosity, the strut architecture still evince flaws which caused the low compressive strength. This strengthens the assumption that viscosity is just one influence on scaffold compressive strength. Although a higher slurry viscosity showed to improve the scaffold properties in this study, the influence on ions during the sintering process and the densification of the material has an even stronger impact on the strut morphology and mechanical properties of the scaffolds.

Another confirmation for the importance of the influence of ions on scaffold properties is given by the larger grain size of divalent scaffolds compared to the control scaffolds. Novak et al. showed an improved compressive strength of tenfold by eliminating cracks and flaws in the scaffolds structure with PDLLA/Bioglass composite coating [26]. This connection proves once again that the compressive strength of a porous scaffold can be increased by decreasing the number of cracks and flaws in the scaffold struts. A theory for the increased compressive strength because of denser struts is that a liquid phase may be formed during the sintering process. Because of a more rapid grain boundary diffusion kinetics and high grain boundary mobility during a liquid phase, the grains are growing much faster and abnormal grain growth is present in the scaffolds with divalent salt [27,28]. As shown in Figs. 5 and 6, the faster grain growth of divalent salt scaffolds led to more dense struts and finally to higher compressive strength. But the comparison of grain size after the burn-out process at 1100 °C shows as well that the mechanism between $SrCl_2$ and the other two divalent salts is different. While $MgCl_2$ and $CaCl_2$ scaffolds showed similar grain size to the control group before the high temperature sintering process, $SrCl_2$ showed increased grain size. Additionally, the observed Sr-rich spots led to the assumption that there is a reaction between Sr^{2+} and TiO_2 forming a new strontium rich phase already at temperature below 1500 °C.

Another effect in $CaCl_2$ and $SrCl_2$ scaffolds was observed in the grain boundary composition. While all other scaffolds showed a homogenous distribution of the additional ions in grains and grain boundaries, Sr^{2+} and Ca^{2+} seemed to affect the grain boundary composition. $CaCl_2$ and $SrCl_2$ scaffolds had an increased amount of Ca^{2+} and Sr^{2+} concentrated in grain boundaries. There is a solubility limit for cations with large ionic radius, such as Ca^{2+} and Sr^{2+}, in TiO_2 lattice. Excess cations are pushed out into the grain boundaries. The solubility of impurities in the lattice is depending on the charge and the ionic radius of the cations [29], which explains the different grain boundaries of Ca^{2+} and Sr^{2+} doped TiO_2 scaffolds compared to Mg^{2+}, Na^+ and K^+ doped one. This effect has also been reported for Al_2O_3 lattices [30].

5. Conclusion

This study showed that the viscosity of concentrated anatase TiO_2 slurries could be increased by adding mono- or divalent chloride salts into the slurry. The ζ potential measurement of the slurry showed that the force which prevents the agglomeration of particles in a suspension with short distances (< 5 µm) is the hydrations force. Due to a higher viscosity, scaffold properties can be improved as well. All scaffolds with salt showed denser struts morphology which results in high compressive strength. Because of these denser and rounder struts, the scaffolds showed a compressive strength up to 1.68 MPa. Furthermore, the activation energy for sintering is decreased by using $CaCl_2$ and $SrCl_2$ which leads to larger grains caused by higher grain boundary mobility. A new grain boundary composition appeared in $CaCl_2$ and $SrCl_2$ scaffolds, which showed a larger amount of Ca^{2+} and Sr^{2+}.

Funding

This work was supported by the Faculty of Dentistry, University Oslo.

References

[1] H. Haugen, J. Will, A. Köhler, U. Hopfner, J. Aigner, E. Wintermantel, Ceramic TiO_2-foams: characterisation of a potential scaffold, J. Eur. Ceram. Soc. 24 (2004) 661–668.
[2] H. Tiainen, J.C. Wohlfahrt, A. Verket, S.P. Lyngstadaas, H.J. Haugen, Bone formation in TiO_2 bone scaffolds in extraction sockets of minipigs, Acta Biomater. 8 (2012) 2384–2391.
[3] N. Tsukimura, N. Kojima, K. Kubo, W. Att, K. Takeuchi, Y. Kameyama, H. Maeda, T. Ogawa, The effect of superficial chemistry of titanium on osteoblastic function, J. Biomed. Mater. Res. Part A 84A (2008) 108–116.
[4] R. Cancedda, B. Dozin, P. Giannoni, R. Quarto, Tissue engineering and cell therapy of cartilage and bone, Matrix Biol. 22 (2003) 81–91.
[5] V. Karageorgiou, D. Kaplan, Porosity of 3D biomaterial scaffolds and osteogenesis, Biomaterials 26 (2005) 5474–5491.
[6] A. Verket, H. Tiainen, H.J. Haugen, S.P. Lyngstadaas, O. Nilsen, J.E. Reseland, Enhanced osteoblast differentiation on scaffolds coated with TiO_2 compared to SiO_2 and CaP coatings, Biointerphases 7 (2012) 36.
[7] D.R. Carter, W.C. Hayes, Bone compressive strength: the influence of density and strain rate, Science 194 (1976) 174–1176.
[8] H. Tiainen, S.P. Lyngstadaas, J.E. Ellingsen, H.J. Haugen, Ultra-porous titanium oxide scaffold with high compressive strength, J. Mater. Sci.: Mater. Med. 21 (2010) 2783–2792.
[9] I. Sabree, J.E. Gough, B. Derby, Mechanical properties of porous ceramic scaffolds: influence of internal dimensions, Ceram. Int. 41 (2015) 8425–8432.
[10] I. Narkevica, L. Stipniece, E. Jakobsons, I. Cakstina, J. Ozolins, Electrically active and 3D porous TiO_{2-x} ceramic scaffolds for bone tissue regeneration, J. Eur. Ceram. Soc. 37 (2017) 833–840.
[11] H. Tiainen, D. Wiedmer, H.J. Haugen, Processing of highly porous TiO_2 bone scaffolds with improved compressive strength, J. Eur. Ceram. Soc. 33 (2013) 15–24.
[12] C. Galassi, Processing of porous ceramics: piezoelectric materials, J. Eur. Ceram. Soc. 26 (2006) 2951–2958.
[13] J. Kolczyk, J. Zych, Rheological properties of ceramic slurries with colloidal binders used in the investment casting technology, Metalurgija 52 (2013) 55–58.
[14] M. Kosmulski, Introduction, Surface Charging and Points of Zero Charge, CRC Press, Boca Raton, FL, 2009, pp. 1–38.
[15] J. Davies, J.G.P. Binner, Coagulation of electrosterically dispersed concentrated alumina suspensions for paste production, J. Eur. Ceram. Soc. 20 (2000) 1555–1567.
[16] N. Casson, A Flow Equation for Pigment-oil Suspension of the Print Ing Ink Type: Conference of the British Society of Rheology, University College, Swansea, UK, Sept 1957, Pergamon Press, NewYork, 1959.
[17] J. Gustafsson, P. Mikkola, M. Jokinen, J.B. Rosenholm, The influence of pH and NaCl on the zeta potential and rheology of anatase dispersions, Colloids Surf. A: Physicochem. Eng. Asp. 175 (2000) 349–359.
[18] J.P. Friend, R.J. Hunter, Plastic flow behavior of coagulated suspensions treated as a repeptization phenomenon, J. Colloid Interface Sci. 37 (1971) 548–556.
[19] M. Kosmulski, J.B. Rosenholm, High ionic strength electrokinetics, Adv. Colloid Interface Sci. 112 (2004) 93–107.
[20] R. Hogg, T.W. Healy, D.W. Fuerstenau, Mutual coagulation of colloidal dispersions, Trans. Faraday Soc. 62 (1966) 1638–1651.
[21] M. Kosmulski, J.B. Rosenholm, Electroacoustic study of adsorption of ions on anatase and zirconia from very concentrated electrolytes, J. Phys. Chem. 100 (1996) 11681–11687.
[22] M. Kosmulski, J. Gustafsson, J.B. Rosenholm, Correlation between the zeta potential and rheological properties of anatase dispersions, J. Colloid Interface Sci. 209 (1999) 200–206.
[23] B.V. Velamakanni, J.C. Chang, F.F. Lange, D.S. Pearson, New method for efficient colloidal particle packing via modulation of repulsive lubricating hydration forces, Langmuir 6 (1990) 1323–1325.
[24] R.A. Terpstra, P. Pex, A.H. de Vries, Ceramic Processing, Springer, Great Britain, 1995.
[25] J.N. Israelachvili, Solvation, Structural, and Hydration Forces, Intermolecular and Surface Forces, Third edition, Academic Press, San Diego, 2011, pp. 341–380.
[26] S. Novak, J. Druce, Q.-Z. Chen, A.R. Boccaccini, TiO_2 foams with poly-(D, L-lactic acid)(PDLLA) and PDLLA/Bioglass® coatings for bone tissue engineering scaffolds, J. Mater. Sci. 44 (2009) 1442–1448.
[27] D.A.H. Hanaor, W. Xu, M. Ferry, C.C. Sorrell, Abnormal grain growth of rutile TiO_2 induced by $ZrSiO_4$, J. Cryst. Growth 359 (2012) 83–91.
[28] S.-H. Hong, D.-Y. Kim, Effect of liquid content on the abnormal grain growth of alumina, J. Am. Ceram. Soc. 84 (2001) 1597–1600.
[29] M. Schacht, N. Boukis, E. Dinjus, Corrosion of alumina ceramics in acidic aqueous solutions at high temperatures and pressures, J. Mater. Sci. 35 (2000) 6251–6258.
[30] L. Ćurković, M.F. Jelača, S. Kurajica, Corrosion behavior of alumina ceramics in aqueous HCl and H_2SO_4 solutions, Corros. Sci. 50 (2008) 872–878.

II

Journal of the European Ceramic Society 39 (2019) 1577–1585

Contents lists available at ScienceDirect

Journal of the European Ceramic Society

journal homepage: www.elsevier.com/locate/jeurceramsoc

Original Article

Grain boundary corrosion in TiO_2 bone scaffolds doped with group II cations

Anne Klemm[a], Manuel Gomez-Florit[b,c], Patricia Almeida Carvalho[d], Mattis Wachendörfer[a,e], Manuela E. Gomes[b,c], Håvard J. Haugen[a], Hanna Tiainen[a,*]

[a] University of Oslo, Department of Biomaterials, Institute of Clinical Dentistry, P.O. Box 1109 Blindern, 0317, Oslo, Norway
[b] 3B's Research Group, I3Bs – Research Institute on Biomaterials, Biodegradables and Biomimetics, University of Minho, Headquarters of the European Institute of Excellence on Tissue Engineering and Regenerative Medicine, AvePark, Parque de Ciência e Tecnologia, Zona Industrial da Gandra, 4805-017, Barco, Guimarães, Portugal
[c] ICVS/3B's–PT Government Associate Laboratory, Braga, Guimarães, Portugal
[d] SINTEF Materials and Chemistry, PB 124, Blindern, NO-0314, Oslo, Norway
[e] Helmholtz-Institute for Biomedical Engineering, Chair of Medical Engineering, RWTH Aachen University, Pauwelsstraße 20, 52074, Aachen, Germany

ARTICLE INFO

Keywords:
Doped TiO_2
Corrosion
Grain boundary
$SrTiO_3$
Osteogenic differentiation

ABSTRACT

A pH drop during the inflammatory phase during bone regeneration can cause corrosion in TiO_2 bone scaffolds and the loss of compressive strength. Corrosion as ion leaching and dissolution is confined to grain boundaries. Cationic doping of TiO_2 showed to increase the compressive strength but increased the amount of impurities in grain boundaries as well. Therefore, this study showed the different grain boundary formation for Ca, Sr and Mg doped scaffolds and their corrosion behavior. After corrosion, the amorphous phase in grain boundaries was dissolved in all doped scaffolds. Differences occurred due to the formation of an additional crystalline phase in Sr doped scaffolds. The presence of an amorphous and crystalline phase led to an inhomogeneous dissolution in grain boundaries and a significant decrease in compressive strength already after 4 h in contact with an acidic environment. Released ions did not show any cytotoxic effect on hASCs. Mg doped TiO_2 scaffolds led to significant increased osteogenic differentiation.

1. Introduction

The potential for highly porous TiO_2 scaffolds as bone scaffolds is well-known [1–3]. Due to a sufficient pore size, interconnectivity and large surface-to-volume ratio, these scaffolds allow cell ingrowth, vascularization and cell adhesion [2,3]. Furthermore, TiO_2 scaffolds produced by the polymer sponge replication method combine high porosity with high compressive strength [4]. This property of bone scaffolds is crucial for the support of bone cells during bone regeneration process and should be stable during the inflammatory phase.

To reach a compressive strength similar to that of natural bone (2–12 MPa), different strategies have been proposed to increase the strength of TiO_2 scaffolds. One possible strategy is the so-called double coating, where the final sintered scaffolds are coated with a low viscous slurry to densify the strut architecture. Using this strategy, the compressive strength of TiO_2 scaffolds can be increased from approx. 1 MPa up to 1.6 MPa for a porosity of approx. 90% [4]. We have also shown that cationic doping of TiO_2 slurries leads to a similar significant increase in compressive strength. The advantage of this strategy is that no additional step, including low viscous slurry and sintering procedure, is necessary. By adding different ions to the slurry, two mechanisms lead to higher compressive strength. First, the slurry viscosity is increased, which was shown to affect the final strength. Second, the sintering behavior of TiO_2 is changed and the presence of a liquid phase during sintering was proposed as reason for the improved strut densification and a high compressive strength of 1.64 MPa [5].

Corrosion resistance of the TiO2 scaffolds is an important property to ensure a high compressive strength during inflammatory phase. During inflammatory phase, a large amount of macrophages are present which can acidify their microenvironment to a pH level of 3.6–3.7 [6]. Ceramics in general show corrosion in acidic environments due to ion leaching and dissolution [7]. These effects tend to concentrate on areas where crystal lattice defects are dominant, such as grain boundaries. Müller et al. found released Si and Al from TiO_2 grain boundaries after storing the TiO_2 bone scaffolds for 8 weeks in 1 mM HCl solution (pH3). Furthermore, the study showed significant decrease in compressive strength after corrosion [8].

In the present study, TiO_2 scaffolds doped with divalent Ca, Sr and Mg cations showed a different and new impurity rich formation in grain boundaries. Considering that corrosion is likely to occur in these areas, the new formation has to be investigated with focus on corrosion behavior. TEM was used to investigate the grain boundary formation in

---

[*] Corresponding author.
E-mail address: Hanna.tiainen@odont.uio.no (H. Tiainen).

https://doi.org/10.1016/j.jeurceramsoc.2018.12.055
Received 24 October 2018; Received in revised form 16 December 2018; Accepted 22 December 2018

Ca, Sr and Mg doped TiO_2 scaffolds. Additionally, a short corrosion test showed the corrosion resistance and amorphous or crystalline nature of phases in grain boundaries. Biocompatibility of these doped scaffolds was investigated by LDH, real-time PCR and live-dead staining which showed the effect of released ions on cell differentiation.

2. Material and methods

2.1. Scaffold fabrication

The polymer foam replication method was used to fabricate TiO_2 scaffolds as previously described [5]. The slurry was prepared by adding 65 g of anatase powder (HOMBITAN FF-Pharma, Sachtleben Chemie GmbH, Duisburg, Germany) into 25 ml of divalent salt solutions. For investigating the scaffold properties depending on salt concentration, the scaffolds were fabricated with increasing salt concentrations up to 0.1 M in 0.02 M steps using the divalent salts $CaCl_2$, $MgCl_2$ and $SrCl_2$ dissolved in deionised water (dH_2O). The slurry was adjusted to a work pH 1.5–1.7 by adding 1 M HCl and was stirred at 5000 rpm for 2.5 h at a temperature of 15–17 °C (Dispermat Ca-40, VMA-Gertzmann GmbH, Reichshof, Germany).

After coating the polymer foams (60 pores per inch, diameter 10 mm, height 10 mm, Bulbern S, Eurofoam GmbH, Wiesbaden, Germany) with the different slurries, excess slurry was squeezed out and the samples dried for 24 h at room temperature. Burn out of the polymer was performed at 1100 °C for 5 h (heating rate of 1 K/min) and sintering at 1500 °C for 20 h (heating rate 3 K/min) (HTC-08/16, Nabertherm GmbH, Lilienthal, Germany).

2.2. Corrosion test

Long-term corrosion test was performed for the control group without salt and 0.1 M $CaCl_2$, $MgCl_2$ and $SrCl_2$ scaffolds. The scaffolds were stored in polypropylene tubes for 2, 4 and 8 weeks in dH_2O and 1 mM HCl (pH3) solution at 37 °C. The short-term test was performed for scaffolds fabricated with different salt concentrations in 1 mM HCl solution at 37 °C for 4 h, 24 h and 7 d. After storing scaffolds in HCl solution, the scaffolds were rinsed with dH_2O and dried for 24 h at 37 °C.

2.3. Atomic absorption spectroscopy (AAS)

To measure the amount of released ions due to corrosion, samples were prepared in the same way as for the corrosion test. After 4 h, 1 d, 3 d and 7 d, the acidic solutions were filtered using a 0.2 µm PES filter. Ca and Mg samples were mixed with $LaCl_2$ (100:1). The amount of Ca, Mg and Sr was measured using an atomic absorption spectroscope (Perkin Elmer AANALYST 400, PerkinElmer, Massachusetts, USA). Three independent samples were measured two times and the average ± standard deviation is shown.

2.4. Compressive strength

Compressive strength of all fabricated scaffolds (uncorroded and corroded) were measured by using an uniaxial mechanical testing machine (Zwick/Roell Z2.5; Zwick GmbH & Co. KG, Ulm, Germany). After reaching the preload of 0.5 N, the scaffolds were compressed along their long axis (1 kN load cell) with a testing speed of 100 mm/min until failure, which is defined as 15% of the highest measured peak. The compressive strength on the basis of scaffold diameter and maximum force until failure was calculated with the software Test Expert II.

2.5. Scanning electron microscopy (SEM) and energy dispersive X-ray spectroscopy (EDX)

For the visual control of grain boundary corrosion, SEM (TM3030, Hitachi High-Technologies Europe GmbH, Krefeld, Germany) and EDX (Quantax 70, Bruker, Billerica, USA) were used. Scaffolds (n = 3) were mounted on aluminium stubs with conductive carbon tape. Images were taken with backscattered electrons mode and at 15 kV accelerating voltage. Scaffolds used for cell studies were washed with PBS and cells were fixed with 2.5% glutaraldehyde and stored for 1 h at 4 °C. After washing again with PBS, cells were dehydrated with increasing ethanol solutions (50, 70, 90 and 100%). After immersing samples three times with HDMS and drying overnight, the SEM (JSM-6010 LV, JEOL, Japan) was operated at 15 kV.

2.6. Focused ion beam (FIB) and transmission electron microscopy (TEM)

TEM samples were prepared by FIB using a JIB-4500 MultiBeam SEM-FIB (JOEL, USA). Scaffolds were embedded in epoxy resin (Poxy Pak™ Epoxy, Ted Pella, Inc., Sweden) mixed with 50 wt% carbon powder (PELCO® Carbon (Graphite) Powder, Ted Pella, Inc., Sweden) to mitigate charging effects. Samples were grinded and then coated with 7 nm thick platinum coating. The grain boundary formation was investigated using a Titan G2 60–300 microscope (FEI Company, USA). Three different selected area diffraction (SAD) patterns were recorded and the crystal structure was determined using JEMS (JEMS-SAAS, Switzerland) and VESTA (JP-Minerals, Japan).

2.7. Human adipose stem cells (hASC) culture

hASCs were isolated from lipoaspirate samples. Samples were obtained from the abdominal region of the patients undergoing plastic surgery, under the scope of previously established protocols with Hospital da Prelada (Porto, Portugal) with the approval of the University of Minho Ethics Committee.

Scaffolds were placed in non-adherent 48 well plates. 3×10^5 cells (hASCs) in 800 µl αMEM media were added against the well wall to each sample. After 3 h shaking the scaffolds at 37 °C, the scaffolds were moved to new well plates and 500 µl fresh αMEM media without cells was added. The used αMEM was supplemented with sodium bicarbonate, 10% fetal bovine serum and 1% antibiotics. The cells were cultured for 14 days at 37 °C with 5% CO_2 and the media was changed three times per week.

2.8. Cell viability

Cell viability by determination of lactate dehydrogenase (LDH) activity in cell culture medium was measured using the manufacturer's protocol (Pierce LDH Cytotoxicity Assay Kit, Thermo scientific, USA). After one and three days, 50 µl cell culture was collected. The absorbance was measured at 490 nm and the background at 680 nm was subtracted. Cytotoxicity is calculated as a percentage from total cell death. For each time point the maximum LDH activity was measured from cells cultured in well plates. Cells were lysed with specific buffer from the kit. Scaffolds without salt were used to measure the spontaneous LDH activity. The final %Cytotoxicity was calculated by

$$\%Cytotoxicity = \frac{[Compound - treated \quad LDH \quad activity] - [Spontaneous \quad LDH \quad activity]}{[Maximum \quad LDH \quad activity] - [Spontaneous \quad LDH \quad activity]} * (100)$$

Live/dead cell staining was used to determine viability of the adherent cells. The cells were first washed with PBS and then stained using calcein AM (1:500) and propidium iodide (PI; 1:1000) diluted in PBS. After 30 min, protected from light and incubated at RT, samples were washed with PBS and observed using confocal microscopy.

2.9. Real-time PCR

After 14 days of cell culture, total RNA was isolated using Ribozol (Amresco, Solon, OH, USA), according to the manufacturer's protocol.

Table 1
Primer sequences used for real-time PCR analysis.

Gene	Primer sequence	
Glyceraldehyde-3-phosphate dehydrogenase (GAPDH)	hGAPDH-F	GGGAGCCAAAAGGGTCATCA
	hGAPDH-R	GCATGGACTGTGGTCATGAGT
β-actin	hBActin-F	CTGGAACGGTGAAGGTGACA
	hBActin-R	AAGGGACTTCCTGTAACAA
Collagen I α1 (COL1)	hCOL1A1-F	CCCCAGCCACAAAGAGTCTAC
	hCOL1A1-R	TTGGTGGGATGTCTTCGTCT
Alkaline phosphatase (ALP)	hALP-F	GAAGGAAAAGCCAAGCAGGC
	hALP-R	GGGGGCCAGACCAAAGATAG
Runt related transcription factor 2 (RUNX2)	hRUNX2-F	TTCCAGACCAGCAGCACTC
	hRUNX2-R	CAGCGTCAACACCATCATTC

Total RNA was quantified at 260 nm using a nanodrop spectrophotometer (Thermo Scientific, Wilmington, DE, USA). The same amount of RNA (1 µg) was reverse transcribed to cDNA according to the protocol of the supplier (qScript cDNA Synthesis Kit, Quanta Biosciences). Aliquots of diluted cDNA sample were used for the later real-time PCR (Realplex, Eppendorf, Germany) reactions for two reference genes and target genes (see Table 1). Each reaction contained 7 µl of master mix (Perfecta SYBR Green FastMix, Quanta Biosciences), the sense and the antisense specific primers (20 µM) and cDNA sample (3 µl) in a final volume of 10 µl. The amplification program consisted of a pre-incubation step for denaturation of the template cDNA (2 min 95 °C), followed by 40 cycles consisting of a denaturation step (5 s 95 °C), an annealing step (15 s 60 °C) and an extension step (20 s 72 °C). After each cycle, fluorescence was measured at 72 °C A negative control without cDNA template was run in each assay.

All samples were normalized by the geometric mean of the expression levels of β-actin and GAPDH and fold changes were related to the control group using the following equation:

$$ratio = \frac{(E_{target})^{\Delta CP_{target}(control-sample)}}{(E_{ref})^{\Delta CP_{ref}(control-sample)}}$$

adapted from [9], where CP is the crossing point of the reaction amplification curve and E is the efficiency from the given slopes using serial dilutions. Stability of reference genes was calculated using a statistical tool (BestKeeper software, Technical University of Munich, Weihenstephan, Germany) [10].

2.10. Statistics

Compressive strength results are shown as mean ± standard deviation. Statistical analysis was performed using one-way analysis of variance (ANOVA) and pairwise multiple comparison by using Holm-Sidak method. If the normality (Shapiro-Wilk) or equal variance (Brown-Forsythe) test failed, Kruskal-Wallis one way analysis of variance on ranks was performed followed by pairwise comparison using Tukey Test. Cell results are shown as mean ± standard deviation of the mean. Statistic was performed using paired *t*-test and normality test using Shapiro-Wilk.

3. Results and discussion

3.1. Grain boundary corrosion and its effect on compressive strength

We have previously shown that cationic doping leads to a significant increase in compressive strength and the formation of a distinct grain boundary phase rich in the dopant ions in porous TiO_2 bone scaffolds [5]. Other studies have shown, that an acidic environment, which may occur for example during the inflammatory phase of bone healing, causes corrosion confined to grain boundaries [11,12]. Ceramics corrode via ion leaching and dissolution, which leads to a release of impurity ions from the grain boundaries. Additionally, corrosion in grain boundaries results in a significant decrease in compressive strength [8]. Considering the new grain boundary formation with a high concentrations of impurity ions at grain boundaries, the corrosion behavior of cation doped TiO_2 scaffolds was investigated in this study.

Ca and Sr doped scaffolds did not show any corrosion or change in compressive strength when stored in dH_2O (Figs. 1 and 2). The compressive strength was stable over 8 weeks and grain boundaries did not show any dissolutions. However, when Ca and Sr scaffolds were stored in an acidic environment, grain boundary corrosion was present. These groups corroded via ion leaching and dissolution, which resulted in a significant decrease in compressive strength. No further change in grain boundary dissolution or compressive strength was observed after two weeks, when stored in the same solution. This shows that grain boundary corrosion occurred already within the first two weeks. Although the change in the compressive strength caused by the corrosion was similar for Ca and Sr doped scaffolds, the remaining grain boundaries, and therefore, the grain boundary morphology were different. While Ca doped scaffolds showed corrosion resistant lamellae in corroded grain boundaries, Sr doped scaffolds exhibited an uneven corrosion resistant layer. To explain both of these mechanisms occuring in the doped grain boundaries, TEM analysis was performed and the results are shown in Fig. 3. Ca doped scaffolds showed an amorphous phase rich in Ca, Al and Si. The observed Al and Si in the grain boundary phase are considered to originate from the sintering environment as previously discussed by Müller et al. [8]. Additionally, TiO_2 crystals were found in grain boundary regions with direct contact to grains, indicating that corrosion resistant TiO_2 lamellar structures were forming in the grain boundaries of the Ca doped scaffolds. The amorphous phase consisting of Ca, Si and Al in between these lamellae was dissolved when stored in acidic solution. This ion leaching and

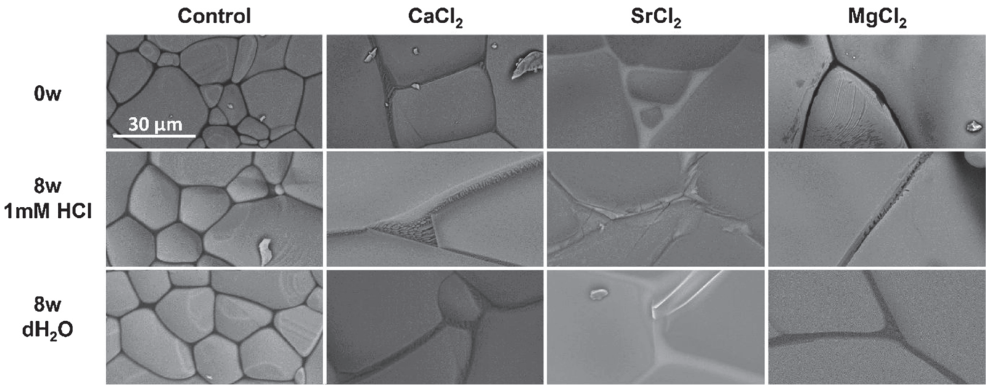

Fig. 1. Grain boundaries of uncorroded (0 w) and corroded (8 w–1 mM HCl and dH_2O) scaffolds as observed by SEM. Corrosion was concentrated in grain boundaries after storing in 1 mM HCl solution.

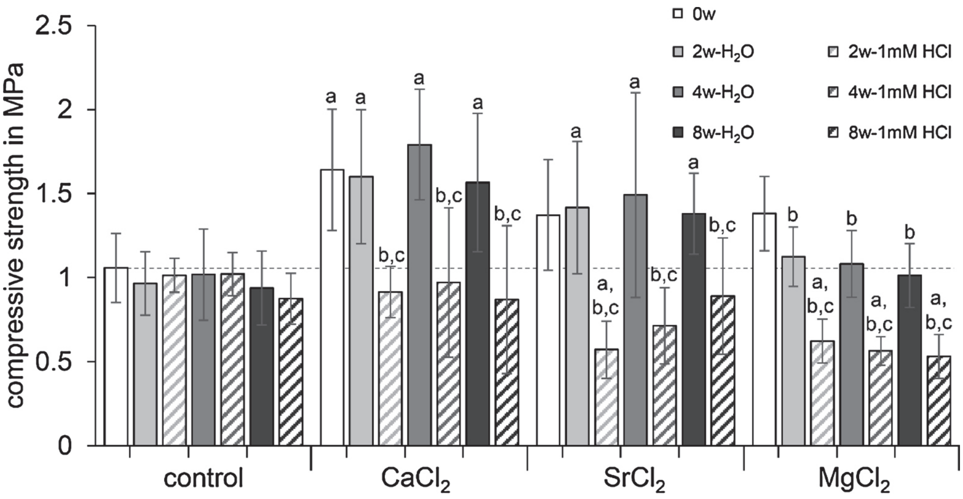

Fig. 2. Compressive strength of long-term treated (2, 4 and 8 weeks in dH_2O and 1 mM HCl) scaffolds doped with 0.1 M $CaCl_2$, $SrCl_2$ and $MgCl_2$. Significant difference ($p < 0.001$, $n = 10$) is indicated in comparison to control scaffolds with the same treatment and same time point (a), to uncorroded scaffolds with same doping (b) and to dH_2O groups at the same time point (c).

dissolution resulted in the decreased compressive strength. Formation of a new crystalline grain boundary phase was detected in the Sr doped scaffolds (Fig. 3C–E). $SrTiO_3$ crystals and an amorphous phase rich in Al and Si were observed in Sr doped grain boundaries. Considering the SEM images presented in Fig. 1, the ion leaching and dissolution was concentrated in the amorphous phase, causing the significant reduction in compressive strength, while the more corrosion resistant $SrTiO_3$ crystals remained intact after storage in acidic solution.

Mg doped TiO_2 scaffolds showed a different corrosion behavior compared to Ca and Sr doped scaffolds. As shown in Fig. 1, the corrosion was confined to the Mg rich spots within the grain boundary, resulting in small and localised holes in the grain boundary phase rather the more homogeneous dissolution of an amorphous grain boundary phase seen in Ca and Sr doped scaffolds. The different observed corrosion mechanism compared to the Ca and Sr doped scaffolds was found to influence the compressive strength in a different way as well. More importantly, a significant decrease in compressive strength already occurred after storing these scaffolds in dH_2O. This reduction in strength was even more pronounced following exposure to 1 mM HCl (Fig. 2).

The different corrosion behavior in Mg doped scaffolds was confirmed by measuring the released ions after the corrosion test (Fig. 4). While the amount of released Ca and Sr ions did not increase after three days, the amount of released Mg was significantly increased after three days. This indicates that Mg doped grain boundaries exhibit a new phase, which is more corrosion resistant compared to Ca and Sr doped grain boundary phases, resulting in a slower and more continous release of Mg ions. A similar result was published by Gavrilov et al., who

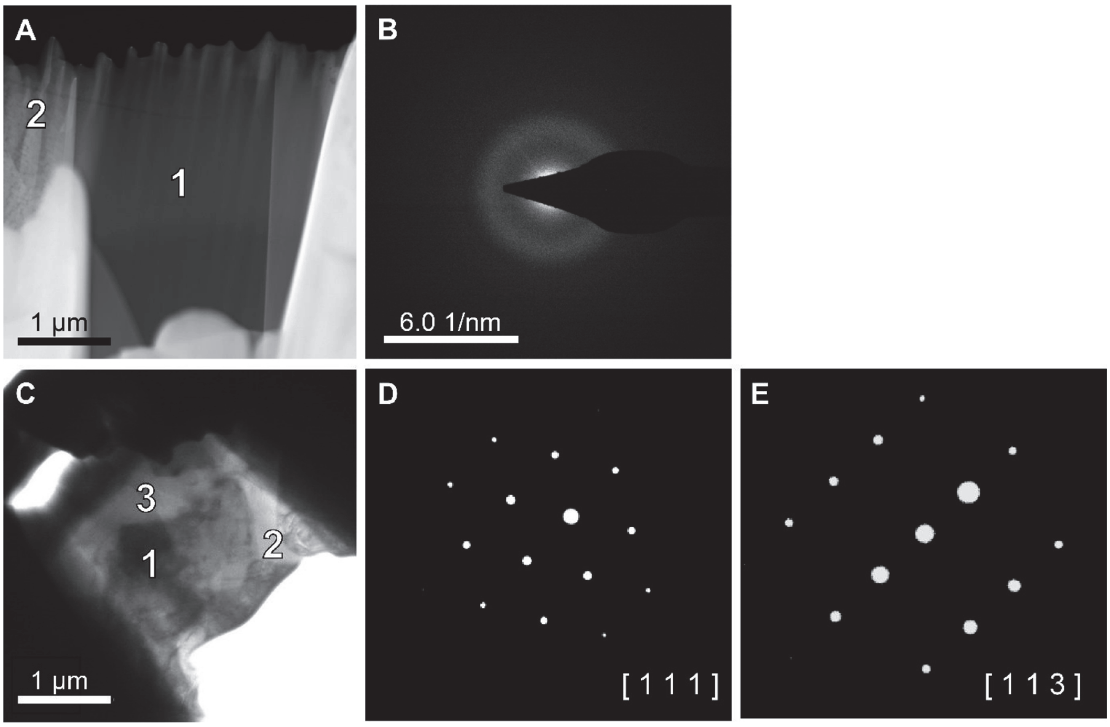

Fig. 3. TEM images of 0.1 M $CaCl_2$ and $SrCl_2$ scaffold grain boundary. $CaCl_2$ sample showed (A) showed an amorphous phase rich in Al, Si and Ca (1) and TiO_2 crystals (2). No diffraction was observed in the amorphous phase rich in Ca (B). The $SrCl_2$ sample (C) contains $SrTiO_3$ (1), TiO_2 (3) crystals and an amorphous part rich in Si and Al (2). The selected area diffraction (SAD) pattern confirmed the crystal structure of $SrTiO_3$ and shows the planes [111] (D) and [113] (E).

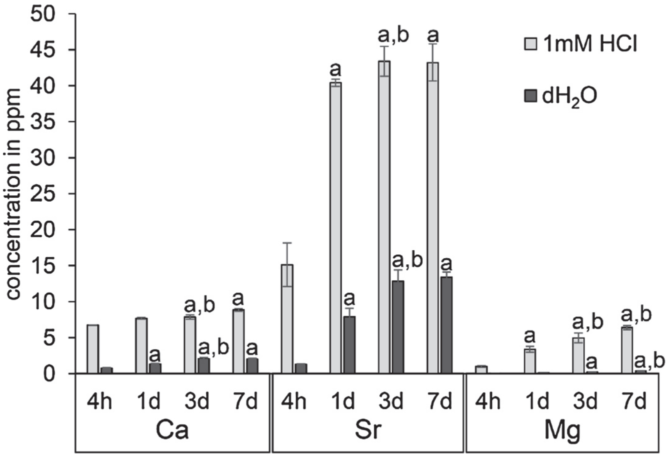

Fig. 4. Cumulative released ion profiles of doped TiO_2 scaffolds (n = 3) stored in 4 ml pH3 solution and dH_2O for different time points. Significant difference ($p < 0.001$, n = 6) is indicated in comparison to the earliest time point (4 h) (a) and to one time point earlier (b).

improved the corrosion resistance of alumina due to MgO doping [13]. Although the new grain boundary phase present in Mg doped scaffolds seemed to be more corrosion resistant compared to other doped scaffolds based on observed prolonged release of Mg, this phase did not resulted in a stable compressive strength of doped scaffolds stored in dH_2O or 1 mM HCl.

3.2. Effect of salt concentration on grain boundary development and corrosion behavior

In accordance to Müller et al. [8], our results showed that ion leaching and dissolution confined to grain boundaries resulted in the release of impurity ions from the grain boundaries. Furthermore, the present study showed that the dissolution of these impurity ions occurred whether a crystalline or amorphous phase was present at the grain boundary. To understand the development of these phases present in the grain boundaries, scaffolds with incrementally increasing salt concentration were tested. Additionally, the corrosion behavior was tested to correlate grain boundary phase development and corrosion in cation doped TiO_2 scaffolds.

The development of the grain boundary phase in all three doped scaffolds groups was similar. No changes in the grain boundaries were observed for 0.02 and 0.04 M scaffolds, which was consistent with the similar compressive strength of these scaffolds compared to undoped scaffolds (Figs. 5 and 6). By increasing the concentration to 0.06 M, the grain boundary formation changed and the distinct grain boundary formation started to form. Especially after exposing these scaffolds to 1 mM HCl, the new grain boundary formation and the characteristic dopant dependent corrosion resulted in a significant decreased compressive strength. The amorphous phase forming in Ca doped scaffolds was homogenously distributed until the Ca ion concentration of 0.08 M. SEM images and the slightly decrease in the compressive strength after corrosion confirmed a homogeneous distribution and dissolution of the amorphous phase. With a concentration of 0.1 M, the previously described TiO_2 lamellae start to form and the resulting change from a homogeneous to a localised dissolution of the amorphous phase between these lamellae caused a significant decrease in compressive strength. The presence of a crystalline grain boundary phase in Sr doped scaffolds was increased with increased dopant concentration. The increasing amount of crystalline $SrTiO_3$ led to a more localised corrosion resulting in deep holes in the grain boundary, as previous described. Sr and Mg doped scaffolds showed a similar development at grain boundaries: the higher the salt concentration the higher the amount of the $SrTiO_3$ crystals or Mg rich spots. One explanation for this could be that the more corrosion resistant phase forming in Mg doped scaffolds consisting of $MgTiO_3$ crystals. Because of the sintering parameters, such as holding temperature and cooling rate, the formation of $MgTiO_3$ crystals may not be sufficient to reach similar amount of crystalline $MgTiO_3$ compared to the $SrTiO_3$ in the Sr doped scaffolds.

Overall, corrosion was observed in all doped scaffolds in the form of ion leaching and dissolution. Because of a more corrosion resistant behavior of crystalline structures, the corrosion was concentrated in amorphous regions. Furthermore, with increasing impurity content in grain boundaries, the decrease in binding energy causes corrosion concentrated in these areas [14]. Fig. 7 summarizes the most important corrosion mechanism. Ca doped scaffolds showed a homogeneous removal of material in grain boundaries, while Sr and Mg doped scaffolds showed a concentrated and deep corrosion in the amorphous areas between the crystalline phases. Furthermore, the formation of the characteristic grain boundaries led to higher structural densification and significant higher compressive strength. Simultaneously, the significant loss in compressive strength caused by the corrosion was strongly correlated to the specific grain boundary formation. No optimal compromise between increased compressive strength and corrosion resistance could be observed.

3.3. Cell response in the presence of released ions

The prepared TiO_2 bone scaffolds doped with divalent cations feature high interconnected pore volume with porosity of approximately 90% and average pore size exceeding 420 μm [5]. Previous studies showed that such TiO_2 bone scaffolds are osteoconductive and show osteogenic potential. Osteoconductivity was confirmed *in vivo* due to direct contact of bone and scaffold material [2], while *in vitro* tests showed the support of TiO_2 scaffolds on osteogenic differentiation of MC3T3-E1 pre-osteoblasts without osteogenic supplements [15]. Furthermore, human mesenchymal stem cells (hMSCs) cultured on TiO_2 scaffolds showed significant higher cell viability and proliferation compared to hMSCs cultured on commercially available bone graft granules [16]. Considering these results with other studies showing a positive influence of TiO_2 scaffolds on osteosarcoma cells (SaOs-2) and normal human osteoblasts (NHO) differentiation [17,18], the analysis of this study was focused on the influence of released ions while undoped TiO_2 scaffolds were used as a control. The used ions were expected to have a positive influence on osteogenic differentiation, because of their important role in bone biology [19–21]. An increased osteogenic differentiation in the presence of ions like Ca, Sr and Mg has been shown in previous studies [22,23]. An increased extracellular calcium concentration can cause an increase of intracellular calcium through calcium channels and results in activation of important targets

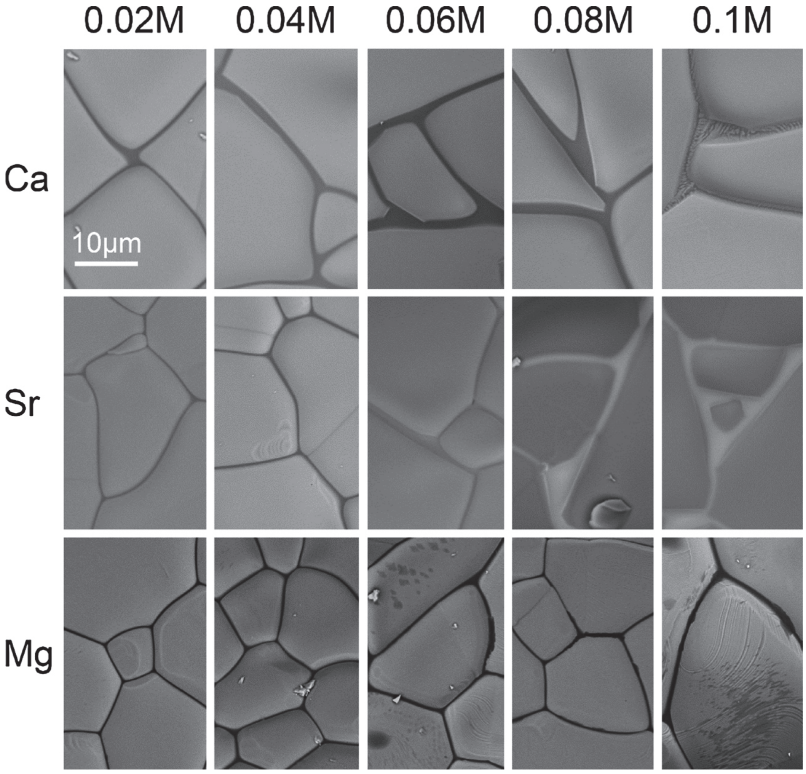

Fig. 5. Development of grain boundary morphology as observed by SEM depending on salt concentration in Ca, Sr and Mg doped TiO_2 scaffolds.

during osteogenic differentiation [24]. Strontium affects DNA synthesis and bone collagen synthesis strongly depending on the concentration [25]. Furthermore, strontium has a physical and chemical similarity to calcium and can increase osteoblast markers and matrix mineralization [26]. Besides the crucial role of magnesium in bone remodelling and skeletal development, the presence of increased magnesium concentration showed to increase osteoblast adhesion to implants [27,28].

In the present study, live dead staining and LDH activity, as a marker of cytotoxicity, showed no difference between the doped and undoped groups (Fig. 8). Next, the influence of released ions on hASCs osteogenic differentiation was studied. Gene expression analysis revealed that cells cultured on Mg doped scaffolds as a significant higher mRNA expression level of the osteogenic markers RUNX2, COL1 and ALP (Fig. 9).

The osteogenic differentiation requires the expression of the transcription factor RUNX2 to trigger the expression of later key osteogenic markers [29]. Among these, collagen type I, which is an essential component of the bone ECM, is produced. This is followed by an increased ALP expression which indicates the organization of the bone ECM and arrangement for mineralization. While RUNX2 and COL1 are early markers of osteogenic differentiation with a peak during proliferation, ALP is upregulated during extracellular matrix mineralization, maturation and organization [30]. Therefore, these genes are differently expressed during differentiation and can be used to determine the stage of osteoblast development. Thus, the real-time PCR results for the Mg group could be an indication for the differentiation of hASCs into the osteogenic lineage due to a significant higher gene expression level of the key osteogenic markers. A limitation of the present study is the measurement of one time point, what did not allow a time depending peak measurement of expressed genes. A peak in BSP expression would confirm fully differentiated osteoblasts [29]. The higher but not significant BSP expressions could lead to the assumption that the cells have not yet reached a fully differentiated state. In conclusion, Mg doping of TiO_2 scaffolds showed an increased osteogenic differentiation in hASCs.

This effect was not observed for cells seeded on Sr or Ca doped scaffolds although they showed a higher amount of released ions. A possible explanation could be that hASCs are more sensitive to Mg ions and a lower amount influences the cells in a significant increase in specific gene expressions. Previous studies showed different cell responses to different ions and their concentrations in vitro. While Wang et al. showed an improved cell response correlated with increasing the magnesium ion concentration, Aimaiti et al. demonstrated that a low concentration of strontium stimulates the cells whereby a high concentration cause apoptosis [31,32]. Another reason could be the different release profile of doped scaffolds. Although the amount of Ca and Sr ions is higher, after 3 days no further release was observed. Because of the need of media change during cell studies, the released ions were removed after 3 days. On the other hand, Mg doped scaffolds showed a different release profile and a significant increase in released ions after 3 days. Therefore, Mg is the only group that differs from the control scaffolds from that time point on, suggesting that the released Mg ions can promote osteogenic differentiation of hASCs.

4. Conclusion

The corrosion in doped TiO_2 scaffolds confined to grain boundaries. Sr doping resulted in a new crystalline $SrTiO_3$ phase present in amorphous Si and Al rich grain boundaries. After exposure to an acidic solution, ion leaching and dissolution took place in the amorphous regions of the grain boundary phase. The removal of material in small areas led to deep holes and a significant decrease in compressive strength. The corrosion effect was similar for Mg doped scaffolds. Ca doping resulted in an amorphous phase rich in Ca, Al and Si. The corrosion in these purely amorphous grain boundaries was homogenous throughout the entire grain boundary region. Although the corrosion behavior was different, grain boundary corrosion resulted in a decreased compressive strength for all doped scaffolds. The effect of the

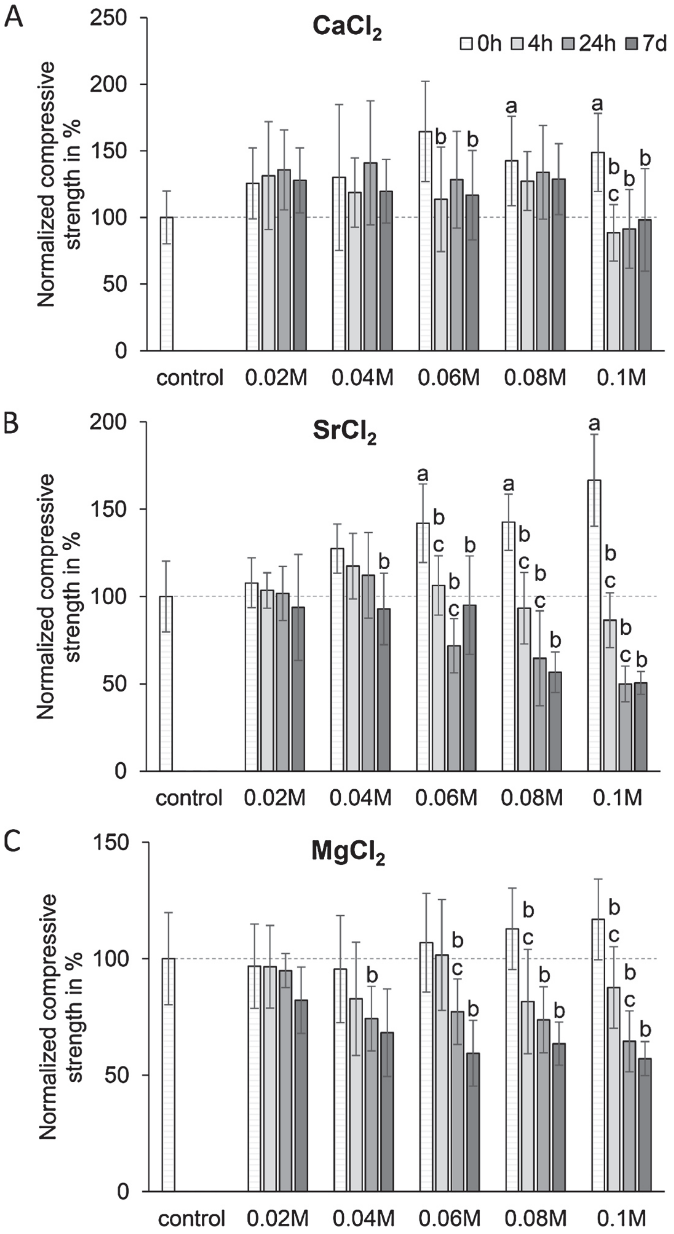

Fig. 6. Normalized compressive strength of Ca (A), Sr (B) and Mg (c) doped scaffolds with increasing doping concentration after short term corrosion test in 1 mM HCl. Significant differences ($p < 0.001$, $n = 10$) compared to the control scaffolds (a), to the same concentration at 0 h (b) and to the same concentration at one time point earlier (c) are highlighted.

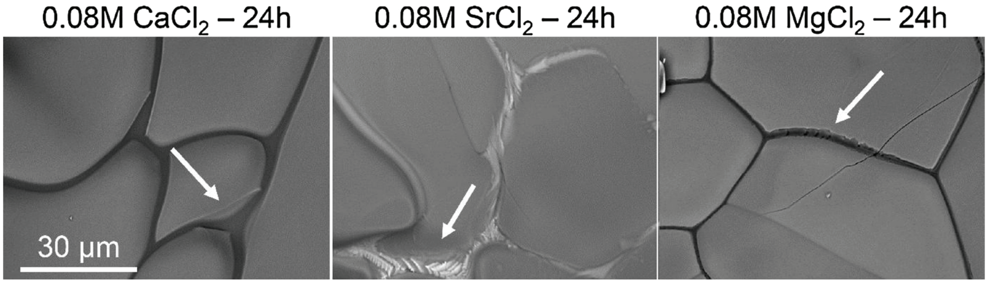

Fig. 7. Highlights of corroded scaffolds, doped with 0.08 M of different salts. $CaCl_2$ scaffolds showed homogeneous 'washed out' grain boundaries. $SrCl_2$ and $MgCl_2$ showed concentrated corrosion in amorphous parts of the grain boundary.

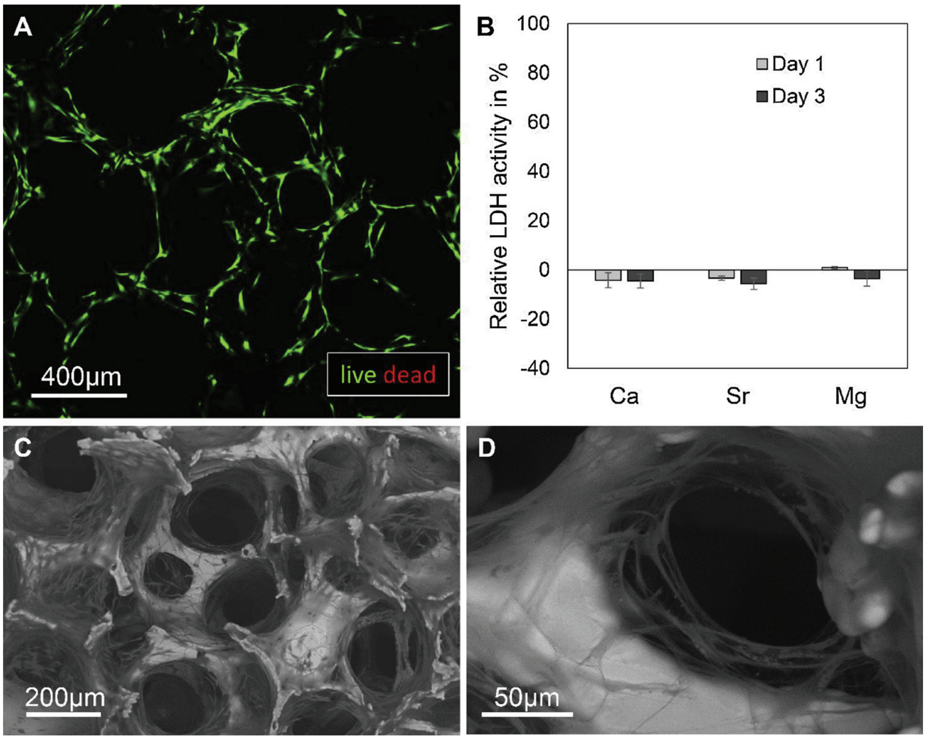

Fig. 8. Cell viability of hASCs cultured on cationic doped TiO_2 scaffolds. Live dead staining shows mainly living cells on control scaffolds after day 3 (A). The relative LDH activity in % showed that none of the doped groups showed any cytotoxic effect on hASCs (B). SEM images confirmed the growth of hASCs inside $MgCl_2$ scaffolds (C) and along the struts in $CaCl_2$ (D) after 14 days. No observed difference in tested groups, therefore, images A, C and D are representative for all tested groups.

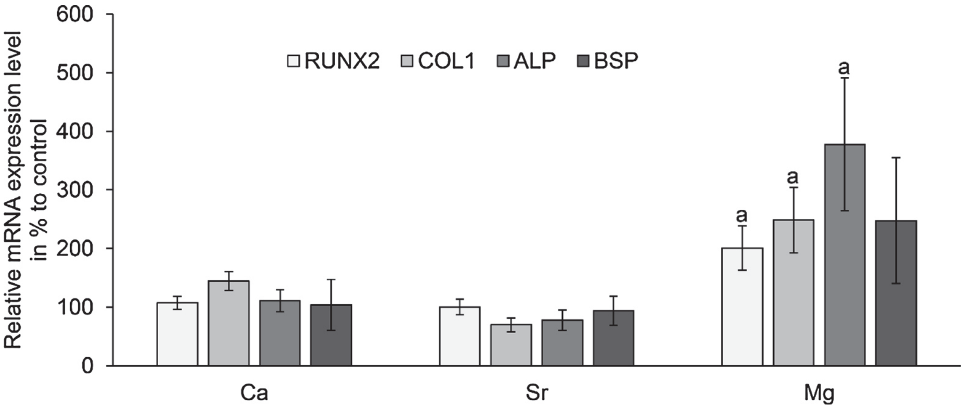

Fig. 9. Relative mRNA levels of RUNX2, COL1, ALP and BSP in hASCs cultured on doped TiO_2 scaffolds after 14 days. The expression level is given as % compared to cells cultured on undoped control scaffolds (100% expression). Cells seeded on Mg doped scaffolds showed a significant higher level in COL1, ALP and RUNX2 after 14 days compared to cells seeded on undoped scaffolds. a: $p < 0.05$, $n = 4$.

higher densification of TiO_2 in the presence of additional ions such as Ca, Sr and Mg and the resulting significant increase in compressive strength was found to be strongly depending on the new grain boundary formation. This new grain boundary formation caused a lower corrosion resistance and a significant decrease in compressive strength after corrosion. An optimal compromise between an increased compressive strength and corrosion resistant was not found.

The amount of released ions did not show any cytotoxic effect on hASCs. Released Mg ions showed a positive influence on hASCs, resulting in a significant increased osteogenic differentiation.

Acknowledgements

The authors thank Rui Domingues and Ana Gonçalves for their excellent technical assistance with confocal and real-time PCR. The authors acknowledge UiO:Life Science and Erasmus+ staff mobility for providing traveling grants for Anne Klemm to perform experiments at 3B's Research Group, Univeristy of Minho.

References

[1] H. Haugen, J. Will, A. Köhler, U. Hopfner, J. Aigner, E. Wintermantel, Ceramic TiO2-foams: characterisation of a potential scaffold, J. Eur. Ceram. Soc. 24 (4) (2004) 661–668.
[2] H. Tiainen, J.C. Wohlfahrt, A. Verket, S.P. Lyngstadaas, H.J. Haugen, Bone formation in TiO2 bone scaffolds in extraction sockets of minipigs, Acta Biomater. 8 (6) (2012) 2384–2391.
[3] H.J. Haugen, M. Monjo, M. Rubert, A. Verket, S.P. Lyngstadaas, J.E. Ellingsen, H.J. Rønold, J.C. Wohlfahrt, Porous ceramic titanium dioxide scaffolds promote bone formation in rabbit peri-implant cortical defect model, Acta Biomater. 9 (2) (2013) 5390–5399.
[4] H. Tiainen, D. Wiedmer, H.J. Haugen, Processing of highly porous TiO2 bone scaffolds with improved compressive strength, J. Eur. Ceram. Soc. 33 (1) (2013) 15–24.
[5] A. Klemm, H. Tiainen, Coagulated concentrated anatase slurry leads to improved strength of ceramic TiO2 bone scaffolds, Ceram. Int. 44 (6) (2018) 6265–6271.
[6] I. Silver, R. Murrills, D. Etherington, Microelectrode studies on the acid microenvironment beneath adherent macrophages and osteoclasts, Exp. Cell Res. 175 (2) (1988) 266–276.
[7] W.B. White, Theory of Corrosion of Glass and Ceramics, Corrosion of Glass, Ceramics and Ceramic Superconductors, (1992), pp. 2–28.
[8] B. Müller, H. Haugen, S.L. Simonsen, H. Tiainen, Grain boundary corrosion of highly porous ceramic TiO2 foams is reduced by annealing and quenching, J. Eur. Ceram. Soc. 36 (1) (2016) 179–188.

[9] M.W. Pfaffl, A new mathematical model for relative quantification in real-time RT–PCR, Nucleic Acids Res. 29 (9) (2001) e45-e45.

[10] M.W. Pfaffl, A. Tichopad, C. Prgomet, T.P. Neuvians, Determination of stable housekeeping genes, differentially regulated target genes and sample integrity: BestKeeper–excel-based tool using pair-wise correlations, Biotechnol. Lett. 26 (6) (2004) 509–515.

[11] L. Ćurković, M.F. Jelača, S. Kurajica, Corrosion behavior of alumina ceramics in aqueous HCl and H2SO4 solutions, Corros. Sci. 50 (3) (2008) 872–878.

[12] K.R. Mikeska, S.J. Bennison, S.L. Grise, Corrosion of ceramics in aqueous hydrofluoric acid, J. Am. Ceram. Soc. 83 (5) (2000) 1160–1164.

[13] K.L. Gavrilov, S.J. Bennison, K.R. Mikeska, J.M. Chabala, R. Levi-Setti, Silica and magnesia dopant distributions in alumina by high-resolution scanning secondary ion mass spectrometry, J. Am. Ceram. Soc. 82 (4) (1999) 1001–1008.

[14] Y. Takigawa, Y. Ikuhara, T. Sakuma, Grain boundary bonding state and fracture energy in small amount of oxide-doped fine-grained Al2O3, J. Mater. Sci. 34 (9) (1999) 1991–1997.

[15] M. Gómez-Florit, M. Rubert, J.M. Ramis, H.J. Haugen, H. Tiainen, S.P. Lyngstadaas, M. Monjo, TiO2 scaffolds sustain differentiation of MC3T3-E1 cells, J. Biomater. Tissue Eng. 2 (4) (2012) 336–344.

[16] R. Sabetrasekh, H. Tiainen, S.P. Lyngstadaas, J. Reseland, H. Haugen, A novel ultra-porous titanium dioxide ceramic with excellent biocompatibility, J. Biomater. Appl. 25 (6) (2011) 559–580.

[17] B. Müller, J.E. Reseland, H.J. Haugen, H. Tiainen, Cell growth on pore-graded biomimetic TiO2 bone scaffolds, J. Biomater. Appl. 29 (9) (2015) 1284–1295.

[18] A. Verket, H. Tiainen, H.J. Haugen, S.P. Lyngstadaas, O. Nilsen, J.E. Reseland, Enhanced osteoblast differentiation on scaffolds coated with TiO 2 compared to SiO 2 and CaP coatings, Biointerphases 7 (1–4) (2012) 36.

[19] S.P. Nielsen, The biological role of strontium, Bone 35 (3) (2004) 583–588.

[20] H.C. Blair, L.J. Robinson, C.L.H. Huang, L. Sun, P.A. Friedman, P.H. Schlesinger, M. Zaidi, Calcium and bone disease, Biofactors 37 (3) (2011) 159–167.

[21] S. Castiglioni, A. Cazzaniga, W. Albisetti, J.A. Maier, Magnesium and osteoporosis: current state of knowledge and future research directions, Nutrients 5 (8) (2013) 3022–3033.

[22] A.J. Leite, A.I. Gonçalves, M.T. Rodrigues, M.E. Gomes, J.F. Mano, Strontium doped bioactive glass nanoparticles in osteogenic commitment, ACS Appl. Mater. Interfaces (2018).

[23] H. Gu, F. Guo, X. Zhou, L. Gong, Y. Zhang, W. Zhai, L. Chen, L. Cen, S. Yin, J. Chang, The stimulation of osteogenic differentiation of human adipose-derived stem cells by ionic products from akermanite dissolution via activation of the ERK pathway, Biomaterials 32 (29) (2011) 7023–7033.

[24] G.-Y. Jung, Y.-J. Park, J.-S. Han, Effects of HA released calcium ion on osteoblast differentiation, J. Mater. Sci.: Mater. Med. 21 (5) (2010) 1649–1654.

[25] P. Marie, P. Ammann, G. Boivin, C. Rey, Mechanisms of action and therapeutic potential of strontium in bone, Calcif. Tissue Int. 69 (3) (2001) 121–129.

[26] P. Marie, D. Felsenberg, M. Brandi, How strontium ranelate, via opposite effects on bone resorption and formation, prevents osteoporosis, Osteoporos. Int. 22 (6) (2011) 1659–1667.

[27] H. Zreiqat, C. Howlett, A. Zannettino, P. Evans, G. Schulze-Tanzil, C. Knabe, M. Shakibaei, Mechanisms of magnesium-stimulated adhesion of osteoblastic cells to commonly used orthopaedic implants, J. Biomed. Mater. Res. 62 (2) (2002) 175–184.

[28] Y. Yamasaki, Y. Yoshida, M. Okazaki, A. Shimazu, T. Uchida, T. Kubo, Y. Akagawa, Y. Hamada, J. Takahashi, N. Matsuura, Synthesis of functionally graded MgCO3 apatite accelerating osteoblast adhesion, J. Biomed. Mater. Res. 62 (1) (2002) 99–105.

[29] R. Miron, Y. Zhang, Osteoinduction: a review of old concepts with new standards, J. Dent. Res. 91 (8) (2012) 736–744.

[30] G.S. Stein, J.B. Lian, J.L. Stein, A.J. Van Wijnen, M. Montecino, Transcriptional control of osteoblast growth and differentiation, Physiol. Rev. 76 (2) (1996) 593–629.

[31] G. Wang, J. Li, W. Zhang, L. Xu, H. Pan, J. Wen, Q. Wu, W. She, T. Jiao, X. Liu, Magnesium ion implantation on a micro/nanostructured titanium surface promotes its bioactivity and osteogenic differentiation function, Int. J. Nanomedicine 9 (2014) 2387.

[32] A. Aimaiti, A. Maimaitiyiming, X. Boyong, K. Aji, C. Li, L. Cui, Low-dose strontium stimulates osteogenesis but high-dose doses cause apoptosis in human adipose-derived stem cells via regulation of the ERK1/2 signaling pathway, Stem Cell Res. Ther. 8 (1) (2017) 282.